

Washington University in St. Louis

Washington University Open Scholarship

All Theses and Dissertations (ETDs)

5-24-2010

Development of Kinetic Schemes for the Numerical Solutions of the 3-D Euler and the Ideal Magnetohydrodynamics Equations

Wei Dong

Washington University in St. Louis

Follow this and additional works at: <https://openscholarship.wustl.edu/etd>

Recommended Citation

Dong, Wei, "Development of Kinetic Schemes for the Numerical Solutions of the 3-D Euler and the Ideal Magnetohydrodynamics Equations" (2010). *All Theses and Dissertations (ETDs)*. 847.
<https://openscholarship.wustl.edu/etd/847>

This Dissertation is brought to you for free and open access by Washington University Open Scholarship. It has been accepted for inclusion in All Theses and Dissertations (ETDs) by an authorized administrator of Washington University Open Scholarship. For more information, please contact digital@wumail.wustl.edu.

WASHINGTON UNIVERSITY IN ST. LOUIS

School of Engineering and Applied Science
Department of Mechanical Engineering & Materials Science

Dissertation Examination Committee:

Ramesh K. Agarwal, Chair
Raimo J. Hakkinen
Guy Genin
Norman I. Katz
Mori Mani
David A. Peters
Shankar Sastry

Development of Kinetic Schemes for the Numerical Solutions
of the 3-D Euler and the Ideal Magnetohydrodynamics Equations

by

Wei Dong

A dissertation submitted to the
Graduate School of Arts and Sciences
of Washington University in St. Louis
in partial fulfillment of the requirements for
the degree of Doctor of Philosophy

December 2010

Saint Louis, Missouri

Acknowledgments

I would like to express my deep gratitude to my advisor Prof. Ramesh Agarwal for his advice, encouragement and patience. This thesis would not have been possible without his consistent assistance. I am also indebted to my dissertation committee members Dr. Mori Mani and Dr. Raimo Hakkinen for their invaluable suggestions and assistance. I would like to thank other members of the dissertation committee – Prof. Norman Katz, Prof. Guy Genin, Prof. David Peters, and Prof. Shankar Sastry for reading the thesis and for providing feedback and constructive comments, which have been essential for improving the content of this thesis.

I am thankful to my colleagues and friends in the CFD lab in the Department of Mechanical Engineering & Materials Science, Loren Ahaus, Xiaomin Chen and Zheming Zhang, for valuable technical discussions, and helpful suggestions as well as for their other support.

Finally, I am grateful to my parents, my brother, and all my friends for their help and care while I have been working on this dissertation.

Wei Dong

Washington University in Saint Louis

December 19, 2010

Contents

Acknowledgments	ii
Abstract	xix
1 Introduction	1
1.1 Kinetic Schemes for the Euler Equations	2
1.2 Kinetic Schemes for the Ideal Magnetohydrodynamics Equations	4
2 Derivations of the Kinetic Schemes for the Euler Equations	6
2.1 Connection between the Boltzmann Equation and the Euler Equations . . .	7
2.1.1 Conservation of Mass	10
2.1.2 Conservation of Momentum	10
2.1.3 Conservation of Total Energy	11
2.2 Explicit Kinetic Schemes (KFVS and KWPS) for the Euler Equations . . .	12
2.3 Implicit Kinetic Schemes for the Euler Equations	15
2.3.1 Continuum Approach	16
2.3.2 Molecular Approach	18
2.3.3 Eigenvalues of the Jacobian Matrix	19
3 Derivations of the Kinetic Schemes for the Ideal MHD Equations	23

3.1	Connection between the Boltzmann Equation and the Ideal MHD Equations	23
3.1.1	Conservation of Mass	26
3.1.2	Conservation of Momentum	27
3.1.3	Conservation of Total Energy	27
3.2	Derivations of the Kinetic Schemes for the Ideal MHD Equations	28
3.2.1	One-Dimensional Formulation	29
3.2.2	Multi-Dimensional Formulation	32
3.2.3	Derivation of Implicit Kinetic Schemes for the Ideal MHD Equations	34
3.2.4	Implementation of the Poisson Solver	39
4	Code Validation Test Cases	42
4.1	Explicit KWPS Scheme for the Euler Equations	43
4.1.1	One-Dimensional Test Cases for the Explicit KWPS Euler Code	43
4.1.2	Two-Dimensional Test Cases for the Explicit KWPS Euler Code	47
4.2	Explicit KWPS Scheme for the Ideal MHD Equations	50
5	Computation of Inviscid Supersonic Flow Past an Axisymmetric Blunt Body	
	Using the 3-D Euler solver	53
5.1	Computational Domain and Grid	54
5.2	Flowfield Computations	58
5.2.1	Flowfield Computations at $M = 5.85, \alpha = 0^\circ$	58
5.2.2	Flowfield Computations at $M = 5.85, \alpha = 3^\circ$	67
5.2.3	Flowfield Computations at $M = 5.85, \alpha = 6^\circ$	74
5.2.4	Flowfield Computations at $M = 5.85, \alpha = 10^\circ$	81
5.2.5	Flowfield Computations at $M = 5.85, \alpha = 15^\circ$	88

6	Computation of Inviscid Supersonic MHD Flow Past an Axisymmetric Blunt Body Using the 3-D Ideal MHD solver	95
6.1	MHD Flowfield Computations at $M = 5.85$, $\alpha = 0^\circ$, $B_x = B_y = 0$, $B_z = 0.04$ T	96
6.2	MHD Flowfield Computations at $M = 5.85$, $\alpha = 0^\circ$, $B_x = B_y = 0$, $B_z = 0.06$ T	101
6.3	Comparison of Euler and MHD Flowfield Computations at $M = 5.85$, $\alpha = 0^\circ$, $B_x = B_y = 0$, $B_z = 0.04$ T and 0.06 T	106
7	Summary	112
	References	114
	APPENDICES	119
A	Derivation of the 1-D Kinetic Schemes for the Euler Equations	120
A.1	The Maxwellian Gas	121
A.2	Conserved Variables (Field) Vector	122
A.3	Kinetic-Flux-Vector-Splitting (KFVS) Scheme Flux-Vector	125
A.4	Kinetic-Wave-Particle-Splitting (KWPS) Scheme Flux-Vector	128
B	Metrics of Transformation for the Generalized Curvilinear Coordinate System	131
B.1	Computation of the Metrics of Transformation	131
B.2	Differentiation of the Metrics of Transformation	133
C	Implementation of Boundary Conditions	136
C.1	Supersonic Inflow	136
C.2	Supersonic Outflow	137

C.3 Subsonic Outflow	137
C.4 Solid Wall Boundary Condition	137
D Computational Code (Separate Document)	139

List of Figures

4.1	Analytical solutions for the Sod's shock tube test case [31]	44
4.2	Explicit KWPS calculations for the Sod's shock tube test case [27]	44
4.3	Density & pressure profiles obtained by the explicit KFVS and KWPS schemes for the shock structure computations[27]	46
4.4	Velocity & Mach number profiles obtained by the explicit KFVS and KWPS schemes for the shock structure computations[27]	46
4.5	Density (L) and thermal pressure (R) contours for the cylindrical blast-wave test case	48
4.6	Density contour plots for the blunt-body computation using the explicit (L) and implicit (R) KWPS scheme	48
4.7	Density, thermal pressure, and temperature profiles along the stagnation line of the 2-D blunt body using the explicit KWPS scheme	49
4.8	Computed Euler and Ideal MHD Density Profiles with an Explicit and Implicit KWPS Solver for Flow in a Shock Tube	51
4.9	Computed Ideal MHD Thermal and Magnetic Pressure Profiles with an Explicit and Implicit KWPS Solver for Flow in a Shock Tube	51
4.10	Computed Ideal MHD Velocity Profiles with an Explicit and Implicit KWPS Solver for Flow in a Shock Tube	52

5.1	Cross-section of the computational domain for Supersonic Flow Past an Axisymmetric Blunt Body	55
5.2	View of the Grid in the $x - y$ Plane	56
5.3	Side View of the Grid	56
5.4	View of the Grid in the $y - z$ Plane	57
5.5	Convergent History of the L_2 - norm of Density for the Supersonic Flow Past an Axisymmetric Blunt Body; $M = 5.85, \alpha = 0^\circ$	60
5.6	Density Profile along the Stagnation Line for Supersonic Flow Past an Axisymmetric Blunt Body; $M = 5.85, \alpha = 0^\circ$; the stagnation point - nose of the body - is at $x = -0.1$	60
5.7	Density Contours in the $x - y$ Plane for Supersonic Flow Past an Axisymmetric Blunt Body; $M = 5.85, \alpha = 0^\circ$	61
5.8	3-D View of the Density Contours for Supersonic Flow Past an Axisymmetric Blunt Body; $M = 5.85, \alpha = 0^\circ$	61
5.9	Streamwise Velocity Profile along the Stagnation Line for Supersonic Flow Past an Axisymmetric Blunt Body; $M = 5.85, \alpha = 0^\circ$	62
5.10	Velocity Contours in the $x - y$ Plane for Supersonic Flow Past an Axisymmetric Blunt Body; $M = 5.85, \alpha = 0^\circ$	62
5.11	3-D View of the Velocity Contours for Supersonic Flow Past an Axisymmetric Blunt Body; $M = 5.85, \alpha = 0^\circ$	63
5.12	Temperature Profile along the Stagnation Line for Supersonic Flow Past an Axisymmetric Blunt Body; $M = 5.85, \alpha = 0^\circ$	63
5.13	Temperature Contours in the $x - y$ Plane for Supersonic Flow Past an Axisymmetric Blunt Body; $M = 5.85, \alpha = 0^\circ$	64
5.14	3-D View of the Temperature Contours for Supersonic Flow Past an Axisymmetric Blunt Body; $M = 5.85, \alpha = 0^\circ$	64

5.15	Total Pressure Profile along the Stagnation Line for Supersonic Flow Past an Axisymmetric Blunt Body; $M = 5.85, \alpha = 0^\circ$	65
5.16	Total Pressure Contours in the $x - y$ Plane for Supersonic Flow Past an Axisymmetric Blunt Body; $M = 5.85, \alpha = 0^\circ$	65
5.17	3-D View of the Total Pressure Contours for Supersonic Flow Past an Axisymmetric Blunt Body; $M = 5.85, \alpha = 0^\circ$	66
5.18	Density Profile along the Stagnation Line for Supersonic Flow Past an Axisymmetric Blunt Body; $M = 5.85, \alpha = 3^\circ$	68
5.19	Density Contours in the $x - y$ Plane for Supersonic Flow Past an Axisymmetric Blunt Body; $M = 5.85, \alpha = 3^\circ$	68
5.20	3-D View of the Density Contours for Supersonic Flow Past an Axisymmetric Blunt Body; $M = 5.85, \alpha = 3^\circ$	69
5.21	Streamwise Velocity Profile along the Stagnation Line for Supersonic Flow Past an Axisymmetric Blunt Body; $M = 5.85, \alpha = 3^\circ$	69
5.22	Velocity Contours in the $x - y$ Plane for Supersonic Flow Past an Axisymmetric Blunt Body; $M = 5.85, \alpha = 3^\circ$	70
5.23	3-D View of the Velocity Contours for Supersonic Flow Past an Axisymmetric Blunt Body; $M = 5.85, \alpha = 3^\circ$	70
5.24	Temperature Profile along the Stagnation Line for Supersonic Flow Past an Axisymmetric Blunt Body; $M = 5.85, \alpha = 3^\circ$	71
5.25	Temperature Contours in the $x - y$ Plane for Supersonic Flow Past an Axisymmetric Blunt Body; $M = 5.85, \alpha = 3^\circ$	71
5.26	3-D View of the Temperature Contours for Supersonic Flow Past an Axisymmetric Blunt Body; $M = 5.85, \alpha = 3^\circ$	72
5.27	Total Pressure Profile along the Stagnation Line for Supersonic Flow Past an Axisymmetric Blunt Body; $M = 5.85, \alpha = 3^\circ$	72

5.28	Total Pressure Contours in the $x - y$ Plane for Supersonic Flow Past an Axisymmetric Blunt Body; $M = 5.85, \alpha = 3^\circ$	73
5.29	3-D View of the Total Pressure Contours for Supersonic Flow Past an Axisymmetric Blunt Body; $M = 5.85, \alpha = 3^\circ$	73
5.30	Density Profile along the Stagnation Line for Supersonic Flow Past an Axisymmetric Blunt Body; $M = 5.85, \alpha = 6^\circ$	75
5.31	Density Contours in the $x - y$ Plane for Supersonic Flow Past an Axisymmetric Blunt Body; $M = 5.85, \alpha = 6^\circ$	75
5.32	3-D View of the Density Contours for Supersonic Flow Past an Axisymmetric Blunt Body; $M = 5.85, \alpha = 6^\circ$	76
5.33	Streamwise Velocity Profile along the Stagnation Line for Supersonic Flow Past an Axisymmetric Blunt Body; $M = 5.85, \alpha = 6^\circ$	76
5.34	Velocity Contours in the $x - y$ Plane for Supersonic Flow Past an Axisymmetric Blunt Body; $M = 5.85, \alpha = 6^\circ$	77
5.35	3-D View of the Velocity Contours for Supersonic Flow Past an Axisymmetric Blunt Body; $M = 5.85, \alpha = 6^\circ$	77
5.36	Temperature Profile along the Stagnation Line for Supersonic Flow Past an Axisymmetric Blunt Body; $M = 5.85, \alpha = 6^\circ$	78
5.37	Temperature Contours in the $x - y$ Plane for Supersonic Flow Past an Axisymmetric Blunt Body; $M = 5.85, \alpha = 6^\circ$	78
5.38	3-D View of the Temperature Contours for Supersonic Flow Past an Axisymmetric Blunt Body; $M = 5.85, \alpha = 6^\circ$	79
5.39	Total Pressure Profile along the Stagnation Line for Supersonic Flow Past an Axisymmetric Blunt Body; $M = 5.85, \alpha = 6^\circ$	79
5.40	Total Pressure Contours in the $x - y$ Plane for Supersonic Flow Past an Axisymmetric Blunt Body; $M = 5.85, \alpha = 6^\circ$	80

5.41	3-D View of the Total Pressure Contours for Supersonic Flow Past an Axisymmetric Blunt Body; $M = 5.85, \alpha = 6^\circ$	80
5.42	Density Profile along the Stagnation Line for Supersonic Flow Past an Axisymmetric Blunt Body; $M = 5.85, \alpha = 10^\circ$	82
5.43	Density Contours in the $x - y$ Plane for Supersonic Flow Past an Axisymmetric Blunt Body; $M = 5.85, \alpha = 10^\circ$	82
5.44	3-D View of the Density Contours for Supersonic Flow Past an Axisymmetric Blunt Body; $M = 5.85, \alpha = 10^\circ$	83
5.45	Streamwise Velocity Profile along the Stagnation Line for Supersonic Flow Past an Axisymmetric Blunt Body; $M = 5.85, \alpha = 10^\circ$	83
5.46	Velocity Contours in the $x - y$ Plane for Supersonic Flow Past an Axisymmetric Blunt Body; $M = 5.85, \alpha = 10^\circ$	84
5.47	3-D View of the Velocity Contours for Supersonic Flow Past an Axisymmetric Blunt Body; $M = 5.85, \alpha = 10^\circ$	84
5.48	Temperature Profile along the Stagnation Line for Supersonic Flow Past an Axisymmetric Blunt Body; $M = 5.85, \alpha = 10^\circ$	85
5.49	Temperature Contours in the $x - y$ Plane for Supersonic Flow Past an Axisymmetric Blunt Body; $M = 5.85, \alpha = 10^\circ$	85
5.50	3-D View of the Temperature Contours for Supersonic Flow Past an Axisymmetric Blunt Body; $M = 5.85, \alpha = 10^\circ$	86
5.51	Total Pressure Profile along the Stagnation Line for Supersonic Flow Past an Axisymmetric Blunt Body; $M = 5.85, \alpha = 10^\circ$	86
5.52	Total Pressure Contours in the $x - y$ Plane for Supersonic Flow Past an Axisymmetric Blunt Body; $M = 5.85, \alpha = 10^\circ$	87
5.53	3-D View of the Total Pressure Contours for Supersonic Flow Past an Axisymmetric Blunt Body; $M = 5.85, \alpha = 10^\circ$	87

5.54	Density Profile along the Stagnation Line for Supersonic Flow Past an Axisymmetric Blunt Body; $M = 5.85, \alpha = 15^\circ$	89
5.55	Density Contours in the $x - y$ Plane for Supersonic Flow Past an Axisymmetric Blunt Body; $M = 5.85, \alpha = 15^\circ$	89
5.56	3-D View of the Density Contours for Supersonic Flow Past an Axisymmetric Blunt Body; $M = 5.85, \alpha = 15^\circ$	90
5.57	Streamwise Velocity Profile along the Stagnation Line for Supersonic Flow Past an Axisymmetric Blunt Body; $M = 5.85, \alpha = 15^\circ$	90
5.58	Velocity Contours in the $x - y$ Plane for Supersonic Flow Past an Axisymmetric Blunt Body; $M = 5.85, \alpha = 15^\circ$	91
5.59	3-D View of the Velocity Contours for Supersonic Flow Past an Axisymmetric Blunt Body; $M = 5.85, \alpha = 15^\circ$	91
5.60	Temperature Profile along the Stagnation Line for Supersonic Flow Past an Axisymmetric Blunt Body; $M = 5.85, \alpha = 15^\circ$	92
5.61	Temperature Contours in the $x - y$ Plane for Supersonic Flow Past an Axisymmetric Blunt Body; $M = 5.85, \alpha = 15^\circ$	92
5.62	3-D View of the Temperature Contours for Supersonic Flow Past an Axisymmetric Blunt Body; $M = 5.85, \alpha = 15^\circ$	93
5.63	Total Pressure Profile along the Stagnation Line for Supersonic Flow Past an Axisymmetric Blunt Body; $M = 5.85, \alpha = 15^\circ$	93
5.64	Total Pressure Contours in the $x - y$ Plane for Supersonic Flow Past an Axisymmetric Blunt Body; $M = 5.85, \alpha = 15^\circ$	94
5.65	3-D View of the Total Pressure Contours for Supersonic Flow Past an Axisymmetric Blunt Body; $M = 5.85, \alpha = 15^\circ$	94

6.1	Density Profile along the Stagnation Line for Supersonic Flow Past an Axisymmetric Blunt Body; $M = 5.85, \alpha = 0^\circ, B_x = B_y = 0, B_z = 0.04 T$	97
6.2	Streamwise Velocity Profile along the Stagnation Line for Supersonic Flow Past an Axisymmetric Blunt Body; $M = 5.85, \alpha = 0^\circ, B_x = B_y = 0, B_z = 0.04 T$	97
6.3	Temperature Profile along the Stagnation Line for Supersonic Flow Past an Axisymmetric Blunt Body; $M = 5.85, \alpha = 0^\circ, B_x = B_y = 0, B_z = 0.04 T$	98
6.4	Thermal Pressure Profile along the Stagnation Line for Supersonic Flow Past an Axisymmetric Blunt Body; $M = 5.85, \alpha = 0^\circ, B_x = B_y = 0, B_z = 0.04 T$	98
6.5	Density Contours in the $x - y$ Plane for Supersonic Flow Past an Axisymmetric Blunt Body; $M = 5.85, \alpha = 0^\circ, B_x = B_y = 0, B_z = 0.04 T$	99
6.6	Velocity Contours in the $x - y$ Plane for Supersonic Flow Past an Axisymmetric Blunt Body; $M = 5.85, \alpha = 0^\circ, B_x = B_y = 0, B_z = 0.04 T$	99
6.7	Dynamic Pressure Contours in the $x - y$ Plane for Supersonic Flow Past an Axisymmetric Blunt Body; $M = 5.85, \alpha = 0^\circ, B_x = B_y = 0, B_z = 0.04 T$	100
6.8	Density Profile along the Stagnation Line for Supersonic Flow Past an Axisymmetric Blunt Body; $M = 5.85, \alpha = 0^\circ, B_x = B_y = 0, B_z = 0.06 T$	102
6.9	Streamwise Velocity Profile along the Stagnation Line for Supersonic Flow Past an Axisymmetric Blunt Body; $M = 5.85, \alpha = 0^\circ, B_x = B_y = 0, B_z = 0.06 T$	102
6.10	Temperature Profile along the Stagnation Line for Supersonic Flow Past an Axisymmetric Blunt Body; $M = 5.85, \alpha = 0^\circ, B_x = B_y = 0, B_z = 0.06 T$	103

6.11	Thermal Pressure Profile along the Stagnation Line for Supersonic Flow Past an Axisymmetric Blunt Body; $M = 5.85, \alpha = 0^\circ, B_x = B_y = 0, B_z = 0.06 \text{ T}$	103
6.12	Density Contours in the $x - y$ Plane for Supersonic Flow Past an Axisymmetric Blunt Body; $M = 5.85, \alpha = 0^\circ, B_x = B_y = 0, B_z = 0.06 \text{ T}$	104
6.13	Velocity Contours in the $x - y$ Plane for Supersonic Flow Past an Axisymmetric Blunt Body; $M = 5.85, \alpha = 0^\circ, B_x = B_y = 0, B_z = 0.06 \text{ T}$.	104
6.14	Dynamic Pressure Contours in the $x - y$ Plane for Supersonic Flow Past an Axisymmetric Blunt Body; $M = 5.85, \alpha = 0^\circ, B_x = B_y = 0, B_z = 0.06 \text{ T}$	105
6.15	Comparison of Density Profiles along the Stagnation Line for Euler and MHD Supersonic Flow Past an Axisymmetric Blunt Body; $M = 5.85, \alpha = 0^\circ, B_x = B_y = 0, B_z = 0.04 \text{ T}$ and $B_z = 0.06 \text{ T}$	107
6.16	Comparison of Velocity Profiles along the Stagnation Line for Euler and MHD Supersonic Flow Past an Axisymmetric Blunt Body; $M = 5.85, \alpha = 0^\circ, B_x = B_y = 0, B_z = 0.04 \text{ T}$ and $B_z = 0.06 \text{ T}$	108
6.17	Comparison of Thermal Pressure Profiles along the Stagnation Line for Euler and MHD Supersonic Flow Past an Axisymmetric Blunt Body; $M = 5.85, \alpha = 0^\circ, B_x = B_y = 0, B_z = 0.04 \text{ T}$ and $B_z = 0.06 \text{ T}$	109
6.18	Comparison of Temperature Profiles along the Stagnation Line for Euler and MHD Supersonic Flow Past an Axisymmetric Blunt Body; $M = 5.85, \alpha = 0^\circ, B_x = B_y = 0, B_z = 0.04 \text{ T}$ and $B_z = 0.06 \text{ T}$	110
6.19	Comparison of Total Pressure Profiles along the Stagnation Line for Euler and MHD Supersonic Flow Past an Axisymmetric Blunt Body; $M = 5.85, \alpha = 0^\circ, B_x = B_y = 0, B_z = 0.04 \text{ T}$ and $B_z = 0.06 \text{ T}$	111

List of Symbols

Symbols

\mathbf{A}	Jacobian matrix
a	speed of sound
a_f	fast magneto-acoustic speed
a_s	slow magneto-acoustic speed
\hat{a}	dummy variable
\vec{B}	magnetic field vector
C_p	constant pressure specific heat
C_v	constant volume specific heat
\vec{c}	thermal or peculiar velocity vector
e_t	specific total energy
\vec{E}	electric field vector
\mathbf{F}	flux vector
f	probability density distribution function
$f^{(0)}$	Maxwellian probability density distribution function
\vec{f}	magnetic force per unit volume
h_t	specific total enthalpy ($\equiv e_t + \frac{1}{\rho}p_o$)
\mathbf{I}	3×3 identity matrix
$\hat{i}, \hat{j}, \hat{k}$	Cartesian orthogonal unit vectors

$J(f, f_1)$	collision integral governing the collisional interaction between the particles associated with the distribution function f and the particles associated with f_1
\mathcal{J}	Jacobian of coordinate system transformation
\vec{J}	volume current density vector
\mathcal{M}	Mach number
\vec{M}	specific momentum vector
m	molecular mass
n	macroscopic number density
p	thermodynamic pressure
p_o	total pressure ($\equiv p + \frac{1}{2}\vec{B} \cdot \vec{B}$)
\mathbf{Q}	conserved variables (field) vector
R	ideal gas constant
\Re	the set of real numbers
\vec{S}	velocity ratio vector ($\equiv \vec{u}\sqrt{\beta}$)
T	temperature
t	time
\vec{u}	fluid velocity vector
\mathbf{V}	primitive variables vector
\vec{v}	molecular velocity vector
\vec{w}	Alfven wave velocity vector ($\equiv \frac{1}{\sqrt{\rho\mu_o}}\vec{B}$)

Greek Symbols

β	equivalent temperature
---------	------------------------

δ	Kronecker delta tensor
ϵ	non-translational kinetic energy (internal energy)
ϵ_o	average internal energy $\left(\equiv \left(\frac{1}{\gamma-1} - \frac{3}{2}\right) RT\right)$
ϵ_t	total kinetic energy $\left(\equiv \frac{1}{2}\vec{v} \cdot \vec{v} + \epsilon\right)$
γ	the ratio of specific heats $\left(\equiv \frac{C_p}{C_v}\right)$
λ	eigenvalue
μ_o	permeability of free space $\left(\equiv 4\pi \times 10^{-7} \text{ henry/metre}\right)$
ξ, η, ζ	generalized curvilinear coordinates
π	the ratio of the circumference of a circle to its diameter (≈ 3.141592654)
ρ	density
ϕ	solution of the Poisson equation employed to minimize the numerical divergence of the magnetic field
Ψ	collision invariants vector $\left(\equiv \left\{ m \quad m\vec{v} \quad \frac{1}{2}m\vec{v} \cdot \vec{v} + m\epsilon \right\}\right)$

Subscript/Superscript

x, y, z	components of Cartesian coordinate system
ξ, η, ζ	components of generalized curvilinear coordinate system

Abbreviations

AUSM	Advection Upwind Split Method
BGK	Bhatnagar-Gross-Krook
CFL	Courant-Friedrichs-Lewy
EFM	Equilibrium Flux Method
ERK	Explicit Runge-Kutta
FVS	Flux-Vector Split

KFVS	Kinetic Flux-Vector Split
KWPS	Kinetic Wave/Particle Split
MHD	Magnetohydrodynamics
MUSCL	Monotone Upstream-centered Schemes for Conservation Laws
PPM	Partially Parabolic Method
RK	Runge-Kutta
<i>SI</i>	International System of Units
TVD	Total Variation Diminishing
WPS	Wave/Particle Split

Abstract

The objective of this dissertation is to develop and apply kinetic schemes for the numerical solution of 3-D compressible Euler and ideal Magnetohydrodynamic (MHD) equations. By employing the so-called “*moment method strategy*”, kinetic schemes for the compressible Euler and ideal MHD equations are derived from the collisionless Boltzmann equation, which is “*upwind*” discretized. Then the moments of the “*upwind*” discretized collisionless Boltzmann equation are taken with a collision invariant vector and the appropriate distribution function to obtain the numerical scheme for the continuum Euler and ideal MHD equations.

The well-known Kinetic Flux-Vector Splitting (KFVS) algorithm is obtained by upwind discretizing the collisionless Boltzmann equation based on the sign of the molecular velocity \vec{v} . However, if the molecular velocity is expressed as $\vec{v} = \vec{u} + \vec{c}$, where \vec{u} is the fluid velocity and \vec{c} is the thermal velocity, and the Boltzmann equation is upwind discretized depending upon the sign of both \vec{u} and \vec{c} , the “*moment method strategy*” leads to the so-called Kinetic Wave/Particle Splitting (KWPS) algorithm.

In this dissertation, for both the Euler and ideal MHD equations, initially the first-order accurate time-explicit KFVS and KWPS algorithms are derived, and then the first-

order accurate time-implicit KFVS and KWPS algorithms are developed. The derivations are presented in the 3-D generalized coordinate system. A 3-D computational code for the solution of compressible Euler and ideal MHD equations in generalized curvilinear coordinate system is written and validated. The code has been written for the first-order time-explicit KWPS algorithm. However, it can be easily extended to include the time-implicit KWPS algorithm as well as both the time-explicit and time-implicit KFVS algorithms. The code is applied to calculate the inviscid Supersonic flow past an axisymmetric blunt body with and without the presence of a magnetic field. The effect of magnetic field in reducing the strength of the bow shock is analyzed.

This dissertation makes a fundamental contribution to the development and application of kinetic schemes for the solution of fluid dynamics equations.

Chapter 1

Introduction

Major developments have been achieved in numerical methods for the solution of the hyperbolic conservation law in the past three decades. Among them, there are several methods that can be categorized as characteristics based upwind schemes. These schemes either split the flux-vector or the flux-difference across a cell interface into positive and negative parts using the eigenvalues of the system. The positive or negative flux-vector or flux-difference is then discretized employing a backward or forward difference operator respectively. The Steger-Warming upwind Flux-Vector Splitting (FVS) scheme [32] and the van Leer FVS [35] are the examples of well-known FVS schemes. In addition, based on an approximate Riemann solver, the Roe [30] and Osher schemes [34, 35] are among the well-known Flux-Difference Splitting (FDS) schemes. There are other formulations that apply the FVS to the flux-vector after separating it in two parts, one without any pressure terms and the other with pressure terms. The well known schemes in this category include Liou's Advection Upwind Split Method (AUSM) [18], and Halt & Agarwal's Wave/Particle Split (WPS) [2] scheme.

1.1 Kinetic Schemes for the Euler Equations

For dilute enough gases where binary collisions between gas molecules can be assumed to dominate, the Boltzmann equation can be written as:

$$\frac{\partial (nf)}{\partial t} + \vec{v} \cdot \nabla (nf) = \left[\frac{\partial (nf)}{\partial t} \right]_{coll} = J(f, f_1) \quad (1.1)$$

where t is the time, n is the particle number density, f is the probability density distribution function, and \vec{v} is the molecular velocity. The collision integral operator $J(f, f_1)$ describes the collision of the gas particle associated with distribution function f with another particle associated with distribution function f_1 . $J(f, f_1)$ drives the distribution function towards collisional equilibrium. In Cartesian coordinate system the operator ∇ is defined as:

$$\nabla = \hat{i} \frac{\partial}{\partial x} + \hat{j} \frac{\partial}{\partial y} + \hat{k} \frac{\partial}{\partial z}$$

where $\hat{i}, \hat{j}, \hat{k}$ are the Cartesian orthogonal unit vectors.

The kernel of the collision integral J vanishes for a gas in a state of collisional equilibrium, and the Boltzmann equation has a form similar to that of the linear wave equation [5]. In literature, many schemes have been developed to solve the linear wave equation, e.g. first- and second-order upwind schemes, Lax-Wendroff method, Euler implicit scheme, and Crank-Nicholson scheme [15, 34]. From statistical perspective [17, 5], the solution for the distribution function f is the Maxwellian probability density distribution function $f^{(0)}$.

During a collision, conserved quantities are mass (m), momentum ($m\vec{v}$), and total energy ($m\epsilon_t$), which are grouped together in the collision invariants vector Ψ . Note that the specific total energy ϵ_t is a sum of the kinetic energy $\frac{1}{2}\vec{v} \cdot \vec{v}$ and the internal energy ϵ . It can be shown that the Euler equations are obtained when moments of the Boltzmann

equation are taken with the collision invariants using the Maxwellian as the weighting function. By taking the moments of the discretized Boltzmann equation with the collision invariant vector and Maxwellian probability density distribution function, it is argued that one can develop numerical schemes for the solution of the Euler equations. The schemes that utilize this strategy are called the kinetic schemes.

There exist two major approaches towards the development of kinetic schemes. In the older and more established approach, the flux vector in the collisionless Boltzmann equation is upwind discretized depending upon the sign of the molecular velocity \vec{v} . Moments of this “upwind” discretized Boltzmann equation are then taken with the collision invariant vector $\Psi \left(\equiv \left\{ 1 \quad \vec{v} \quad \frac{1}{2} \vec{v} \cdot \vec{v} + \epsilon \right\} \right)$ and the equilibrium distribution function (Maxwellian) $f^{(0)}$ as a weighting function to obtain the so called Kinetic Flux-Vector Splitting (KFVS) scheme for the Euler equations. It was first proposed by Pullin[25] and further developed by Deshpande [10] and Mandal & Deshpande [21]. This scheme, however, requires the evaluation of computationally expensive error functions. The other approach, proposed by Agarwal & Acheson [1], results in the so called Kinetic Wave/Particle Splitting (KWPS) scheme. In this scheme, the molecular velocity \vec{v} is decomposed in two parts as $\vec{v} = \vec{u} + \vec{c}$ where \vec{u} is the average fluid velocity of the gas and \vec{c} is the thermal (or peculiar) velocity. The flux-vector in the Boltzmann equation is thus divided into two parts: the convective part based on \vec{u} and the acoustic part based on \vec{c} . Both the convective and the acoustic parts in the Boltzmann equation are then “upwind” discretized and converted into a numerical scheme for the Euler equations using the moment method strategy. This approach results into the KWPS scheme, which does not require the evaluation of error functions, thereby tends to increase the computational efficiency.

There have been several important extensions to the basic kinetic schemes in the past two decades. Eppard & Grossman [12] extended the KFVS scheme for computing flows

in chemical and thermal non-equilibrium. Ravichandran [26] applied the compact differencing to the KFVS scheme to improve the spatial accuracy. Reksoprodjo [27] derived a higher-order accurate kinetic wave/particle flux-splitting algorithm for the Euler equations. Higher-order accuracy has also been obtained through interpolation of the flow variables, most notably in the q-KFVS scheme of Deshpande [9, 11], which employs the entropy variables instead of the state or the primitive variables; this formulation also ensures the positivity of the scheme. Estivalezes & Villedieu [14, 13] proposed a second-order KFVS scheme based on Taylor series expansion applied to the Maxwellian probability density distribution function. Similar approach was applied to the development of higher-order KWPS scheme by Reksoprodjo & Agarwal [28], who devised a systematic methodology to increase the accuracy to any desired order. Furthermore, they also developed the implicit kinetic schemes, both for the KFVS and KWPS algorithms. In another approach, Xu [23, 37, 38] has employed the BGK collisional model in the Boltzmann equation to reduce the diffusivity of the KFVS and KWPS schemes.

1.2 Kinetic Schemes for the Ideal Magnetohydrodynamics Equations

During the last decade, the kinetic schemes for the Euler equations have been extended to solve the ideal MHD equations. By employing the kinetic schemes, the 1-D (*7-wave*) MHD system has been extensively studied, and the results are in excellent agreement with those obtained with other non-kinetic schemes. Achievements of Croisille et al. [8], Xu [36, 33], and Reksoprodjo & Agarwal [29] are the most notable in the application of kinetic schemes to ideal MHD equations. The key problem in the development of

kinetic schemes for MHD equations has been the difficulty in obtaining a probability density distribution function for ideal MHD flow equations and the magnetic induction equations. However, by adding an acceleration term to the Boltzmann equation, which recovers the fluid portion of the ideal MHD equations, Huba & Lyon [16] have derived a distribution function. Agarwal & Reksoprodjo [3] have made another breakthrough; they have successfully derived the implicit kinetic schemes for both the Euler equations and the ideal MHD equations.

Chapter 2

Derivations of the Kinetic Schemes for the Euler Equations

The Chapman-Enskog expansion of the classical Boltzmann equation with Knudsen number (K_n) as a small parameter is used to determine the higher-order distribution functions which represent the small departure from the equilibrium. In the Chapman-Enskog expansion, the leading term represents the equilibrium distribution function $f^{(0)}$ known as the Maxwellian distribution function. The moments of Boltzmann equation with collision invariant vector Ψ and distribution function $f^{(0)}$ result in the Euler equations. The distribution function $f^{(1)}$ corresponding to $O(K_n)$ in the Chapman-Enskog expansion represents the small departure from equilibrium such that the moments of the Boltzmann equation with collision invariant vector Ψ and the distribution function $\{f^{(0)} + K_n f^{(1)}\}$ result in the Navier-Stokes equations. Similarly the moments of the Boltzmann equation with collision invariant vector Ψ and the distribution function $\{f^{(0)} + K_n f^{(1)} + K_n^2 f^{(2)}\}$ result in Burnett equations and so on. Thus the kinetic schemes for the Euler, Navier-

Stokes and Burnett equations can be derived by applying the “*moment method strategy*” to the “*upwind*” discretized Boltzmann equation. In this chapter, the time-explicit and time-implicit kinetic schemes — KFVS and KWPS are derived for the 3-D Euler equations in curvilinear coordinate system.

2.1 Connection between the Boltzmann Equation and the Euler Equations

The Boltzmann equation (1.1) governs the time evolution of a gas particle associated with a probability density distribution function f as it convects and collides with other particles. The collision process drives the distribution function toward collisional equilibrium. The mathematical link between the Boltzmann equation at the molecular level and the continuum equations of fluid flow is based on the “*moment method strategy*”, defined as the following linear mapping:

$$\langle f \Psi \rangle = \int_{\mathfrak{R}^+} d\epsilon \int_{\mathfrak{R}^3} d^3v (f \Psi) \quad (2.1)$$

where f is the probability density distribution function defining the state of the gas and Ψ is the collision invariant vector. The integration in equation (2.1) is carried out over the positive space of internal energy ϵ and over the entire three-dimensional velocity space d^3v .

The mapping of the Boltzmann equation (1.1) to the continuum level is then expressed by the following operation:

$$\left\langle \left(\frac{\partial (nf)}{\partial t} + v_i \frac{\partial (nf)}{\partial x_i} \right) \psi \right\rangle = \langle J(f, f_1) \psi \rangle \quad (2.2)$$

where ψ is a collision invariant belonging to the collision invariant vector, defined as:

$$\Psi(m, \vec{v}, \epsilon) = \left[m \quad m\vec{v} \quad \frac{1}{2}m\vec{v} \cdot \vec{v} + m\epsilon \right]^T \quad (2.3)$$

such that the following operation is satisfied:

$$\langle J(f, f_1) \psi \rangle = \int_{\mathbb{R}^+} d\epsilon \int_{\mathbb{R}^3} d^3v J(f, f_1) \psi = 0 \quad (2.4)$$

This requirement is needed to ensure that the equations of the fluid flows are conserved at the continuum level.

For a gas in a state of collisional equilibrium, the collision integral vanishes, thus $J(f, f_1) = 0$ in equation (1.1). The solution to the Boltzmann equation then becomes the zeroth order probability density distribution function (Maxwellian distribution) in the Chapman-Enskog expansion given by:

$$f^{(0)} = \frac{1}{\epsilon_o} \exp\left(-\frac{\epsilon}{\epsilon_o}\right) \left(\frac{\beta}{\pi}\right)^{3/2} \exp(-\beta(\vec{v} - \vec{u}) \cdot (\vec{v} - \vec{u})) \quad (2.5)$$

where $\beta = \frac{\rho}{2p}$ is the equivalent temperature, $\rho = mn$ is the fluid density, and p is the fluid pressure. The internal energy term associated with the non-translational degrees of freedom is expressed in terms of the ideal gas constant R and temperature T as $\epsilon_o = \left(\frac{1}{\gamma-1} - \frac{3}{2}\right) RT$. Additionally, the molecular velocity \vec{v} can also be written as the sum of the fluid velocity \vec{u} and the thermal velocity \vec{c} .

Taking moments of the Boltzmann equation (1.1) with the collision invariant vector Ψ and the equilibrium distribution function $f^{(0)}$ results in the Euler equations for the conservation of mass, momentum, and total energy for a compressible inviscid gas. In all the derivations, it is assumed that the equation of state for ideal gas holds, that is:

$$p = \rho RT = \frac{\rho}{2\beta} \quad (2.6)$$

In Cartesian coordinates, the Euler equations can be written as:

$$\frac{\partial \mathbf{Q}}{\partial t} + \frac{\partial \mathbf{F}_i}{\partial x_i} = \mathbf{0} \quad (2.7)$$

where

$$\begin{aligned} \mathbf{Q} &= \left[\rho \quad \rho u_j \quad \rho e_t \right]^T \\ \mathbf{F}_i &= \left[\rho u_i \quad \rho u_i u_j + p \delta_{ij} \quad \rho u_i e_t + p u_i \right]^T \\ i, j &= 1, 2, 3 \end{aligned}$$

The total energy density is defined as $\rho e_t = \frac{1}{2} \rho \vec{u} \cdot \vec{u} + \frac{1}{\gamma-1} p$.

In the following sections (2.1.1) - (2.1.3), the details of the application of “*moment method strategy*” to the Boltzmann equation (1.1) for obtaining the Euler equations (2.7) are described. In the derivations, it is assumed that the gas is always in a state of collisional equilibrium, that is, the convected molecules experience instantaneous collisions such that the probability density distribution function f is *always* Maxwellian $f^{(0)}$.

In the derivations of the Euler equations in sections (2.1.1) - (2.1.3), the following definitions and notations are employed:

1. Non-dimensional thermal velocity and non-dimensional internal energy are defined as $\vec{c} = \sqrt{\beta} \vec{c}$ and $\hat{\epsilon} = \epsilon / \epsilon_o$ respectively;
2. The angle-brackets denote the mathematical operation of taking the moments of the arguments;
3. The subscripts i, j, k run from 1 to 3, representing the three spatial dimensions, with repeated indices implying summation over the range.

It is important to note that the Boltzmann equation is inherently three-dimensional in velocity space, which implies that the equations at the continuum level should also be three-dimensional. Therefore, the terms “1-D” and “2-D” flows within this context could be misleading; they only imply that the fluid velocity vector has 2 and 1 vanishing components of velocity in the physical space for 1-D and 2-D flows, respectively.

2.1.1 Conservation of Mass

The equation for conservation of mass is obtained by employing the mapping operation defined by equation (2.2) and substituting the collision invariant for the mass $\psi = m$:

$$\left\langle m \left(\frac{\partial (nf)}{\partial t} + v_i \frac{\partial (nf)}{\partial x_i} \right) \right\rangle = \frac{\partial}{\partial t} (\rho \langle f \rangle) + \frac{\partial}{\partial x_i} (\rho \langle v_i f \rangle) = 0 \quad (2.8)$$

where

$$\begin{aligned} \langle f \rangle &= 1 \\ \langle v_i f \rangle &= u_i \langle f \rangle + \frac{1}{\sqrt{\beta}} \langle \hat{c}_i f \rangle = u_i + 0 \end{aligned}$$

Thus, the equation for conservation of mass (2.8) becomes:

$$\frac{\partial}{\partial t} (\rho) + \frac{\partial}{\partial x_i} (\rho u_i) = 0 \quad (2.9)$$

2.1.2 Conservation of Momentum

The equation for conservation of momentum is obtained by employing the mapping operation defined by equation (2.2) and substituting the collision invariant for the

components of the momentum $\psi = mv_j$:

$$\left\langle mv_j \left(\frac{\partial (nf)}{\partial t} + v_i \frac{\partial (nf)}{\partial x_i} \right) \right\rangle = \frac{\partial}{\partial t} (\rho \langle v_j f \rangle) + \frac{\partial}{\partial x_i} (\rho \langle v_j v_i f \rangle) = 0 \quad (2.10)$$

where

$$\begin{aligned} \langle v_j f \rangle &= u_j \langle f \rangle + \frac{1}{\sqrt{\beta}} \langle \hat{c}_j f \rangle = u_j \\ \langle v_j v_i f \rangle &= u_i u_j \langle f \rangle + u_i \frac{1}{\sqrt{\beta}} \langle \hat{c}_j f \rangle + u_j \frac{1}{\sqrt{\beta}} \langle \hat{c}_i f \rangle + \frac{1}{\sqrt{\beta}} \langle \hat{c}_i \hat{c}_j f \rangle \\ &= u_i u_j + 0 + 0 + \frac{1}{2\beta} \delta_{ij} \end{aligned}$$

After substituting the equation of state (2.6) for $\frac{1}{2\beta}$, the equation for conservation of momentum (2.10) can be expressed as:

$$\frac{\partial}{\partial t} (\rho u_j) + \frac{\partial}{\partial x_i} (\rho u_i u_j) + \frac{\partial}{\partial x_j} (p) = 0 \quad (2.11)$$

2.1.3 Conservation of Total Energy

The equation for conservation of total energy is obtained by employing the mapping operation defined by equation (2.2) and substituting the collision invariant for the total energy $\psi = \frac{1}{2}mv_k^2 + m\epsilon$:

$$\begin{aligned} \left\langle \left(\frac{1}{2}mv_k^2 + m\epsilon \right) \left(\frac{\partial (nf)}{\partial t} + v_i \frac{\partial (nf)}{\partial x_i} \right) \right\rangle = \\ \frac{\partial}{\partial t} (\rho \langle \epsilon f \rangle + \rho \langle \frac{1}{2}v_k^2 f \rangle) + \frac{\partial}{\partial x_i} (\rho \langle v_i \epsilon f \rangle + \rho \langle \frac{1}{2}v_i v_k^2 f \rangle) = 0 \end{aligned} \quad (2.12)$$

where

$$\begin{aligned} \langle \epsilon f \rangle &= \epsilon_o \langle f \rangle = \epsilon_o \\ \langle v_i \epsilon f \rangle &= \epsilon_o \langle v_i f \rangle = u_i \epsilon_o \langle f \rangle + \epsilon_o \frac{1}{\sqrt{\beta}} \langle \hat{c}_i f \rangle = u_i \epsilon_o + 0 \end{aligned}$$

$$\begin{aligned}
\left\langle \frac{1}{2} v_k^2 f \right\rangle &= \frac{1}{2} u_k^2 \langle f \rangle + \frac{1}{\sqrt{\beta}} u_k \langle \hat{c}_k f \rangle + \frac{1}{2\beta} \langle \hat{c}_k^2 f \rangle = \frac{1}{2} u_k^2 + 0 + \frac{1}{4\beta} \delta_{kk} \\
\left\langle \frac{1}{2} v_i v_k^2 f \right\rangle &= \frac{1}{2} u_i u_k^2 \langle f \rangle + \frac{1}{\sqrt{\beta}} u_i u_k \langle \hat{c}_k f \rangle + \frac{1}{2\beta} u_i \langle \hat{c}_k^2 f \rangle \\
&\quad + \frac{1}{2\sqrt{\beta}} u_k^2 \langle \hat{c}_i f \rangle + \frac{1}{\beta} u_k \langle \hat{c}_i \hat{c}_k f \rangle + \frac{1}{2\beta\sqrt{\beta}} \langle \hat{c}_i \hat{c}_k^2 f \rangle \\
&= \frac{1}{2} u_i u_k^2 + 0 + \frac{1}{4\beta} u_i \delta_{kk} + 0 + \frac{1}{2\beta} u_k \delta_{ik} + 0
\end{aligned}$$

Utilizing the definition of the average internal energy (ϵ_o) and the equation of state for the ideal gas (2.6), the equation for conservation of energy (2.12) can be written as:

$$\frac{\partial}{\partial t} (\rho e_t) + \frac{\partial}{\partial x_i} (\rho u_i e_t + p u_i) = 0 \quad (2.13)$$

where the total energy is defined as $\rho e_t = \frac{1}{2} \rho u_k^2 + \frac{1}{\gamma-1} p$.

2.2 Explicit Kinetic Schemes (KFVS and KWPS) for the Euler Equations

The mathematical link between the Boltzmann equation and the continuum equations of fluid flows demonstrated in the previous section is called “moment method strategy”, which can also be employed to map an upwind algorithm for solving the Boltzmann equation to obtain the corresponding algorithm for solving the Euler equations. This methodology is the philosophical basis of all kinetic schemes.

The moments of the upwind discretized form of the Boltzmann equation result in upwind schemes for the equations for fluid flows at the continuum level. In this section, the derivations of the kinetic schemes for the numerical solution of the Euler equations, namely the KFVS and the KWPS schemes in generalized curvilinear coordinate system,

are presented. The Euler equations in a time-invariant generalized coordinate system (ξ, η, ζ) can be expressed as the follows:

$$\frac{\partial \bar{\mathbf{Q}}}{\partial t} + \frac{\partial \bar{\mathbf{F}}_\xi}{\partial \xi} + \frac{\partial \bar{\mathbf{F}}_\eta}{\partial \eta} + \frac{\partial \bar{\mathbf{F}}_\zeta}{\partial \zeta} = \mathbf{0} \quad (2.14)$$

where the overbar denotes the quantities in the generalized curvilinear coordinate system, defined as

$$\begin{aligned} \bar{\mathbf{Q}} &= \frac{1}{\mathcal{J}} \mathbf{Q} = \frac{1}{\mathcal{J}} \begin{bmatrix} \rho & \rho u_j & \rho e_t \end{bmatrix}^T \\ \bar{\mathbf{F}}_\xi &= \frac{1}{\mathcal{J}} (\xi_x \mathbf{F}_x + \xi_y \mathbf{F}_y + \xi_z \mathbf{F}_z) \\ &= \frac{\|\xi\|}{\mathcal{J}} \begin{bmatrix} \rho u_\xi & \rho u_\xi u_j + p \hat{\xi}_j & \rho u_\xi e_t + p u_\xi \end{bmatrix}^T \\ \bar{\mathbf{F}}_\eta &= \frac{1}{\mathcal{J}} (\eta_x \mathbf{F}_x + \eta_y \mathbf{F}_y + \eta_z \mathbf{F}_z) \\ &= \frac{\|\eta\|}{\mathcal{J}} \begin{bmatrix} \rho u_\eta & \rho u_\eta u_j + p \hat{\eta}_j & \rho u_\eta e_t + p u_\eta \end{bmatrix}^T \\ \bar{\mathbf{F}}_\zeta &= \frac{1}{\mathcal{J}} (\zeta_x \mathbf{F}_x + \zeta_y \mathbf{F}_y + \zeta_z \mathbf{F}_z) \\ &= \frac{\|\zeta\|}{\mathcal{J}} \begin{bmatrix} \rho u_\zeta & \rho u_\zeta u_j + p \hat{\zeta}_j & \rho u_\zeta e_t + p u_\zeta \end{bmatrix}^T \\ j &= x, y, z \end{aligned}$$

where

1. Subscripts x, y, z are associated with the Cartesian coordinate system;
2. $\|\cdot\|$ denotes the Euclidean magnitude of the transformation metric vectors $\vec{\xi}, \vec{\eta}, \vec{\zeta}$, e.g., $\|\xi\| = \sqrt{\xi_k^2} = \sqrt{\xi_x^2 + \xi_y^2 + \xi_z^2}$;
3. The hat ($\hat{\cdot}$) denotes the normalized components of the transformation metrics, and the subscripts ξ, η, ζ on the velocity components indicate the velocity components in the generalized coordinate system, which can be related to the values in the Cartesian coordinate system through a rotation operation such as $u_\xi = \hat{\xi}_k u_k$ with $k = x, y, z$.

The Jacobian of coordinate transformation is defined as:

$$\mathcal{J} = \begin{vmatrix} \xi_x & \xi_y & \xi_z \\ \eta_x & \eta_y & \eta_z \\ \zeta_x & \zeta_y & \zeta_z \end{vmatrix} = \begin{vmatrix} x_\xi & x_\eta & x_\zeta \\ y_\xi & y_\eta & y_\zeta \\ z_\xi & z_\eta & z_\zeta \end{vmatrix}^{-1}$$

Deshpande et al. [10, 11, 21] apply the idea of moment method strategy by splitting the molecular velocity (\vec{v}) into positive and negative parts. In the Cartesian coordinate system, the split-flux Boltzmann equation (1.1) becomes:

$$\frac{\partial (nf)}{\partial t} + \frac{\partial}{\partial x_i} \left(\frac{v_i + |v_i|}{2} (nf) \right) + \frac{\partial}{\partial x_i} \left(\frac{v_i - |v_i|}{2} (nf) \right) = J(f, f_1) \quad (2.15)$$

with $i = x, y, z$. After applying the simple first-order accurate upwind discretization to the Boltzmann equation (2.15) and utilizing the moment method strategy, the scheme called Kinetic Flux-Vector Splitting (KFVS) is obtained. The split-flux terms for the Euler equations in the generalized coordinate system are obtained as:

$$\bar{\mathbf{F}}_\xi^\pm = \frac{\|\xi\|}{\mathcal{J}} \left[\frac{1 \pm \text{erf}(S_\xi)}{2} \begin{bmatrix} \rho u_\xi \\ \rho u_\xi u_j + \hat{\xi}_j p \\ \rho u_\xi e_t + u_\xi p \end{bmatrix} \pm \frac{\exp(-S_\xi^2)}{2\sqrt{\pi\beta}} \begin{bmatrix} \rho \\ \rho u_j \\ \rho e_t + \frac{1}{2}p \end{bmatrix} \right] \quad (2.16)$$

where S_ξ is the $\hat{\xi}$ -component of the velocity ratio vector $\vec{S} = \vec{u}\sqrt{\beta}$, such that $S_\xi = \hat{\xi}_k S_k$ with $k = x, y, z$. The *error function* $\text{erf}(x)$ is defined as:

$$\text{erf}(x) = \frac{2}{\sqrt{\pi}} \int_0^x dt \exp(-t^2) \quad (2.17)$$

In the numerical computation this function must be calculated using numerical integration schemes such as Gaussian Quadratures [1] or polynomial approximation [24].

Agarwal & Acheson [1] proposed the Kinetic Wave/Particle Split (KWPS) scheme to upwind split the Boltzmann equation (1.1). The scheme is derived by first decomposing

the molecular velocity in the flux terms of the Boltzmann equation into fluid velocity and thermal velocity ($\vec{v} = \vec{u} + \vec{c}$), and then upwind-splitting the velocities \vec{u} and \vec{c} individually based on their signs. In the Cartesian coordinate system, the split-flux Boltzmann equation becomes:

$$\begin{aligned} \frac{\partial (nf)}{\partial t} + \frac{\partial}{\partial x_i} \left(\frac{u_i + |u_i|}{2} (nf) \right) + \frac{\partial}{\partial x_i} \left(\frac{u_i - |u_i|}{2} (nf) \right) + \\ \frac{\partial}{\partial x_i} \left(\frac{c_i + |c_i|}{2} (nf) \right) + \frac{\partial}{\partial x_i} \left(\frac{c_i - |c_i|}{2} (nf) \right) = J(f, f_1) \end{aligned} \quad (2.18)$$

After the moments are taken with respects to the collision invariants Ψ , the resulting split-flux-vectors for the Euler equations in the generalized coordinate system are obtained as:

$$\bar{\mathbf{F}}_{\xi}^{\pm} = \frac{\|\xi\|}{\mathcal{J}} \left[\frac{u_{\xi} \pm |u_{\xi}|}{2} \begin{bmatrix} \rho \\ \rho u_j \\ \rho e_t \end{bmatrix} + \frac{1}{2} \begin{bmatrix} 0 \\ \hat{\xi}_j p \\ u_{\xi} p \end{bmatrix} \pm \frac{1}{2\sqrt{\pi\beta}} \begin{bmatrix} \rho \\ \rho u_j \\ \rho e_t + \frac{1}{2} p \end{bmatrix} \right] \quad (2.19)$$

Note the simpler expressions in equation (2.19) compared to the KFVS formulation (2.16).

2.3 Implicit Kinetic Schemes for the Euler Equations

In order to increase the efficiency of the calculations for steady state cases, the implicit variants of the kinetic schemes of section 2.2 are derived in this section. For the derivation of implicit schemes, it is required to obtain the Jacobian matrices of the flux-vectors.

There are two approaches for deriving the Jacobians:

Continuum approach: the Jacobians are obtained from the flux-vectors such as the one expressed in equation (2.16) of the explicit scheme, for example $\mathbf{A}_x^\pm = \partial \mathbf{F}_x^\pm / \partial \mathbf{Q}$ in Cartesian coordinate system.

Molecular approach: the Jacobians of the Boltzmann equation are calculated first and then their moments are taken with the collision invariant vector Ψ , for example $\mathbf{A}_x^\pm = \langle v_x^\pm \partial (nf) / \partial \mathbf{Q} \Psi \rangle$ in Cartesian coordinate system.

In subsequent derivations, the Jacobians are presented as a matrix product $\mathbf{A} = \mathbf{B}\mathbf{C}^{-1}$, where \mathbf{B} and \mathbf{C} are 5×5 matrices with \mathbf{C} defined as

$$\mathbf{C} = \frac{\partial \bar{\mathbf{Q}}}{\partial \mathbf{V}} = \frac{1}{\mathcal{J}} \begin{bmatrix} 1 & 0_{1 \times 3} & 0 \\ u_j & \rho \mathbf{I} & 0_{3 \times 1} \\ \frac{1}{2} u_k^2 & \rho u_l & \frac{1}{\gamma-1} \end{bmatrix} \quad (2.20)$$

and \mathbf{V} defined as the primitive variables vector $\left(\left[\rho \quad \vec{u} \quad p \right]^T \right)$, and \mathbf{I} is a 3×3 identity matrix. Also, the subscript $j \in \{x, y, z\}$ runs vertically while the subscript $l \in \{x, y, z\}$ runs horizontally. The repeated index implies summation over the range $\{x, y, z\}$. This convention on index notations is employed in all the derivations that follow. Also, the size of the zero submatrices are subsequently dropped for brevity and to avoid clutter.

2.3.1 Continuum Approach

In the continuum (\mathcal{C}) approach, the split Jacobian matrices are obtained directly from the linearization of the flux-vectors at the continuum level. This approach is very straightforward, and the results are as follows:

For KFVS scheme:

$$\mathbf{A}_\xi^\pm = \frac{\|\xi\|}{\mathcal{J}} \left[\frac{1 \pm \operatorname{erf}(S_\xi)}{2} \mathbf{B}_\xi^1 \pm \frac{\exp(-S_\xi^2)}{2\sqrt{\pi\beta}} \mathbf{B}_\xi^2 \right] \mathbf{C}^{-1} \quad (2.21)$$

where

$$\mathbf{B}_\xi^1 = \begin{bmatrix} u_\xi & \rho \hat{\xi}_l & 0 \\ u_\xi u_j & \rho u_\xi \mathbf{I} + \rho u_j \hat{\xi}_l & \hat{\xi}_j \\ \frac{1}{2} u_\xi u_k^2 & \rho u_\xi u_l + \rho e_t \hat{\xi}_l + p \hat{\xi}_l & \frac{1}{\gamma-1} u_\xi + u_\xi \end{bmatrix}$$

$$\mathbf{B}_\xi^2 = \begin{bmatrix} \frac{1}{2} & 0 & \beta \\ \frac{1}{2} u_j + \frac{1}{2} u_\xi \hat{\xi}_j & \rho \mathbf{I} + \rho \hat{\xi}_j \hat{\xi}_l & \beta u_j - \beta u_\xi \hat{\xi}_j \\ \frac{1}{2} u_k^2 - \frac{1}{8\beta} - \frac{1}{2} e_t + \frac{1}{4} u_\xi^2 & \rho u_l + \frac{1}{2} \rho u_\xi \hat{\xi}_l & \frac{1}{\gamma-1} + \frac{3}{4} + \beta e_t - \frac{1}{2} \beta u_\xi^2 \end{bmatrix}$$

and $j, k, l = x, y, z$.

Applying the continuum approach to the KWPS scheme, the following expression is obtained:

$$\mathbf{A}_\xi^\pm = \frac{\|\xi\|}{\mathcal{J}} \left[\frac{1 - \operatorname{sgn}(\mp u_\xi)}{2} \mathbf{B}_\xi^0 + \frac{1}{2} \mathbf{B}_\xi^1 \pm \frac{1}{2\sqrt{\pi\beta}} \mathbf{B}_\xi^2 \right] \mathbf{C}^{-1} \quad (2.22)$$

where

$$\mathbf{B}_\xi^0 = \begin{bmatrix} u_\xi & \rho \hat{\xi}_l & 0 \\ u_\xi u_j & \rho u_\xi \mathbf{I} + \rho u_j \hat{\xi}_l & 0 \\ \frac{1}{2} u_\xi u_k^2 & \rho u_\xi u_l + \rho e_t \hat{\xi}_l & \frac{1}{\gamma-1} u_\xi \end{bmatrix}$$

$$\mathbf{B}_\xi^1 = \begin{bmatrix} 0 & 0 & 0 \\ 0 & 0 & \hat{\xi}_j \\ 0 & p \hat{\xi}_l & u_\xi \end{bmatrix}$$

$$\mathbf{B}_\xi^2 = \begin{bmatrix} \frac{1}{2} & 0 & \beta \\ \frac{1}{2} u_j & \rho \mathbf{I} & \beta u_j \\ \frac{1}{2} u_k^2 - \frac{1}{8\beta} - \frac{1}{2} e_t & \rho u_l & \frac{1}{\gamma-1} + \frac{3}{4} + \beta e_t \end{bmatrix}$$

and $j, k, l = x, y, z$. Note that $\operatorname{sgn}(0) \equiv 1$.

2.3.2 Molecular Approach

In the molecular (\mathcal{M}) approach, first an upwind implicit scheme is formulated for the Boltzmann equation. For example, the x -component of the flux terms is approximated as follows:

$$(v_x n f)^{t_0 + \Delta t} \approx (v_x n f)^{t_0} + \Delta t \frac{\partial (v_x n f)}{\partial t} \approx v_x (n f)^{t_0} + v_x \frac{\partial (n f)}{\partial \mathbf{Q}} \Delta \mathbf{Q} \quad (2.23)$$

where

$$\begin{aligned} \frac{\partial (n f)}{\partial \mathbf{Q}} &= (n f) \begin{bmatrix} \frac{1}{\rho} (1 + \Phi) & 2\beta c_x & 2\beta c_y & 2\beta c_z & -\frac{1}{p} \Phi \end{bmatrix} \mathbf{C}^{-1} \\ \Phi &= \frac{5}{2} - \frac{\epsilon}{\epsilon_o} - \beta c_x^2 - \beta c_y^2 - \beta c_z^2 \end{aligned}$$

The moment method strategy is then applied to obtain the split-flux Jacobians for the Euler equations. The results are then utilized in formulating the implicit kinetic schemes for the Euler equations.

Using the KFVS methodology, the split-flux Jacobians are the same as those obtained using the continuum approach, expressed in equation (2.21).

On the other hand, by applying the Kinetic Wave/Particle Split (KWPS) methodology, the resulting split-flux Jacobians for the Euler equations are obtained as:

$$\mathbf{A}_\xi^\pm = \frac{\|\xi\|}{\mathcal{J}} \left[\frac{u_\xi \pm |u_\xi|}{2} \mathbf{B}_\xi^0 + \frac{1}{2} \mathbf{B}_\xi^1 \pm \frac{1}{2\sqrt{\pi\beta}} \mathbf{B}_\xi^2 \right] \mathbf{C}^{-1} \quad (2.24)$$

where

$$\mathbf{B}_\xi^0 = \begin{bmatrix} 1 & 0 & 0 \\ u_j & \rho \mathbf{I} & 0 \\ u_k^2 & \rho u_l & \frac{1}{\gamma-1} \end{bmatrix}$$

$$\mathbf{B}_\xi^1 = \begin{bmatrix} 0 & \rho \hat{\xi}_l & 0 \\ 0 & \rho u_j \hat{\xi}_l & \hat{\xi}_j \\ 0 & \rho e_t \hat{\xi}_l + p \hat{\xi}_l & u_\xi \end{bmatrix}$$

$$\mathbf{B}_\xi^2 = \begin{bmatrix} \frac{1}{2} & 0 & \beta \\ \frac{1}{2} u_j & \rho \mathbf{I} + \rho \hat{\xi}_j \hat{\xi}_l & \beta u_j \\ \frac{1}{2} u_k^2 - \frac{1}{2} e_t - \frac{1}{8\beta} & \rho u_l + \rho u_\xi \hat{\xi}_l & \frac{1}{\gamma-1} + \frac{3}{4} + \beta e_t \end{bmatrix}$$

Note again, the simpler expressions in equations (2.24) and (2.22) compared to equation (2.21).

2.3.3 Eigenvalues of the Jacobian Matrix

Some further insights can be obtained from the eigenvalue analysis of the Jacobian matrix $\mathbf{A} = \mathbf{X}\mathbf{\Lambda}\mathbf{X}^{-1}$ where $\mathbf{\Lambda}$ is the diagonal matrix containing all the eigenvalues and \mathbf{X} is the eigenvector matrix. However, the present analysis is conducted on a simpler diagonal matrix \mathbf{D} , which is related to \mathbf{A} by the similarity transformation $\mathbf{A} = \mathbf{C}\mathbf{D}\mathbf{C}^{-1}$. Also, for simplicity, the analysis is limited to 1-D Jacobian matrix only, resulting in a cubic equation for the characteristics polynomial.

There are three Jacobian matrices that need to be considered: KFVS, KWPS_C, and KWPS_M. Their characteristic polynomials are calculated as follows.

Eigenvalues of the KFVS Scheme

The characteristic polynomial can be written as:

$$0 = \left| -\lambda \mathbf{I} + \frac{1+\text{erf}(S_x)}{2\sqrt{\beta}} \mathbf{E}_x^1 + \frac{\exp(-S_x^2)}{2\sqrt{\pi\beta}} \mathbf{E}_x^2 \right| \quad (2.25)$$

where

$$\mathbf{E}_x^1 = \begin{bmatrix} S_x & \rho\sqrt{\beta} & 0 \\ 0 & S_x & \frac{1}{\rho}\sqrt{\beta} \\ 0 & \frac{\gamma}{2\sqrt{\beta}}\rho & S_x \end{bmatrix} \quad \mathbf{E}_x^2 = \begin{bmatrix} \frac{1}{2} & 0 & \beta \\ \frac{1}{2\rho\sqrt{\beta}}S_x & 2 & -\frac{1}{\rho}S_x\sqrt{\beta} \\ -\frac{\gamma+1}{8\beta} - \frac{\gamma-1}{4\beta}S_x^2 & -\frac{\gamma-1}{2\sqrt{\beta}}\rho S_x & \frac{3\gamma+3}{4} + \frac{\gamma-1}{2}S_x^2 \end{bmatrix}$$

The calculation can be simplified if the following change of variables is applied:

$$\mathcal{K}_1 = \frac{1+\text{erf}(S_x)}{2\sqrt{\beta}} \quad \mathcal{K}_2 = \frac{\exp(-S_x^2)}{2\sqrt{\pi\beta}} \quad \bar{\lambda} = \lambda - S_x\mathcal{K}_1 - \mathcal{K}_2 \quad \bar{\gamma} = \gamma - 1$$

The characteristic polynomial can now be recast as follows:

$$\begin{aligned} 0 &= \begin{vmatrix} -\bar{\lambda} - \frac{1}{2}\mathcal{K}_2 & \rho\sqrt{\beta}\mathcal{K}_1 & \beta\mathcal{K}_2 \\ \frac{1}{2\rho\sqrt{\beta}}S_x\mathcal{K}_2 & -\bar{\lambda} + \mathcal{K}_2 & \frac{1}{\rho}\sqrt{\beta}\mathcal{K}_1 - \frac{1}{\rho}\sqrt{\beta}S_x\mathcal{K}_2 \\ -\left(\frac{\bar{\gamma}}{4\beta}S_x^2 + \frac{\bar{\gamma}+2}{8\beta}\right)\mathcal{K}_2 & \frac{\bar{\gamma}+1}{2\sqrt{\beta}}\rho\mathcal{K}_1 - \frac{\bar{\gamma}}{2\sqrt{\beta}}\rho S_x\mathcal{K}_2 & -\bar{\lambda} + \left(\frac{\bar{\gamma}}{2}S_x^2 + \frac{3\bar{\gamma}+2}{4}\right)\mathcal{K}_2 \end{vmatrix} \\ 0 &= \bar{\lambda}^3 + \bar{\lambda}^2 \left[\left(-\frac{3\bar{\gamma}}{4} - 1 - \frac{\bar{\gamma}}{2}S_x^2\right)\mathcal{K}_2 \right] + \bar{\lambda} \left[\frac{\bar{\gamma}}{2}\mathcal{K}_2^2 + \bar{\gamma}S_x\mathcal{K}_1\mathcal{K}_2 - \frac{\bar{\gamma}+1}{2}\mathcal{K}_1^2 \right] \\ &\quad + \left[\frac{\bar{\gamma}}{4}\mathcal{K}_2^3 + \frac{\bar{\gamma}}{2}S_x\mathcal{K}_1\mathcal{K}_2^2 + \left(\frac{\bar{\gamma}}{4}S_x^2 - \frac{\bar{\gamma}}{8}\right)\mathcal{K}_1^2\mathcal{K}_2 \right] \end{aligned} \quad (2.26)$$

Eigenvalues of the KWPS Scheme

The characteristic polynomial for the ‘‘continuum’’ approach can be written as:

$$0 = \left| -\lambda\mathbf{I} + \frac{1-\text{sgn}(-S_x)}{2}\mathbf{E}_x^0 + \frac{1}{2}\mathbf{E}_x^1 + \frac{1}{2\sqrt{\pi\beta}}\mathbf{E}_x^2 \right| \quad (2.27)$$

where

$$\mathbf{E}_x^0 = \begin{bmatrix} \frac{S_x}{\sqrt{\beta}} & \rho & 0 \\ 0 & \frac{S_x}{\sqrt{\beta}} & 0 \\ 0 & \frac{1}{2\beta}\rho & \frac{S_x}{\sqrt{\beta}} \end{bmatrix} \quad \mathbf{E}_x^1 = \begin{bmatrix} 0 & 0 & 0 \\ 0 & 0 & \frac{1}{\rho} \\ 0 & \frac{\gamma-1}{2\beta}\rho & 0 \end{bmatrix} \quad \mathbf{E}_x^2 = \begin{bmatrix} \frac{1}{2} & 0 & \beta \\ 0 & 1 & 0 \\ -\frac{\gamma+1}{8\beta} & 0 & \frac{3\gamma+3}{4} \end{bmatrix}$$

Define the following the variables:

$$\mathcal{K}_0 = \frac{1 - \text{sgn}(-S_x)}{2} \quad \mathcal{K}_3 = \frac{1}{2\sqrt{\pi\beta}} \quad \bar{\lambda} = \lambda - \frac{1}{\sqrt{\beta}} S_x \mathcal{K}_0 - \mathcal{K}_3 \quad \bar{\gamma} = \gamma - 1$$

With this change of variables, the characteristic polynomial can be recast as:

$$0 = \begin{vmatrix} -\bar{\lambda} - \frac{1}{2}\mathcal{K}_3 & \rho\mathcal{K}_0 & \beta\mathcal{K}_3 \\ 0 & -\bar{\lambda} & \frac{1}{2\rho} \\ -\frac{\bar{\gamma}+2}{8\beta}\mathcal{K}_3 & \frac{1}{4\beta}\rho(\bar{\gamma} + 2\mathcal{K}_0) & -\bar{\lambda} + \frac{3\bar{\gamma}+2}{4}\mathcal{K}_3 \end{vmatrix}$$

$$0 = \bar{\lambda}^3 + \bar{\lambda}^2 \left[-\frac{3\bar{\gamma}}{4}\mathcal{K}_3 \right] + \bar{\lambda} \left[-\frac{\bar{\gamma}}{4}\mathcal{K}_3^2 - \frac{\bar{\gamma}}{8\beta} - \frac{1}{4\beta}\mathcal{K}_0 \right] + \left[\frac{\bar{\gamma}}{16\beta}\mathcal{K}_3(\mathcal{K}_0 - 1) \right] \quad (2.28)$$

For the “molecular” approach, the characteristic polynomial is given as:

$$0 = \left| -\lambda \mathbf{I} + \frac{S_x + |S_x|}{2\sqrt{\beta}} \mathbf{E}_x^0 + \frac{1}{2} \mathbf{E}_x^1 + \frac{1}{2\sqrt{\pi\beta}} \mathbf{E}_x^2 \right| \quad (2.29)$$

where

$$\mathbf{E}_x^0 = \begin{bmatrix} 1 & 0 & 0 \\ 0 & 1 & 0 \\ 0 & 0 & 1 \end{bmatrix} \quad \mathbf{E}_x^1 = \begin{bmatrix} 0 & \rho & 0 \\ 0 & 0 & \frac{1}{\rho} \\ 0 & \frac{\gamma}{2\beta}\rho & 0 \end{bmatrix} \quad \mathbf{E}_x^2 = \begin{bmatrix} \frac{1}{2} & 0 & \beta \\ 0 & 2 & 0 \\ -\frac{\gamma+1}{8\beta} & 0 & \frac{3\gamma+3}{4} \end{bmatrix}$$

Again, considerable simplification can be realized by the use of following variables:

$$\mathcal{K}_3 = \frac{1}{2\sqrt{\pi\beta}} \quad \bar{\lambda} = \lambda - [\sqrt{\pi}(S_x + |S_x|) + 1] \mathcal{K}_3 \quad \bar{\gamma} = \gamma - 1$$

The characteristic polynomial can now be recast as:

$$0 = \begin{vmatrix} -\bar{\lambda} - \frac{1}{2}\mathcal{K}_3 & \frac{1}{2}\rho & \beta\mathcal{K}_3 \\ 0 & -\bar{\lambda} + \mathcal{K}_3 & \frac{1}{2\rho} \\ -\frac{\bar{\gamma}+2}{8\beta}\mathcal{K}_3 & \frac{\bar{\gamma}+1}{4\beta}\rho & -\bar{\lambda} + \frac{3\bar{\gamma}+2}{4}\mathcal{K}_3 \end{vmatrix}$$

$$0 = \bar{\lambda}^3 + \bar{\lambda}^2 \left[\left(-\frac{3\bar{\gamma}}{4} - 1 \right) \mathcal{K}_3 \right] + \bar{\lambda} \left[\frac{\bar{\gamma}}{2}\mathcal{K}_3^2 - \frac{\bar{\gamma}+1}{8\beta} \right] + \left[\frac{\bar{\gamma}}{4}\mathcal{K}_3 \left(\mathcal{K}_3^2 - \frac{1}{8\beta} \right) \right] \quad (2.30)$$

Eigenvalues of the Kinetic Schemes

The determinants for both KWPS variants are constants. However, the determinant of the KWPS_C switches its sign and becomes positive for $S_x \leq 0$. The determinant for the KWPS_M stays the same, a negative constant throughout.

Using procedures outlined above, the eigenvalues of the positive split-flux Jacobian matrices are obtained as functions of the non-dimensional fluid velocity S_x and the equivalent temperature β whose value is set to unity for the eigenvalues computations. When applied to the KFVS split-flux Jacobian matrix, it is revealed that the eigenvalues are smooth real functions of S_x . Furthermore, the eigenvalues associated with the positive flux Jacobian matrix are all positive, go to zero as S_x goes to $-\infty$, and to the non-dimensional eigenvalues of the Euler equations $(S_x, S_x \pm \sqrt{\frac{\gamma}{2}})$ as S_x goes to $+\infty$. For the KWPS split-flux Jacobian matrix, for both the *molecular* and the *continuum* approaches, the eigenvalues are positive real functions which are parallel to the non-dimensional eigenvalues of the Euler equations for positive values of S_x . For negative values of S_x , however, two eigenvalues of the *continuum* KWPS Jacobian matrix become complex numbers, and the remaining eigenvalue, a constant value, is discontinuous at $S_x = 0$. On the other hand, the eigenvalues associated with *molecular* KWPS split-flux Jacobian matrix stay continuous at $S_x = 0$, and stay constant for $S_x \leq 0$. Based on this observation, the *molecular* approach is preferred over the *continuum* approach.

Chapter 3

Derivations of the Kinetic Schemes for the Ideal MHD Equations

In the previous chapter, a systematic description of the application of the “*moment method strategy*” was presented for obtaining the kinetic schemes for the Euler equations from the “*upwind*” discretized Boltzmann equation. In this chapter, the methodology is extended for obtaining the kinetic schemes for the ideal MHD equations.

3.1 Connection between the Boltzmann Equation and the Ideal MHD Equations

Under the assumption that the viscous effects are negligible and there are no relativistic effects [22, 6], the governing equations of Magnetohydrodynamics (MHD) are given

below. Note that $\nabla = \hat{i} \frac{\partial}{\partial x} + \hat{j} \frac{\partial}{\partial y} + \hat{k} \frac{\partial}{\partial z}$ where $\hat{i}, \hat{j}, \hat{k}$ are the Cartesian orthogonal unit vectors.

Continuity equation:

$$\frac{\partial}{\partial t} (\rho) + \nabla \cdot (\rho \vec{u}) = 0 \quad (3.1)$$

Conservation of momentum:

$$\frac{\partial}{\partial t} (\rho \vec{u}) + \nabla \cdot (\rho \vec{u} \vec{u}) + \nabla (p_o) = \nabla \cdot \left(\frac{1}{\mu_o} \vec{B} \vec{B} \right) \quad (3.2)$$

Conservation of total energy:

$$\frac{\partial}{\partial t} (\rho e_t) + \nabla \cdot (\rho \vec{u} e_t + p_o \vec{u}) = \nabla \cdot \left(\frac{1}{\mu_o} \vec{B} (\vec{u} \cdot \vec{B}) \right) \quad (3.3)$$

Magnetic field induction:

$$\frac{\partial}{\partial t} (\vec{B}) = \nabla \times (\vec{u} \times \vec{B}) \quad (3.4)$$

The above equations can be combined in the following conservation form. Note that the repeated indices imply summation over the range.

$$\frac{\partial \mathbf{Q}}{\partial t} + \frac{\partial \mathbf{F}_i}{\partial x_i} = \mathbf{0} \quad (3.5)$$

The components of \mathbf{Q} and \mathbf{F} are as follows

$$\mathbf{Q} = \left[\rho \quad \rho u_j \quad \rho e_t \quad B_j \right]^T$$

$$\mathbf{F}_i = \begin{bmatrix} \rho u_i \\ \rho u_i u_j + p_o \delta_{ij} - \frac{1}{\mu_o} B_i B_j \\ \rho u_i e_t + p_o u_i - \frac{1}{\mu_o} B_i u_k B_k \\ u_i B_j - B_i u_j \end{bmatrix}$$

$$i, j, k = 1, 2, 3$$

where \vec{B} is the magnetic field and the constant μ_o is the permeability of free space ($\equiv 4\pi \times 10^{-7}$ H/m). The total pressure and total energy density are redefined to account for the magnetic field contribution as $p_o = p + \frac{1}{2\mu_o} B_k^2$ and $\rho e_t = \frac{1}{2} \rho u_k^2 + \frac{1}{\gamma-1} p + \frac{1}{2\mu_o} B_k^2$. Furthermore, the equivalent temperature is now defined as $\beta = \frac{p}{2p_o}$. Thus, the equation of state for the ideal MHD can be expressed as

$$p = \rho R T = p_o - \frac{1}{2\mu_o} B_k^2 = \frac{\rho}{2\beta} - \frac{B_k^2}{2\mu_o} \quad (3.6)$$

To establish the connection between the Boltzmann equation and the ideal MHD equations it is necessary to derive a suitable distribution function from which the continuum equations can be recovered. Previous derivations of the kinetic schemes for ideal MHD [8, 36] simply extend the flux-splitting function of the Euler equations. Recently, it has been shown [16] that a distribution function can indeed be constructed for the ideal MHD equations for the conservation of mass, momentum, and total energy, namely equations (3.1), (3.2), and (3.3). The following sections illustrate this new approach. However, the methodology does not work in connecting the Boltzmann equation to the equation of magnetic field induction (3.4). Thus, this approach will not be followed in this dissertation for the derivation of the kinetic schemes for the ideal MHD equations.

Consider the following generalized transport equation:

$$\left\langle \frac{\partial (nf)}{\partial t} \psi \right\rangle + \left\langle v_i \frac{\partial (nf)}{\partial x_i} \psi \right\rangle - \left\langle a_i \frac{\partial (\psi)}{\partial v_i} \right\rangle = 0 \quad (3.7)$$

with $\vec{w} = \frac{1}{\sqrt{\rho\mu_o}} \vec{B}$ defined as the Alfven wave velocity, and the acceleration terms $a_i = \frac{\partial}{\partial x_i} \left(\frac{1}{2} w_i^2 nf \right)$ in conjunction with the following distribution function [16]:

$$\begin{aligned} f &= \frac{1}{\epsilon_o} \exp\left(-\frac{\epsilon}{\epsilon_o}\right) \left(\frac{1}{\pi}\right)^{3/2} \prod_h \frac{\sqrt{\beta}}{\sqrt{1-w_h^2\beta}} \exp\left(-\frac{\beta c_h^2}{1-w_h^2\beta}\right) \\ &- \frac{1}{\epsilon_o} \exp\left(-\frac{\epsilon}{\epsilon_o}\right) \left(\frac{1}{\pi}\right)^{3/2} \left(\frac{c_r c_s}{8w_r w_s} - \frac{c_q^2}{8w_q^2}\right) \prod_h \frac{1}{\sqrt{4w_h^2}} \exp\left(-\frac{c_h^2}{4w_h^2}\right) \end{aligned} \quad (3.8)$$

where $i, h, q, r, s = 1, 2, 3$. In the following sections the derivation of the fluid portion of the ideal MHD equations (3.1), (3.2), and (3.3) from the generalized transport equation (3.7) is presented. Note that the angle-brackets denote the mapping operation defined by equation (2.1).

3.1.1 Conservation of Mass

By substituting $\psi = m$ in the generalized transport equation (3.7), the following equation is obtained:

$$\frac{\partial}{\partial t} (\rho \langle f \rangle) + \frac{\partial}{\partial x_i} (\rho \langle v_i f \rangle) = 0 \quad (3.9)$$

Since $\partial\psi/\partial v_i = 0$, taking the moment of equation (3.9) with $\psi = m$ we obtain:

$$\langle f \rangle = 1$$

$$\langle v_i f \rangle = u_i$$

Thus, the equation for conservation of mass (3.9) can be expressed as:

$$\frac{\partial}{\partial t} (\rho) + \frac{\partial}{\partial x_i} (\rho u_i) = 0 \quad (3.10)$$

3.1.2 Conservation of Momentum

By substituting $\psi = mv_j$ in the generalized transport equation (3.7), the following equation is obtained:

$$\frac{\partial}{\partial t} (\rho \langle v_j f \rangle) + \frac{\partial}{\partial x_i} (\rho \langle v_i v_j f \rangle) - \frac{\partial}{\partial x_j} \left(\frac{1}{2} \rho w_j^2 \langle f \rangle \right) = 0 \quad (3.11)$$

Since $\partial\psi/\partial v_i = m\delta_{ij}$, taking the moment of equation 3.11 with $\psi = mv_j$ we obtain:

$$\begin{aligned} \langle v_j \bar{f} \rangle &= u_j \\ \langle v_i v_j f \rangle &= \begin{cases} u_i u_j - w_i w_j, & i \neq j \\ u_i u_j + \frac{1}{2\beta} - \frac{1}{2} w_i w_j, & i = j \end{cases} \end{aligned}$$

Substituting for $\frac{1}{2\beta}$ from the equation of state (3.6), the equation for conservation of momentum (3.11) can be written as:

$$\frac{\partial}{\partial t} (\rho u_j) + \frac{\partial}{\partial x_i} (\rho u_i u_j - \rho w_i w_j) + \frac{\partial}{\partial x_j} \left(p_o + \frac{1}{2} \rho w_j^2 \right) - \frac{\partial}{\partial x_j} \left(\frac{1}{2} \rho w_j^2 \right) = 0$$

which simplifies to:

$$\frac{\partial}{\partial t} (\rho u_j) + \frac{\partial}{\partial x_i} \left(\rho u_i u_j - \frac{1}{\mu_o} B_i B_j \right) + \frac{\partial}{\partial x_j} (p_o) = 0 \quad (3.12)$$

3.1.3 Conservation of Total Energy

By substituting $\psi = m\epsilon + \frac{1}{2}mv_k^2$ in the generalized transport equation (3.7), the following equation is obtained:

$$\frac{\partial}{\partial t} \left(\rho \left\langle \left(\epsilon + \frac{1}{2}v_k^2 \right) f \right\rangle \right) + \frac{\partial}{\partial x_i} \left(\rho \left\langle \left(\epsilon + \frac{1}{2}v_k^2 \right) v_i f \right\rangle \right) - \frac{\partial}{\partial x_i} \left(\frac{1}{2} \rho w_i^2 \langle v_i f \rangle \right) = 0 \quad (3.13)$$

Since $\partial\psi/\partial v_i = mv_k \delta_{ik} = mv_i$, taking the moment of equation 3.13 with

$\psi = m\epsilon + \frac{1}{2}mv_k^2$ we obtain:

$$\langle \epsilon f \rangle = \epsilon_o$$

$$\begin{aligned}
\left\langle \frac{1}{2} v_k^2 f \right\rangle &= \frac{1}{2} u_k^2 + \frac{3}{4\beta} - \frac{1}{4} w_k^2 \\
\langle v_i \epsilon f \rangle &= u_i \epsilon_o \\
\left\langle \frac{1}{2} v_i v_k^2 f \right\rangle &= \frac{1}{2} u_i u_k^2 + \frac{5}{4\beta} u_i - \frac{1}{4} u_i w_k^2 - \frac{1}{2} u_i w_i^2 - w_i u_k w_k + u_i w_i^2
\end{aligned}$$

The equation for conservation of total energy (3.13) can then be written as:

$$\begin{aligned}
&\frac{\partial}{\partial t} \left(\rho \epsilon_o + \frac{1}{2} \rho u_k^2 + \frac{3}{2} p_o - \frac{1}{4} \rho w_k^2 \right) \\
&\quad + \frac{\partial}{\partial x_i} \left(\rho u_i \epsilon_o + \frac{1}{2} \rho u_i u_k^2 + \frac{5}{2} p_o u_i - \frac{1}{4} \rho u_i w_k^2 - \frac{1}{2} \rho u_i w_i^2 \right) \\
&\quad - \frac{\partial}{\partial x_i} \left(\rho w_i u_k w_k - \rho u_i w_i^2 \right) - \frac{\partial}{\partial x_i} \left(\frac{1}{2} \rho u_i w_i^2 \right) = 0
\end{aligned}$$

which, after some simplification and applying the definition of the total energy density

($\rho e_t = \frac{1}{2} \rho u_k^2 + \frac{1}{\gamma-1} p + \frac{1}{2} \rho w_k^2$), becomes:

$$\frac{\partial}{\partial t} (\rho e_t) + \frac{\partial}{\partial x_i} \left(\rho u_i e_t + p_o u_i - \frac{1}{\mu_o} B_i u_k B_k \right) = 0 \quad (3.14)$$

3.2 Derivations of the Kinetic Schemes for the Ideal MHD Equations

In section 3.1, it was shown that the ideal MHD equations can be expressed in conservation form, given by equation (3.5). These equations are:

$$\frac{\partial \mathbf{Q}}{\partial t} + \frac{\partial \mathbf{F}_i}{\partial x_i} = \mathbf{0} \quad (3.15)$$

$$\mathbf{Q} = \begin{bmatrix} \rho \\ \rho u_j \\ \rho e_t \\ B_j \end{bmatrix} \quad \text{and} \quad \mathbf{F}_i = \begin{bmatrix} \rho u_i \\ \rho u_i u_j + p_o \delta_{ij} - B_i B_j \\ \rho u_i e_t + p_o u_i - B_i u_k B_k \\ u_i B_j - B_i u_j \end{bmatrix}$$

where

1. $i, j, k = 1, 2, 3$;
2. the total pressure and total energy density are defined as $p_o = p + \frac{1}{2}B_k^2$ and $\rho e_t = \frac{1}{2}\rho u_k^2 + \frac{1}{\gamma-1}p + \frac{1}{2}B_k^2$;
3. the equivalent temperature is now defined as $\beta = \frac{\rho}{2p_o}$ to include the contribution of the magnetic field;
4. the factor $\frac{1}{\sqrt{\mu_o}}$ has been absorbed in the definition of \vec{B} for simplicity and brevity.

3.2.1 One-Dimensional Formulation

Equation (3.15) includes 8 equations: the continuity equation, the three momentum equations, total energy equation, and three induction equations. Since the eigenvalues of the Jacobian matrices associated with this system are real numbers, the system is hyperbolic [15]. Therefore, in the flowfield information is propagated through the wave speeds. Because the 8 eigenvalues can be related to the wave speeds, the terminology *8-wave* formulation is often employed for the system of equations (3.15).

Due to the solenoidal condition required on the magnetic field ($\nabla \cdot \vec{B} = 0$) by the Maxwell equations of electrodynamics, the B_x term in 1-D MHD equations becomes a constant. Therefore, the corresponding induction equation for B_x can be dropped, and the above *8-wave* system of equations (3.15) can be contracted to *7-wave* formulation for 1-D ideal MHD. The corresponding 7 eigenvalues, in non-decreasing order [22], are: $u_x - a_f$, $u_x - w_x$, $u_x - a_s$, u_x , $u_x + a_s$, $u_x + w_x$, and $u_x + a_f$; where w_x is the

x -component of the Alfvén (intermediate) wave velocity, with a_f and a_s defined as the fast and slow magneto-acoustic wave speeds:

$$\begin{aligned} a_f &= \sqrt{a_{\mathcal{M}}^2 + a_z^2} \\ a_s &= \sqrt{a_{\mathcal{M}}^2 - a_z^2} \\ a_{\mathcal{M}}^2 &= \frac{1}{2} (w_k^2 + a^2) \\ a_z^2 &= \sqrt{a_{\mathcal{M}}^4 - a^2 w_x^2} \end{aligned}$$

with $a = \sqrt{\frac{\gamma p}{\rho}}$ being the speed of sound, and $w_k^2 = w_x^2 + w_y^2 + w_z^2$.

Some of the eigenvalues can be equal to one another, depending on the values of the magnetic field components. Hence the ideal MHD equations may not remain strictly hyperbolic [7]. The following cases may arise depending upon the values of the magnetic field components:

No magnetic field: $B_x = B_y = B_z = 0$

$$w_x = 0 \quad , \quad a_f = a \quad , \quad a_s = 0$$

In this case, 5 of the eigenvalues are equal to the flow velocity u_x , and the fast magneto-acoustic speed reduces to the speed of sound a .

Zero longitudinal magnetic field: $B_x = 0$ and $B_y, B_z \neq 0$

$$w_x = 0 \quad , \quad a_f = \sqrt{w_k^2 + a^2} \quad , \quad a_s = 0$$

Again, 5 of the eigenvalues are equal.

Zero transverse magnetic field: $B_x \neq 0$ and $B_y = B_z = 0$

$$a_f = \max(|w_x|, a) \quad , \quad a_s = \min(|w_x|, a)$$

In this case, there are 2 pairs of the eigenvalues that are equal. Depending on the magnitude of B_x , either the fast or the slow magneto-acoustic wave travels with the Alfvén wave. A special case arises when $|B_x| = \sqrt{\gamma p}$. In this case, 3 pairs of eigenvalues are equal to each other ($w_x = a_f = a_s = a$).

Croisille et al [8] derived an extension of the KFVS scheme to solve the 7-wave MHD equation. Xu [36] employed a similar methodology to extend his BGK scheme to solve the ideal MHD equations. The KFVS split-flux-vectors that are obtained can be written as:

$$\mathbf{F}_x^\pm = \frac{1 \pm \text{erf}(S_x)}{2} \mathbf{F}_1 \pm \frac{\exp(-S_x^2)}{2\sqrt{\pi\beta}} \mathbf{F}_2 \quad (3.16)$$

where

$$\mathbf{F}_1 = \begin{bmatrix} \rho u_x \\ \rho u_x^2 + p_o - B_x^2 \\ \rho u_x u_y - B_x B_y \\ \rho u_x u_z - B_x B_z \\ \rho u_x e_t + p_o u_x - B_x u_k B_k \\ u_x B_y - B_x u_y \\ u_x B_z - B_x u_z \end{bmatrix} \quad \text{and} \quad \mathbf{F}_2 = \begin{bmatrix} \rho \\ \rho u_x \\ \rho u_y \\ \rho u_z \\ \rho e_t + \frac{1}{2} p_o - \frac{1}{2} B_x^2 \\ B_y \\ B_z \end{bmatrix}$$

Employing a similar strategy, the split-flux-vectors for KWPS scheme for ideal MHD equations can be obtained as follows:

$$\mathbf{F}_x^\pm = \frac{u_x \pm |u_x|}{2} \mathbf{Q} + \frac{1}{2} \mathbf{F}_1 \pm \frac{1}{2\sqrt{\pi\beta}} \mathbf{F}_2 \quad (3.17)$$

where

$$\mathbf{F}_1 = \begin{bmatrix} 0 \\ p_o - B_x^2 \\ -B_x B_y \\ -B_x B_z \\ p_o u_x - B_x u_k B_k \\ -B_x u_y \\ -B_x u_z \end{bmatrix} \quad \text{and} \quad \mathbf{F}_2 = \begin{bmatrix} \rho \\ \rho u_x \\ \rho u_y \\ \rho u_z \\ \rho e_t + \frac{1}{2} p_o - \frac{1}{2} B_x^2 \\ B_y \\ B_z \end{bmatrix}$$

The KWPS formulation of the *7-wave* ideal MHD equations, studied by Reksoprodjo & Agarwal [29], gives results that are in excellent agreement with those obtained with other schemes.

3.2.2 Multi-Dimensional Formulation

The Maxwell equations of electrodynamics require that the magnetic field (\vec{B}) remains divergence-free, which is not an easy condition to implement in the numerical schemes for MHD equations. Thus it is not straightforward to extend the numerical schemes developed for the *7-wave* 1-D ideal MHD equations to multi-dimensional MHD equations. Till now, there are several ideas that have been proposed in the literature to satisfy this requirement of divergence free magnetic field. Powell [22] utilized a clever mathematical trick to ensure that the errors associated with non-compliance of the solenoidal requirement are advected away. An alternative approach is to solve the Poisson equation $\nabla^2 \phi + \nabla \cdot \vec{B} = 0$, at the end of each time step to attain a corrected magnetic field $\vec{B} \rightarrow \vec{B} + \nabla \phi$, where ϕ is the solution of the Poisson equation.

Tang and Xu [33] proposed a multi dimensional kinetic scheme for the ideal MHD equations. The new split-flux-vectors are obtained as follows:

$$\bar{\mathbf{F}}_{\xi}^{\pm} = \frac{\|\xi\|}{\mathcal{J}} \left[\frac{1 \pm \text{erf}(S_{\xi})}{2} \bar{\mathbf{F}}_1 \pm \frac{\exp(-S_{\xi}^2)}{2\sqrt{\pi\beta}} \bar{\mathbf{F}}_2 \right] \quad (3.18)$$

where

$$\bar{\mathbf{F}}_1 = \begin{bmatrix} \rho u_{\xi} \\ \rho u_{\xi} u_j + \hat{\xi}_j p_o - B_{\xi} B_j \\ \rho u_{\xi} e_t + u_{\xi} p_o - B_{\xi} u_k B_k \\ u_{\xi} B_j - B_{\xi} u_j \end{bmatrix} \quad \text{and} \quad \bar{\mathbf{F}}_2 = \begin{bmatrix} \rho \\ \rho u_j \\ \rho e_t + \frac{1}{2} p_o - \frac{1}{2} B_{\xi}^2 \\ B_j - \hat{\xi}_j B_{\xi} \end{bmatrix}$$

The above subscript j denotes a 3×1 column vector representing Cartesian x, y, z components.

A similar flux-vector splitting can be employed for the KWPS algorithm. The split-flux-vectors are obtained as follows:

$$\bar{\mathbf{F}}_{\xi}^{\pm} = \frac{\|\xi\|}{\mathcal{J}} \left[\frac{u_{\xi} \pm |u_{\xi}|}{2} \bar{\mathbf{F}}_0 + \frac{1}{2} \bar{\mathbf{F}}_1 \pm \frac{1}{2\sqrt{\pi\beta}} \bar{\mathbf{F}}_2 \right] \quad (3.19)$$

where

$$\bar{\mathbf{F}}_0 = \begin{bmatrix} \rho \\ \rho u_j \\ \rho e_t \\ B_j - \hat{\xi}_j B_{\xi} \end{bmatrix}, \quad \bar{\mathbf{F}}_1 = \begin{bmatrix} 0 \\ \hat{\xi}_j p_o - B_{\xi} B_j \\ u_{\xi} p_o - B_{\xi} u_k B_k \\ -B_{\xi} (u_j - \hat{\xi}_j u_{\xi}) \end{bmatrix}$$

$$\text{and} \quad \bar{\mathbf{F}}_2 = \begin{bmatrix} \rho \\ \rho u_j \\ \rho e_t + \frac{1}{2} p_o - \frac{1}{2} B_{\xi}^2 \\ B_j - \hat{\xi}_j B_{\xi} \end{bmatrix}$$

3.2.3 Derivation of Implicit Kinetic Schemes for the Ideal MHD Equations

The derivation of the implicit kinetic schemes for the ideal MHD equations employs the same methodology as was used in deriving the implicit kinetic schemes for the Euler equations in section 2.3. However, due to the unavailability of a distribution function that completely describes the ideal MHD equations [16], only the continuum approach can be applied to the KFVS algorithm. The implicit KWPS algorithm for the ideal MHD equations is derived from the implicit KFVS scheme using the implicit formulation for the Euler equations as a guideline.

Homogeneity of the Ideal MHD Flux-Vector

Since the flux-vectors of the ideal MHD equations are not homogeneous of degree one with respect to the conserved variables ($(\partial \mathbf{F} / \partial \mathbf{Q}) \mathbf{Q} \neq \mathbf{F}$), an implicit scheme must be derived in a somewhat roundabout manner. MacCormack [19, 20] accomplished this by adding a dummy equation $\partial \hat{a} / \partial t = 0$, with \hat{a} being a dummy variable, to the system of equations (3.15), and modified the expressions for the magnetic field components in the equations as shown in equation (3.20). The resulting system reduces to equation (3.15) when $\hat{a} = 1$. However, the modified flux-vectors in (3.20) can be shown to be homogeneous of degree one with respect to the modified conserved variable vector. In all subsequent derivations, the expressions are given only for the ξ component of the generalized coordinate system. The expressions for η and ζ components are easily obtained by simply replacing ξ with η and ζ respectively.

The modified conserved variable vector $\bar{\mathbf{Q}}$ and the ξ -component of the modified flux

dyad $\bar{\mathbf{F}}_\xi$ can be written as follows:

$$\bar{\mathbf{Q}} = \frac{1}{\mathcal{J}} \begin{bmatrix} \rho \\ \rho u_j \\ \rho e_t \\ B_j \\ \hat{a} \end{bmatrix} \quad \text{and} \quad \bar{\mathbf{F}}_\xi = \frac{\|\xi\|}{\mathcal{J}} \begin{bmatrix} \rho u_\xi \\ \rho u_\xi u_j + \hat{\xi}_j p_o - \left(\frac{1}{\hat{a}} B_\xi\right) B_j \\ \rho u_\xi e_t + u_\xi p_o - \left(\frac{1}{\hat{a}} B_\xi\right) u_k B_k \\ u_\xi B_j - B_\xi u_j \\ 0 \end{bmatrix} \quad (3.20)$$

where the total pressure and total energy density are now defined as $p_o = p + \frac{1}{2\hat{a}} B_k^2$ and $\rho e_t = \frac{1}{2} \rho u_k^2 + \frac{1}{\gamma-1} p + \frac{1}{2\hat{a}} B_k^2$. Without loss of generality, it can be assumed that $\hat{a} \equiv 1$.

The homogeneity of the flux-vector can be shown as follows. First, note that $\bar{\mathbf{F}}_\xi$ can be expressed as:

$$\bar{\mathbf{F}}_\xi = \frac{\|\xi\|}{\mathcal{J}} \left[\begin{bmatrix} \rho u_\xi \\ \rho u_\xi u_j + \hat{\xi}_j p_o \\ \rho u_\xi e_t + u_\xi p_o \\ u_\xi B_j \\ 0 \end{bmatrix} - \left(\frac{1}{\hat{a}} B_\xi\right) \begin{bmatrix} 0 \\ B_j \\ u_k B_k \\ u_j \hat{a} \\ 0 \end{bmatrix} \right]$$

The Jacobian matrix of this flux-vector can be calculated as follows:

$$\mathbf{A}_\xi = \frac{\partial}{\partial \bar{\mathbf{Q}}} (\bar{\mathbf{F}}_\xi) = \frac{\partial}{\partial \bar{\mathbf{Q}}} \left(\frac{\|\xi\|}{\mathcal{J}} \begin{bmatrix} \rho u_\xi \\ \rho u_\xi u_j + \hat{\xi}_j p_o \\ \rho u_\xi e_t + u_\xi p_o \\ u_\xi B_j \\ 0 \end{bmatrix} \right)$$

$$- \left(\frac{1}{\hat{a}} B_\xi \right) \frac{\partial}{\partial \bar{\mathbf{Q}}} \left(\frac{\|\xi\|}{\mathcal{J}} \begin{bmatrix} 0 \\ B_j \\ u_k B_k \\ u_j \hat{a} \\ 0 \end{bmatrix} \right) - \frac{\|\xi\|}{\mathcal{J}} \begin{bmatrix} 0 \\ B_j \\ u_k B_k \\ u_j \hat{a} \\ 0 \end{bmatrix} \frac{\partial}{\partial \bar{\mathbf{Q}}} \left(\frac{1}{\hat{a}} B_\xi \right)$$

However, the last term can be dropped because $\left(\partial \left(\frac{1}{\hat{a}} B_\xi \right) / \partial \bar{\mathbf{Q}} \right) \bar{\mathbf{Q}} = 0$. Thus the 9×9 Jacobian matrix becomes:

$$\mathbf{A}_\xi = \frac{\partial}{\partial \bar{\mathbf{Q}}} (\bar{\mathbf{F}}_\xi) = \|\xi\| \begin{bmatrix} \mathbf{A}_P & \vec{b} \\ \vec{0}^T & 0 \end{bmatrix}$$

where \mathbf{A}_P is the 8×8 Jacobian matrix due to Powell [22] and

$$\vec{b} = \left[0 \quad \frac{\gamma-2}{2\hat{a}^2} \hat{\xi}_j B_k^2 \quad \frac{\gamma-2}{2\hat{a}^2} u_\xi B_k^2 \quad -\frac{1}{\hat{a}} B_\xi u_j \right]^T$$

is the 8×1 column vector associated with \hat{a} flux.

Implicit KFVS Scheme for the Ideal MHD Equations

The implicit KFVS scheme for the ideal MHD equations is derived by utilizing a methodology similar to that used in deriving the implicit KFVS scheme for the Euler equations employing the *continuum* approach. Define the matrix \mathbf{C} as:

$$\mathbf{C} = \frac{1}{\mathcal{J}} \begin{bmatrix} 1 & 0_{1 \times 3} & 0 & 0_{1 \times 3} & 0 \\ u_j & \rho \mathbf{I} & 0_{3 \times 1} & 0_{3 \times 3} & 0_{3 \times 1} \\ \frac{1}{2} u_k^2 & \rho u_l & \frac{1}{\gamma-1} & B_l & -\frac{1}{2} B_k^2 \\ 0_{3 \times 1} & 0_{3 \times 3} & 0_{3 \times 1} & \mathbf{I} & 0_{3 \times 1} \\ 0 & 0_{1 \times 3} & 0 & 0_{1 \times 3} & 1 \end{bmatrix}$$

where \mathbf{I} is the 3×3 identity matrix. The subscript j denotes a 3×1 column vector, while the subscript l indicates a 1×3 row vector. The range for j, k, l subscripts is $\{x, y, z\}$ with repeated indices signifying summation over the whole range. The sizes of the zero submatrices are dropped in the rest of this chapter for brevity and to avoid clutter.

For the Jacobian matrix of the KFVS ideal MHD split-flux-vectors, the following expression is obtained:

$$\mathbf{A}_\xi^\pm = \frac{\|\xi\|}{\mathcal{J}} \left[\frac{1 \pm \text{erf}(S_\xi)}{2} \mathbf{B}_1 \pm \frac{\exp(-S_\xi^2)}{2\sqrt{\pi\beta}} \mathbf{B}_2 \right] \mathbf{C}^{-1} \quad (3.21)$$

where

$$\mathbf{B}_1 = \begin{bmatrix} u_\xi & \rho \hat{\xi}_l & 0 & 0 & 0 \\ u_\xi u_j & \rho \hat{\xi}_l u_j + \rho u_\xi \mathbf{I} & \hat{\xi}_j & \hat{\xi}_j B_l - B_\xi \mathbf{I} & -\frac{1}{2} \hat{\xi}_j B_k^2 \\ \frac{1}{2} u_\xi u_k^2 & \rho \hat{\xi}_l h_t + \rho u_\xi u_l - B_\xi B_l & \frac{\gamma}{\gamma-1} u_\xi & 2u_\xi B_l - B_\xi u_l & -u_\xi B_k^2 \\ 0 & \hat{\xi}_l B_j - B_\xi \mathbf{I} & 0 & u_\xi (\mathbf{I} - \hat{\xi}_j \hat{\xi}_l) & -B_\xi (u_j - u_\xi \hat{\xi}_j) \\ 0 & 0 & 0 & 0 & 0 \end{bmatrix}$$

$$\mathbf{B}_2 = \begin{bmatrix} 1 & 0 & 0 & 0 & 0 \\ u_j & \rho \mathbf{I} & 0 & 0 & 0 \\ \frac{1}{2} u_k^2 & \rho u_l & \frac{1}{\gamma-1} + \frac{1}{2} & \frac{3}{2} B_l - \frac{1}{2} B_\xi \hat{\xi}_l & -\frac{3}{4} B_k^2 \\ 0 & 0 & 0 & \mathbf{I} - \hat{\xi}_j \hat{\xi}_l & 0 \\ 0 & 0 & 0 & 0 & 0 \end{bmatrix}$$

$$- \begin{bmatrix} 1 \\ u_j \\ h_t - \frac{1}{4\beta} - \frac{1}{2\rho} B_\xi^2 \\ \frac{1}{\rho} (B_j - B_\xi \hat{\xi}_j) \\ 0 \end{bmatrix} \begin{bmatrix} \frac{1}{2} \\ 0 \\ -\beta \\ -B_l \beta \\ \frac{1}{2} B_k^2 \beta \end{bmatrix}^T$$

$$+ \begin{bmatrix} 0 \\ \hat{\xi}_j - \frac{1}{\rho_o} B_\xi B_j \\ \frac{1}{2} u_\xi - \frac{1}{2\rho_o} B_\xi (2u_k B_k - u_\xi B_\xi) \\ -\frac{1}{\rho_o} B_\xi (u_j - u_\xi \hat{\xi}_j) \\ 0 \end{bmatrix} \begin{bmatrix} \frac{1}{2} u_\xi \\ \hat{\xi}_l \rho \\ -u_\xi \beta \\ -B_l u_\xi \beta \\ \frac{1}{2} B_k^2 u_\xi \beta \end{bmatrix}^T$$

Implicit KWPS Scheme for the Ideal MHD Equations

The implicit KWPS scheme for the ideal MHD equations is derived by employing the molecular approach of the implicit KWPS scheme for the Euler equations, and using the previously obtained implicit KFVS Jacobian for the MHD equations, expressed in equation (3.21), as a guiding model. The Jacobian matrix of the KWPS ideal MHD split-flux-vectors is obtained as:

$$\mathbf{A}_\xi^\pm = \frac{|\xi|}{\mathcal{J}} \left[\frac{u_\xi \pm |u_\xi|}{2} \mathbf{B}_0 + \frac{1}{2} \mathbf{B}_1 \pm \frac{1}{2\sqrt{\pi\beta}} \mathbf{B}_2 \right] \mathbf{C}^{-1} \quad (3.22)$$

where

$$\mathbf{B}_0 = \begin{bmatrix} 1 & 0 & 0 & 0 & 0 \\ u_j & \rho \mathbf{I} & 0 & 0 & 0 \\ \frac{1}{2} u_k^2 & \rho u_l & \frac{1}{\gamma-1} & B_l & -\frac{1}{2} B_k^2 \\ 0 & 0 & 0 & \mathbf{I} - \hat{\xi}_j \hat{\xi}_l & 0 \\ 0 & 0 & 0 & 0 & 0 \end{bmatrix}$$

$$\begin{aligned}
\mathbf{B}_1 &= \begin{bmatrix} 0 & \rho \hat{\xi}_l & 0 & 0 & 0 \\ 0 & \rho \hat{\xi}_l u_j & \hat{\xi}_j & \hat{\xi}_j B_l - B_\xi \mathbf{I} & -\frac{1}{2} \hat{\xi}_j B_k^2 \\ 0 & \rho \hat{\xi}_l h_t - B_\xi B_l & u_\xi & u_\xi B_l - B_\xi u_l & -\frac{1}{2} u_\xi B_k^2 \\ 0 & \hat{\xi}_l B_j - B_\xi \mathbf{I} & 0 & 0 & -B_\xi (u_j - u_\xi \hat{\xi}_j) \\ 0 & 0 & 0 & 0 & 0 \end{bmatrix} \\
\mathbf{B}_2 &= \begin{bmatrix} 1 & 0 & 0 & 0 & 0 \\ u_j & \rho \mathbf{I} & 0 & 0 & 0 \\ \frac{1}{2} u_k^2 & \rho u_l & \frac{1}{\gamma-1} + \frac{1}{2} & \frac{3}{2} B_l - \frac{1}{2} \hat{\xi}_l B_\xi & -\frac{3}{4} B_k^2 \\ 0 & 0 & 0 & \mathbf{I} - \hat{\xi}_j \hat{\xi}_l & 0 \\ 0 & 0 & 0 & 0 & 0 \end{bmatrix} \\
&- \begin{bmatrix} 1 \\ u_j \\ h_t - \frac{1}{4\beta} - \frac{1}{2\rho} B_\xi^2 \\ \frac{1}{\rho} (B_j - B_\xi \hat{\xi}_j) \\ 0 \end{bmatrix} \begin{bmatrix} \frac{1}{2} \\ 0 \\ -\beta \\ -B_l \beta \\ \frac{1}{2} B_k^2 \beta \end{bmatrix}^T \\
&+ \begin{bmatrix} 0 \\ \hat{\xi}_j - \frac{1}{p_o} B_\xi B_j \\ u_\xi - \frac{1}{p_o} B_\xi (2u_k B_k - u_\xi B_\xi) \\ -\frac{1}{p_o} B_\xi (u_j - u_\xi \hat{\xi}_j) \\ 0 \end{bmatrix} \begin{bmatrix} 0 \\ \hat{\xi}_l \rho \\ 0 \\ 0 \\ 0 \end{bmatrix}^T
\end{aligned}$$

3.2.4 Implementation of the Poisson Solver

The Maxwell's equations require that the solenoidal condition on the magnetic field is satisfied in MHD computations. One method to fulfill this requirement is to utilize a

Poisson solver. The initial step is to solve the following Poisson equation:

$$\nabla^2 \phi + \nabla \cdot \vec{B} = 0 \quad (3.23)$$

and then to adjust the magnetic field according to $\vec{B}_{k+1} = \vec{B}_k + \nabla \phi_k$. The Poisson equation (3.23) is then solved again based on the new value of the magnetic field. The application of Neumann boundary condition $\nabla_i \phi = 0$ is to guarantee that the magnetic field along the boundary is left unchanged. The Laplacian in a generalized coordinate system can be expressed as follows:

$$\begin{aligned} \nabla^2 \phi = & (\vec{\xi}, \vec{\xi}) \phi_{\xi\xi} + (\vec{\eta}, \vec{\eta}) \phi_{\eta\eta} + (\vec{\zeta}, \vec{\zeta}) \phi_{\zeta\zeta} \\ & + 2 (\vec{\xi}, \vec{\eta}) \phi_{\xi\eta} + 2 (\vec{\eta}, \vec{\zeta}) \phi_{\eta\zeta} + 2 (\vec{\zeta}, \vec{\xi}) \phi_{\zeta\xi} \\ & + \nabla^2 \xi \phi_\xi + \nabla^2 \eta \phi_\eta + \nabla^2 \zeta \phi_\zeta \end{aligned}$$

where the quantities in parentheses denote inner products and the greek subscripts denote partial differentiation, e.g., $(\vec{\xi}, \vec{\eta}) = \xi_x \eta_x + \xi_y \eta_y + \xi_z \eta_z$ and $\phi_{\xi\eta} = \frac{\partial^2 \phi}{\partial \xi \partial \eta}$. The Laplacian of the generalized coordinate component ξ can be written as follows:

$$\begin{aligned} \nabla^2 \xi = & - (\vec{\xi}, \vec{\xi}) (\xi_x x_{\xi\xi} + \xi_y y_{\xi\xi} + \xi_z z_{\xi\xi}) - 2 (\vec{\xi}, \vec{\eta}) (\xi_x x_{\xi\eta} + \xi_y y_{\xi\eta} + \xi_z z_{\xi\eta}) \\ & - (\vec{\eta}, \vec{\eta}) (\xi_x x_{\eta\eta} + \xi_y y_{\eta\eta} + \xi_z z_{\eta\eta}) - 2 (\vec{\eta}, \vec{\zeta}) (\xi_x x_{\eta\zeta} + \xi_y y_{\eta\zeta} + \xi_z z_{\eta\zeta}) \\ & - (\vec{\zeta}, \vec{\zeta}) (\xi_x x_{\zeta\zeta} + \xi_y y_{\zeta\zeta} + \xi_z z_{\zeta\zeta}) - 2 (\vec{\zeta}, \vec{\xi}) (\xi_x x_{\zeta\xi} + \xi_y y_{\zeta\xi} + \xi_z z_{\zeta\xi}) \end{aligned}$$

The Laplacian of other components η and ζ can be similarly obtained using appropriate substitutions. In addition, the following formula can be used to calculate the magnetic field divergence:

$$\begin{aligned} \nabla \cdot \vec{B} = & \xi_x (B_x)_\xi + \eta_x (B_x)_\eta + \zeta_x (B_x)_\zeta \\ & + \xi_y (B_y)_\xi + \eta_y (B_y)_\eta + \zeta_y (B_y)_\zeta \\ & + \xi_z (B_z)_\xi + \eta_z (B_z)_\eta + \zeta_z (B_z)_\zeta \end{aligned}$$

Also, the boundary conditions are applied in the generalized coordinate system as $\phi_\xi = \phi_\eta = \phi_\zeta = 0$, similar to $\phi_x = \phi_y = \phi_z = 0$ in Cartesian system. Finally, the magnetic field is updated as follows:

$$B_x = \frac{\partial \phi}{\partial x} = \xi_x \phi_\xi + \eta_x \phi_\eta + \zeta_x \phi_\zeta \quad (3.24)$$

with the other magnetic field components obtained by employing corresponding substitutions.

Chapter 4

Code Validation Test Cases

Employing a number of test cases, Reksoprodjo[27] has validated the 1-D and 2-D explicit KWPS schemes for the solution of Euler and ideal MHD equations. For the Euler code, the 1-D cases include the Sod's shock tube test case [31] and the steady-state shock structure computations. The 2-D Euler cases include the flowfield computations of a cylindrical blast-wave, and supersonic flow past an axisymmetric blunt body. For the MHD code, the 1-D case is the standard Brio & Wu magnetic shock tube test case [7]. In all the above test cases, it is clear that the explicit KWPS scheme is able to produce accurate results.

4.1 Explicit KWPS Scheme for the Euler Equations

4.1.1 One-Dimensional Test Cases for the Explicit KWPS Euler Code

The first test case used to validate the explicit KWPS schemes is the Sod's shock tube test case. A uniform grid of 2000 mesh points is employed in the computational domain. This computational domain is divided in two parts which are initially (at time $t = 0$) separated by a diaphragm, with density and pressure ratios of 8 and 10 respectively. The specific heats ratio γ is set to $\frac{7}{5}$. The CFL is defined as the ratio

$$\text{CFL} = \frac{\max(|u_x| + a)}{\Delta x} \Delta t \quad (4.1)$$

where a is the local speed of sound, and Δx is set equal to unity. The time step used is $\Delta t = 0.4$, which corresponds to $\text{CFL} \approx 0.877$, and the final solution is obtained at $t = 400$. This case is widely used as a benchmark for testing the numerical algorithms. The numerical results are compared with the analytical solution, which can be easily obtained.

In this case, a gas, initially at rest in a long infinite tube and separated by a diaphragm, is at a high pressure and density in one chamber and at a low pressure and density in the other chamber. When the diaphragm is broken, the high pressure gas expands into the low pressure side and a series of waves generate from the original location of the diaphragm: these waves constitute a compression wave, an entropy wave, and an expansion wave. With the assumption that both the ends of the tube to the diaphragm are infinitely long, the waves that emanate from the diaphragm location are assumed to never reach the ends of the tube. The flow domain spanned these three waves can be

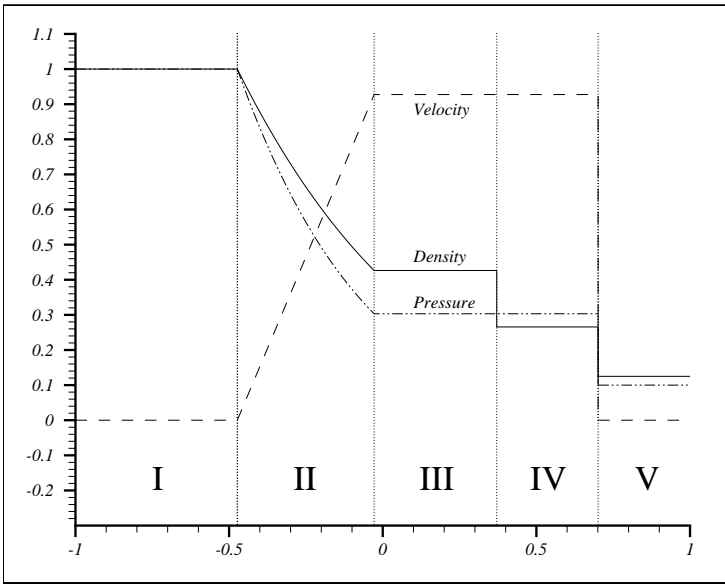


Figure 4.1: Analytical solutions for the Sod's shock tube test case [31]

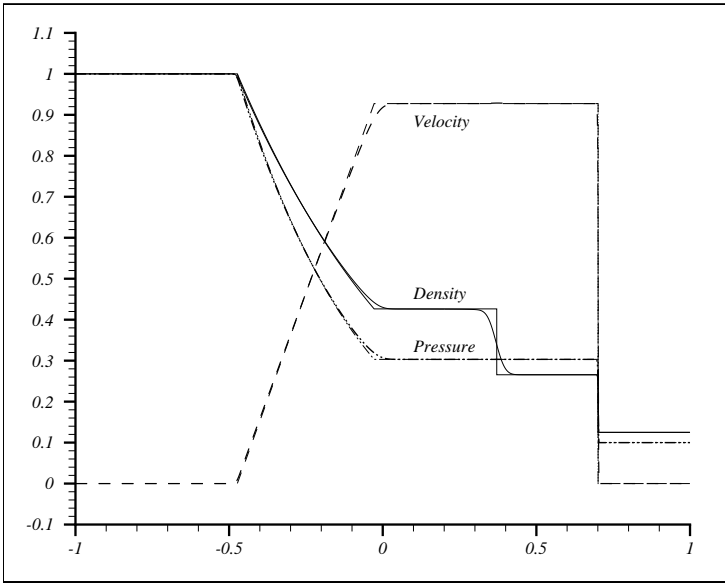


Figure 4.2: Explicit KWPS calculations for the Sod's shock tube test case [27]

divided into 5 distinct regions, as shown in Fig. (4.1). The undisturbed gas fills regions I and V. The head and the tail of the expansion wave mark the left and right borders of region II, which is called the expansion region. On the border between regions III and IV, the two gases are separated by a contact discontinuity—density shows an increase but velocity and pressure profiles stay continuous. Finally, a traveling shock is present on the boundary between regions IV and V across which all flow variables are discontinuous. The numerical solutions with the KWPS Euler solver are shown in Fig. (4.2) which compare with the analytical solutions shown in Fig. (4.1).

The second test case is the computation of the structure of a Mach 1.5 steady shock. The domain consists of 100 uniformly distributed mesh points. For Euler flow, an analytical solution can be found in standard textbooks on compressible fluid flow, e.g., the book by Anderson [4]. If the flow starts at $t = 0$, then linear variations in density, velocity, and pressure within the computational domain can be calculated using the boundary values at the left and right boundaries, which are obtained from the Rankine-Hugoniot jump relations [17] as given below:

$$\begin{aligned}\frac{\rho_r}{\rho_l} &= \frac{(\gamma + 1) \mathcal{M}_l^2}{(\gamma - 1) \mathcal{M}_l^2 + 2} \\ \frac{p_r}{p_l} &= \frac{2\gamma \mathcal{M}_l^2 - (\gamma - 1)}{\gamma + 1} \\ \mathcal{M}_r^2 &= \frac{(\gamma - 1) \mathcal{M}_l^2 + 2}{2\gamma \mathcal{M}_l^2 - (\gamma - 1)}\end{aligned}$$

where $\mathcal{M} = \frac{u_x}{a}$ is the Mach number, $a = \sqrt{\frac{\gamma p}{\rho}}$ is the speed of sound, and the subscripts l and r denote pre- and post-shock conditions. A time step of $\Delta t = 0.3$ is used for explicit KWPS scheme, which corresponds to $\text{CFL} \approx 0.890$. The solution is considered to converge when $L_2 - \text{norm} < 10^{-5}$. Results from the steady-state shock structure computations are shown in Figs. (4.3) and (4.4).

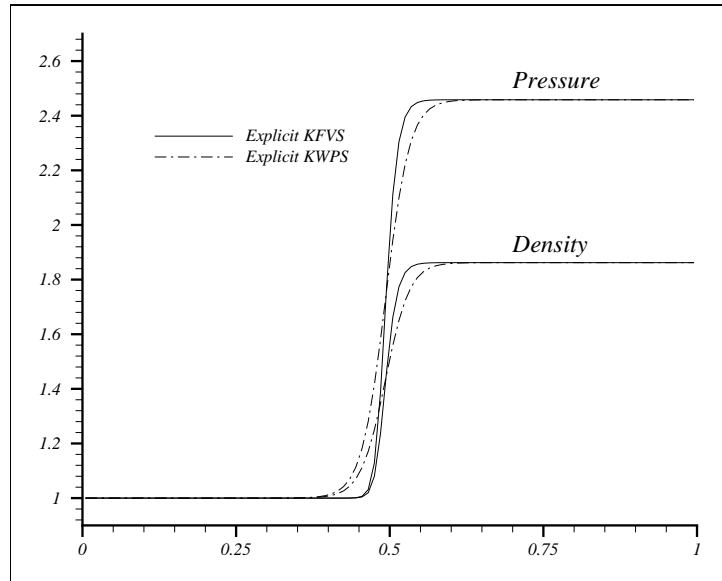


Figure 4.3: Density & pressure profiles obtained by the explicit KFVS and KWPS schemes for the shock structure computations[27]

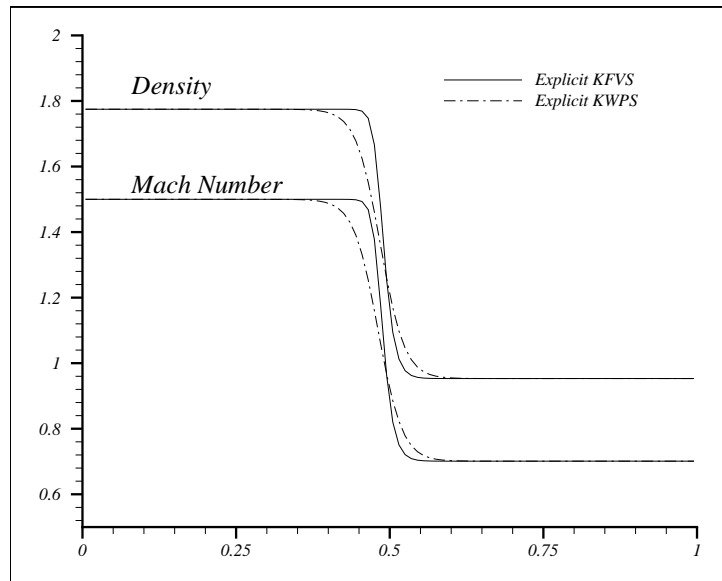


Figure 4.4: Velocity & Mach number profiles obtained by the explicit KFVS and KWPS schemes for the shock structure computations[27]

4.1.2 Two-Dimensional Test Cases for the Explicit KWPS Euler Code

In the 2-D test case of the propagation of a cylindrical blast-wave, a Cartesian square domain $L \times L$ is discretized into 100×100 grid points. In the center of the domain is a circular region $r = \frac{1}{5}L$ representing a high pressure $p_{high} = 40p_{low}$ region. The final solution is computed at $t = 2.0$, and the time step is set at $\Delta t = 0.02$ for the explicit KWPS scheme. The numerical results for the cylindrical blast-wave test case are obtained by using the KWPS scheme; the density and thermal pressure contours as shown in Fig. (4.5).

The second 2-D case is the supersonic flow past a cylindrical blunt-body, of which the leading edge is semicircular with a radius $R = 0.1$ m, and the afterbody extends to $2R$ behind the leading edge. The grid consists of 78×51 mesh points.

The inflow conditions are set to that of a uniform flow of Mach 5.85 with farfield density and pressure values of $T_\infty = 55$ K and $p_\infty = 510$ Pa. The CFL values used are 0.4 for the explicit KWPS scheme, and the solution is assumed to converge when the L_2 – norm of changes in density is less than 10^{-7} .

The density contour plots are shown in Fig. (4.6) for the explicit and the implicit KWPS scheme. The stagnation line profiles for the density, thermal pressure, and temperature are given in Figs. (4.7). It should be noted that at the stagnation point the computed numerical values of the flow variables are accurate when compared with analytical values.

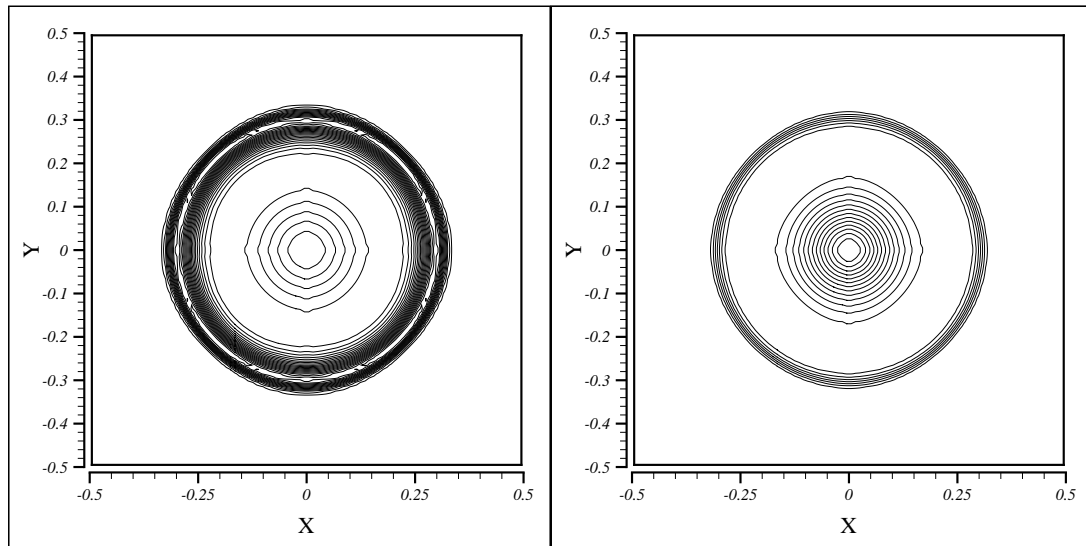


Figure 4.5: Density (L) and thermal pressure (R) contours for the cylindrical blast-wave test case

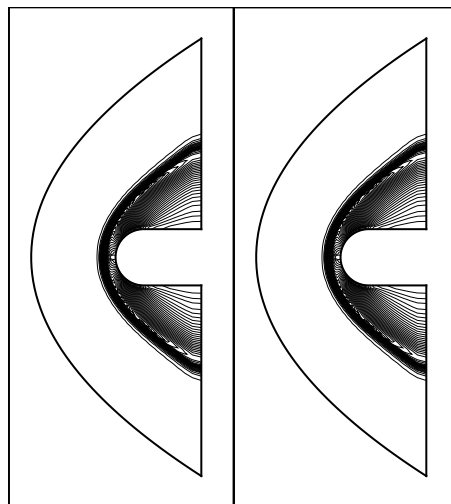


Figure 4.6: Density contour plots for the blunt-body computation using the explicit (L) and implicit (R) KWPS scheme

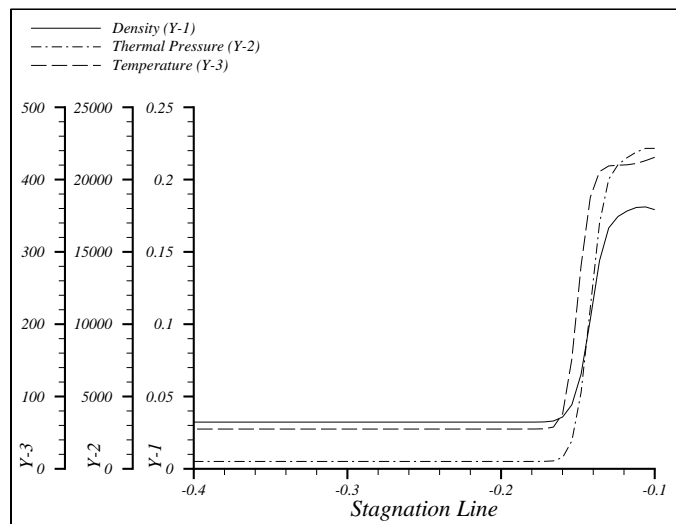


Figure 4.7: Density, thermal pressure, and temperature profiles along the stagnation line of the 2-D blunt body using the explicit KWPS scheme

4.2 Explicit KWPS Scheme for the Ideal MHD

Equations

The standard Brio & Wu [7] magnetic shock tube test case is employed to validate the explicit KWPS scheme for the ideal MHD equations. This test case is similar to that of Sod's shock tube except that the gas under investigation is a plasma subjected to a magnetic field. The initial conditions are the same as that of the Sod's shock tube test case (Section 4.1.1), with the additions of a constant longitudinal magnetic field value of $B_x = \frac{3}{4}$ and a transverse magnetic field value of $B_y = +1$ in the high density/pressure region and $B_y = -1$ in the low density/pressure region of the magnetic shock tube. The computational domain consists of 1600 mesh points. The time step is set to $\Delta t = 0.16$, which corresponds to $CFL \approx 0.390$ for the Euler case and to $CFL \approx 0.608$ for the MHD case.

The MHD code is first used to compute the flowfield without the magnetic field. Under this condition, the code is actually solving the Euler equations. After that, the magnetic field is imposed on the Euler solution. In the calculations, γ is set to 2 following Brio & Wu [7]. Final solution is obtained at $t = 160$. In the MHD shock tube, there are 5 waves present within the solution. From the left, they are a fast rarefaction wave, a compound (shock-expansion) wave, the contact discontinuity, a slow shock, and a fast rarefaction wave.

Computations with KWPS MHD solvers are in good agreement with those of Brio & Wu [7]. Figs. (4.8) - (4.10) respectively show the density, pressure and velocity profiles at $t = 160$, which are in good agreement with those computed by Brio & Wu [7]. These calculations validate the accuracy of explicit KWPS scheme for computing ideal MHD flows.

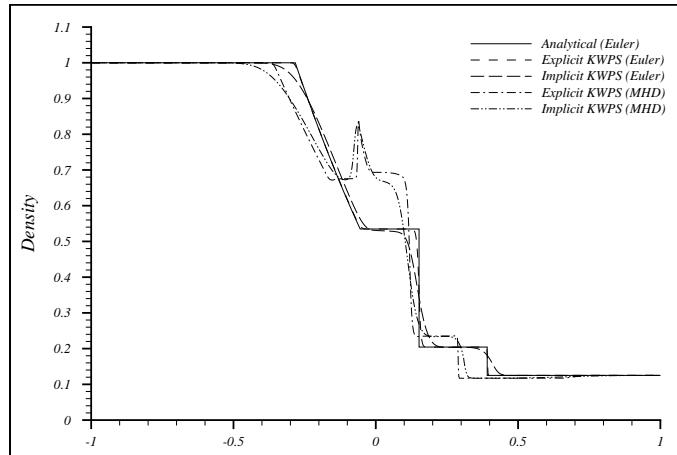


Figure 4.8: Computed Euler and Ideal MHD Density Profiles with an Explicit and Implicit KWPS Solver for Flow in a Shock Tube

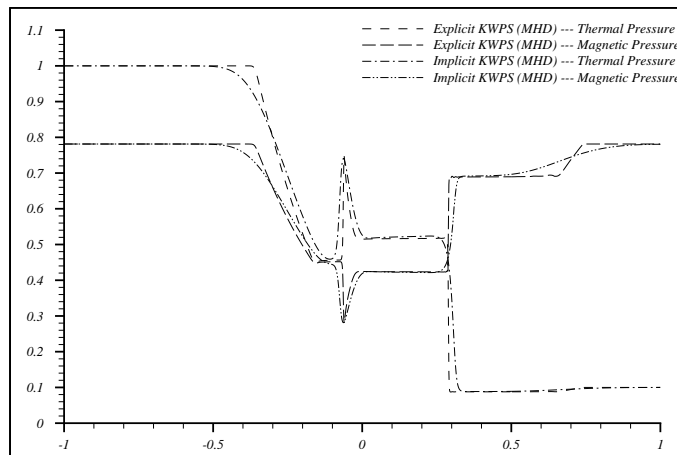


Figure 4.9: Computed Ideal MHD Thermal and Magnetic Pressure Profiles with an Explicit and Implicit KWPS Solver for Flow in a Shock Tube

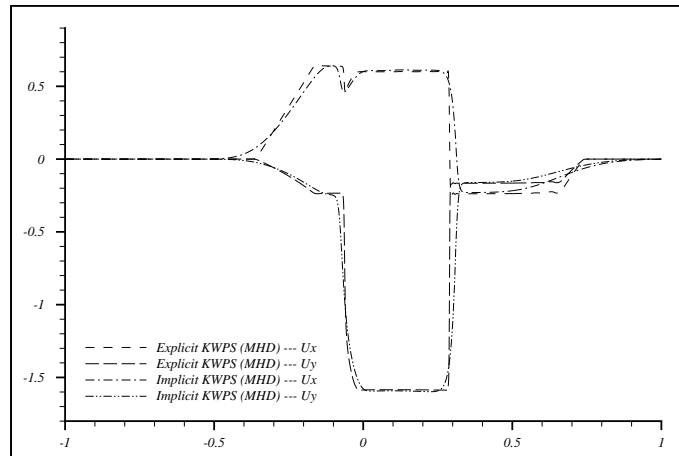


Figure 4.10: Computed Ideal MHD Velocity Profiles with an Explicit and Implicit KWPS Solver for Flow in a Shock Tube

Chapter 5

Computation of Inviscid Supersonic Flow Past an Axisymmetric Blunt Body Using the 3-D Euler solver

A 3-D computational code for solving the Euler equations in general curvilinear coordinate system was written based on the explicit KWPS scheme. The code has been applied to compute the supersonic flow past a cylindrical blunt-body at Mach 5.85 for angles of attack varying from 3° to 15° . The following sections describe the detailed results for the computed flow fields.

5.1 Computational Domain and Grid

A sketch of the computational domain is shown in Fig. (5.1), where appropriate boundaries are also identified. The leading edge of the blunt body is semi-spherical with a radius $R = 0.1$ m, and the afterbody extends to $2R$ behind the leading edge.

A structured-grid is employed for flow field calculations. The grid consists of $40 \times 51 \times 10$ mesh points for cases with an angle of attack of 0° and 3° . For angles of attack of 6° , 10° , and 15° , a finer grid of $117 \times 51 \times 10$ mesh points is used to maintain accuracy. Figures (5.2) - (5.4) show various views of the grid.

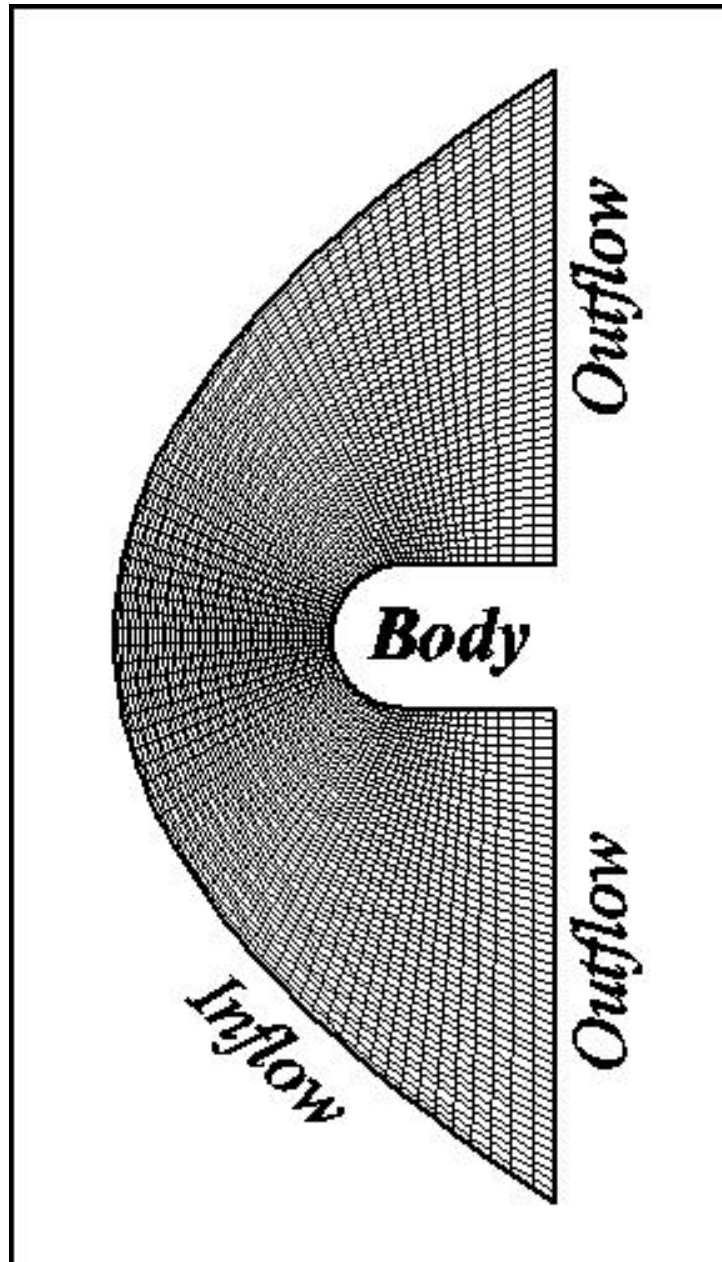


Figure 5.1: Cross-section of the computational domain for Supersonic Flow Past an Axisymmetric Blunt Body

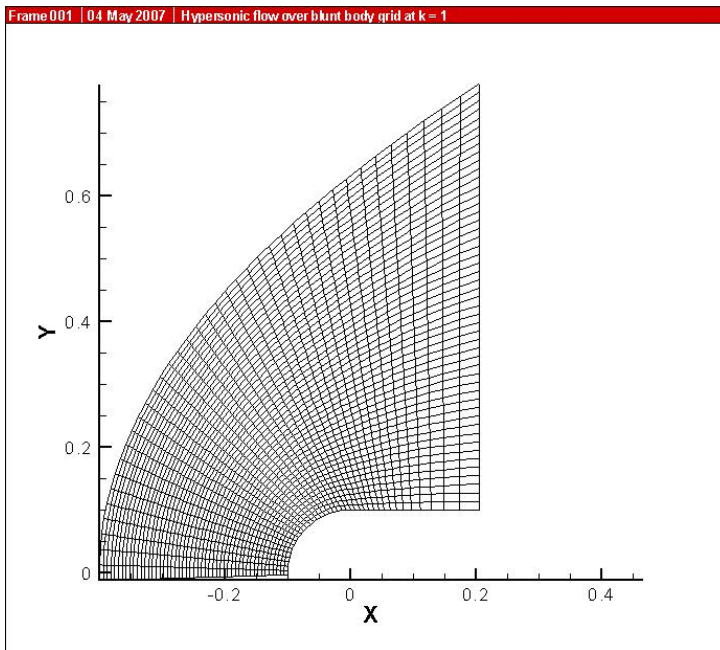


Figure 5.2: View of the Grid in the $x - y$ Plane

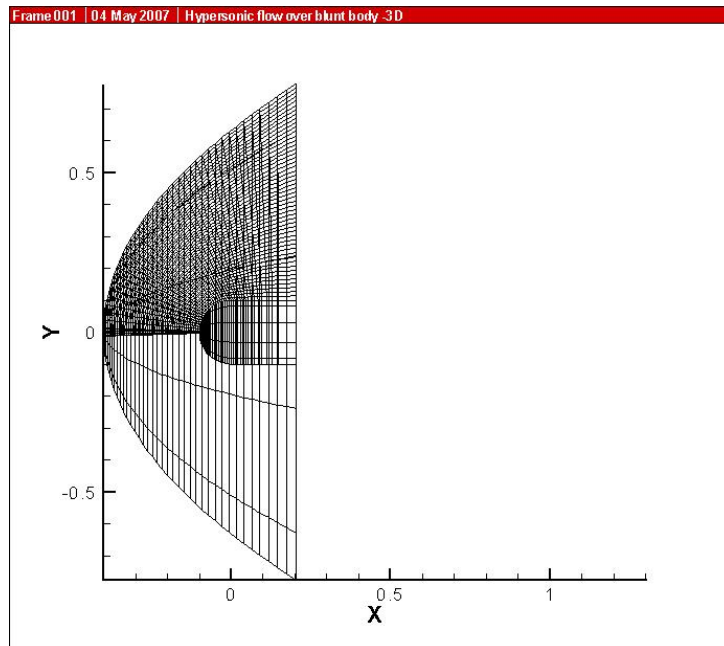


Figure 5.3: Side View of the Grid

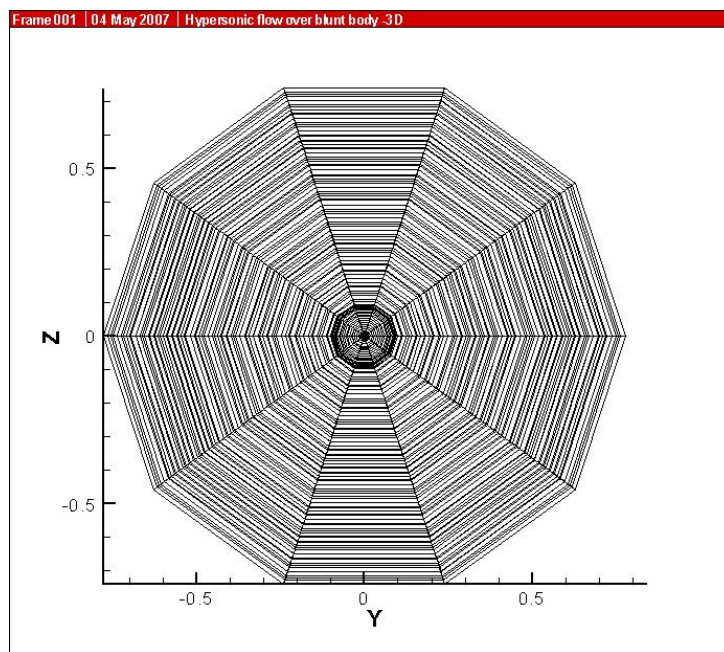


Figure 5.4: View of the Grid in the $y - z$ Plane

5.2 Flowfield Computations

Computations are performed at Mach number $M = 5.85$ at angles of attack $\alpha = 0^\circ, 3^\circ, 6^\circ, 10^\circ$ and 15°

The inflow conditions are that of a uniform flow of Mach 5.85 with farfield density and pressure values of $\rho_\infty = 0.0323 \text{ kgm}^3$ and $p_\infty = 510 \text{ Pa}$. The CFL value used is 0.4 for the KWPS explicit scheme. The solution is assumed to converge when the L_2 – norm of changes in density is less than 10^{-7} .

5.2.1 Flowfield Computations at $M = 5.85, \alpha = 0^\circ$

In this case, relatively coarse grid of $40 \times 51 \times 10$ mesh points was found to be sufficient for accurate results. Figure (5.5) shows the convergence history of the L_2 – norm of density which decreases to 10^{-7} in about 1500 iterations. Figure (5.6) shows the variation of density along the stagnation line. Figure (5.7) shows the density contours in the $x - y$ plane and Figure (5.8) shows a 3-D view of the density contours. Figure (5.9) shows the variation in the streamwise velocity along the stagnation line. Figure (5.10) shows the contours of the streamwise velocity in $x - y$ plane and figure (5.11) shows the 3-D view of the streamwise velocity. Figure (5.12) shows the variation in temperature along the stagnation line. Figure (5.13) shows the temperature contours in the $x - y$ plane and Figure (5.14) shows a 3-D view of the temperature contours. Figure (5.15) shows the variation in total pressure along the stagnation line. Figure (5.16) shows the total pressure contours in the $x - y$ plane and Figure (5.17) shows a 3-D view of the total pressure contours.

For this test case the computed shock appears at the right location as seen by the density profile along the stagnation line. The stagnation value of density is 0.1849kg/m^3 compared to the reference value of 0.0323kg/m^3 in the free-stream; the temperature and total pressure at the stagnation point increase from 55K and 0.51kPa in the free-stream to 430K and 23kPa respectively. The velocity along the stagnation line decreases from the free-stream value of 870m/s to the value of 0m/s at the stagnation point. These computed values at the stagnation point are in excellent agreement with the analytical values as shown in the table below:

Flow Variables	Units	Analytical Values	Computed Values
Density	kg/m^3	0.1834	0.1849
Total Pressure	kPa	22.704	22.510
Temperature	K	431.45	430.63

Table 5.1: Analytical and computed values of the flow variables at the stagnation point

During computation, it was found that the KWPS scheme has difficulty in converging to the correct solution when the initial conditions in the interior of the domain are set to the free-stream conditions. For moderately high Mach number, the bow shock never detaches from the body, instead it degenerates into a shock layer next to the surface. This problem has been circumvented by specifying zero velocity vector in the interior and on the solid wall, while keeping the values of density ρ and total energy e_t to that of the free-stream. In other words, instead of detaching the bow shock from the body, it is allowed to travel into the domain from the free-stream. The computed stagnation values are in excellent agreement with the analytical values. It is also found that the computed bow shock is placed correctly in the computational domain in the converged solution when compared to its analytically determined location along the stagnation line.

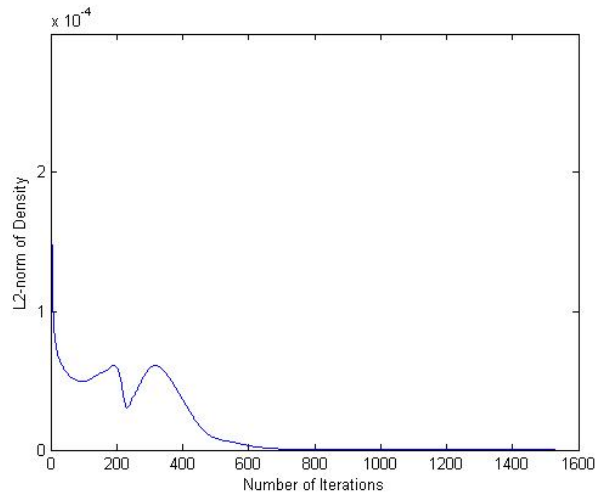


Figure 5.5: Convergent History of the L_2 – norm of Density for the Supersonic Flow Past an Axisymmetric Blunt Body; $M = 5.85, \alpha = 0^\circ$.

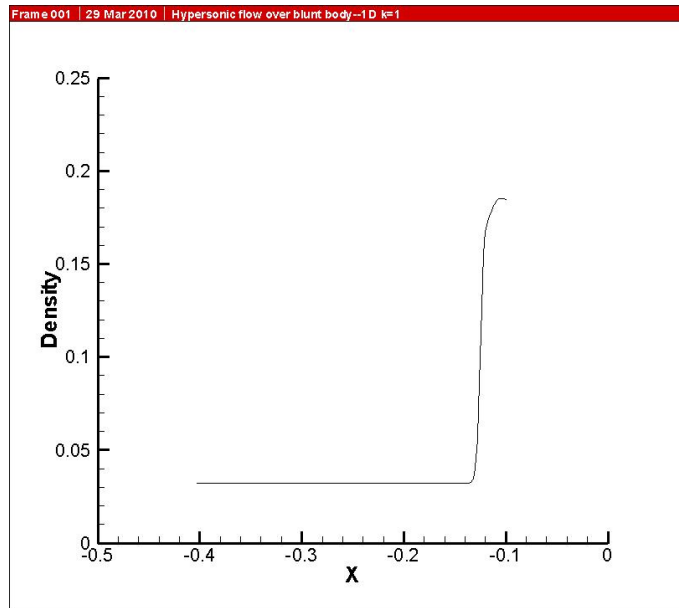


Figure 5.6: Density Profile along the Stagnation Line for Supersonic Flow Past an Axisymmetric Blunt Body; $M = 5.85, \alpha = 0^\circ$; the stagnation point - nose of the body - is at $x = -0.1$.

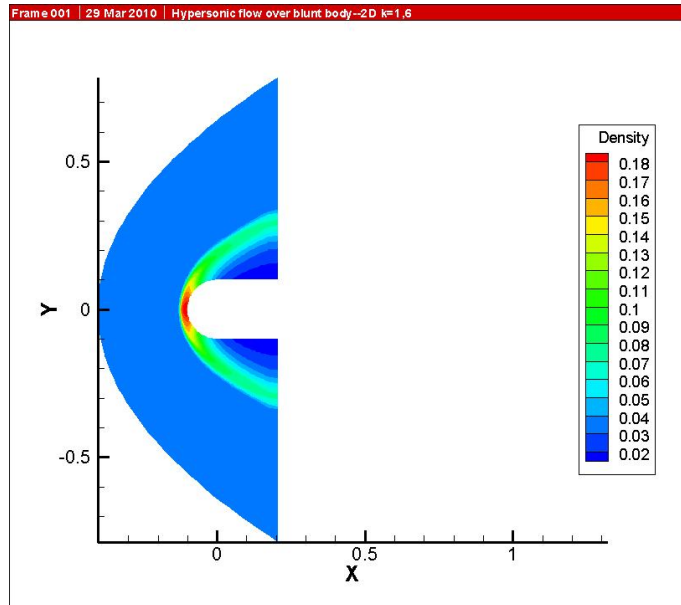


Figure 5.7: Density Contours in the $x-y$ Plane for Supersonic Flow Past an Axisymmetric Blunt Body; $M = 5.85$, $\alpha = 0^\circ$.

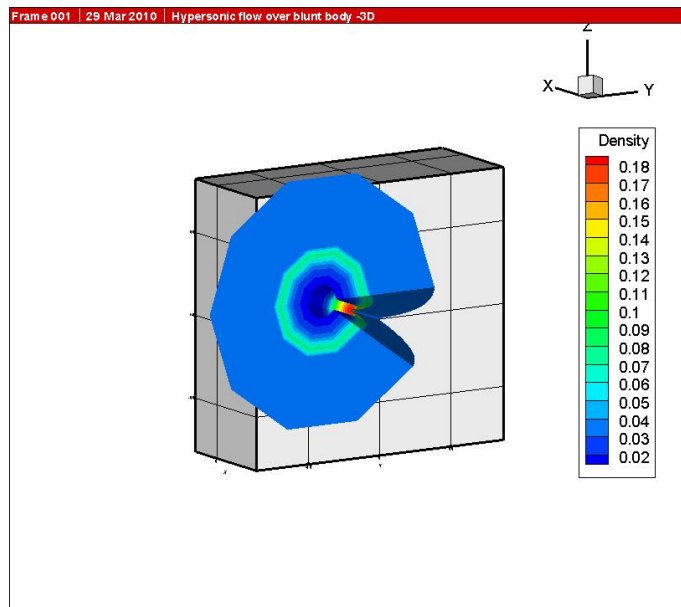


Figure 5.8: 3-D View of the Density Contours for Supersonic Flow Past an Axisymmetric Blunt Body; $M = 5.85$, $\alpha = 0^\circ$.

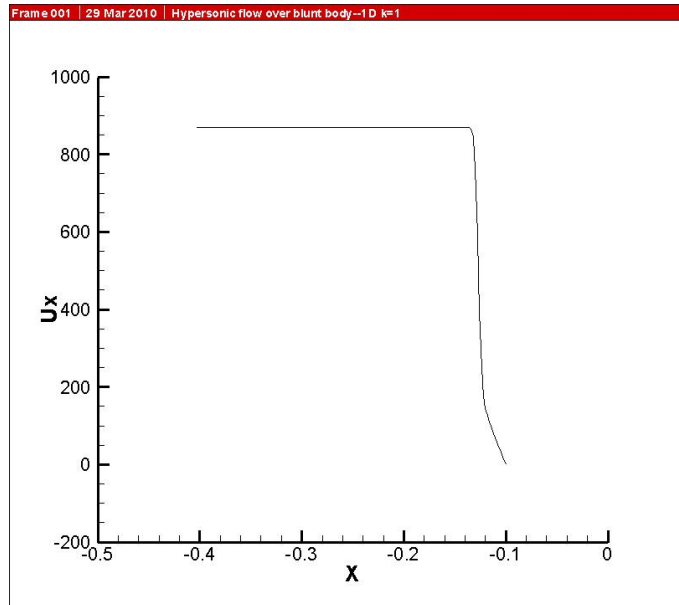


Figure 5.9: Streamwise Velocity Profile along the Stagnation Line for Supersonic Flow Past an Axisymmetric Blunt Body; $M = 5.85$, $\alpha = 0^\circ$.

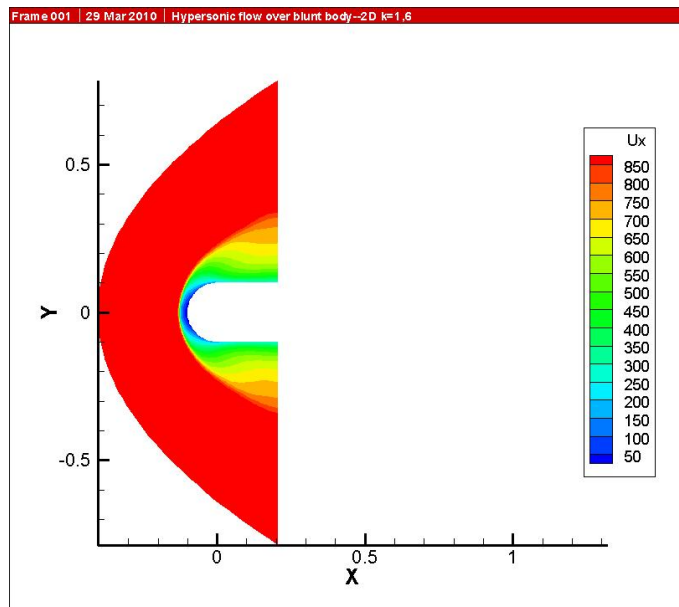


Figure 5.10: Velocity Contours in the $x - y$ Plane for Supersonic Flow Past an Axisymmetric Blunt Body; $M = 5.85$, $\alpha = 0^\circ$.

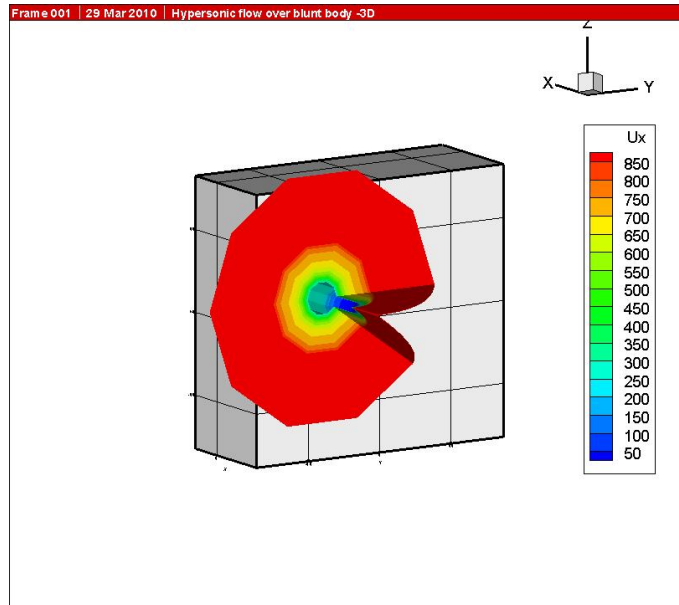


Figure 5.11: 3-D View of the Velocity Contours for Supersonic Flow Past an Axisymmetric Blunt Body; $M = 5.85$, $\alpha = 0^\circ$.

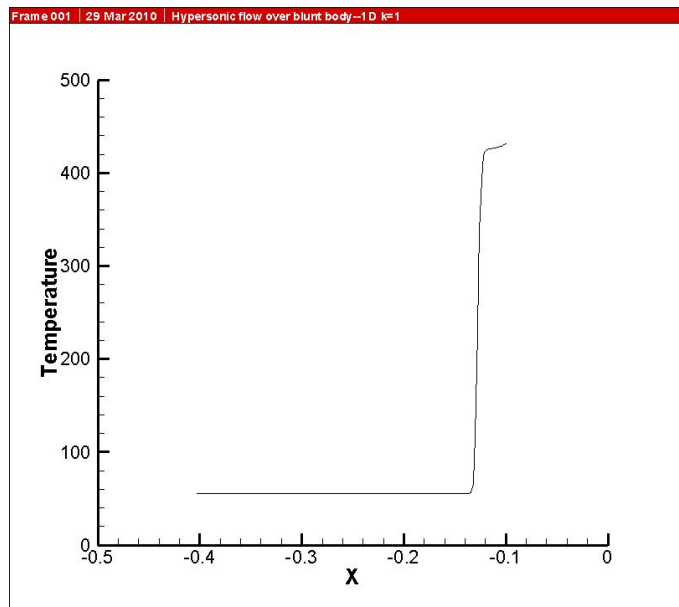


Figure 5.12: Temperature Profile along the Stagnation Line for Supersonic Flow Past an Axisymmetric Blunt Body; $M = 5.85$, $\alpha = 0^\circ$.

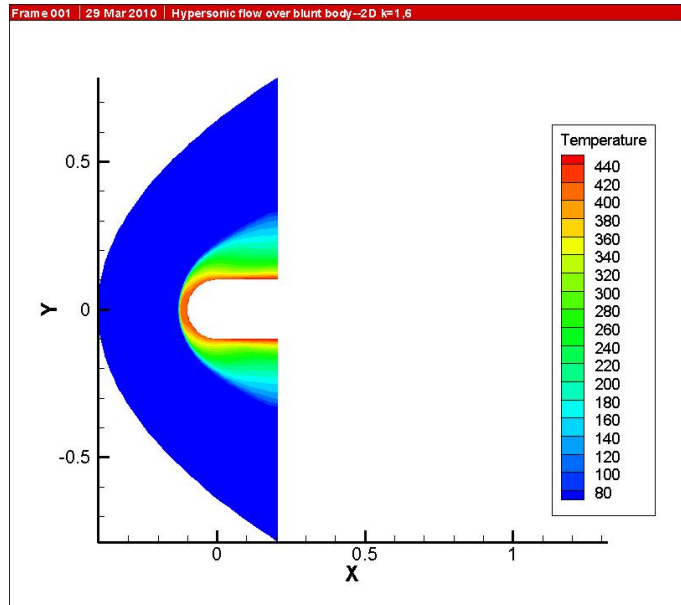


Figure 5.13: Temperature Contours in the $x - y$ Plane for Supersonic Flow Past an Ax-symmetric Blunt Body; $M = 5.85$, $\alpha = 0^\circ$.

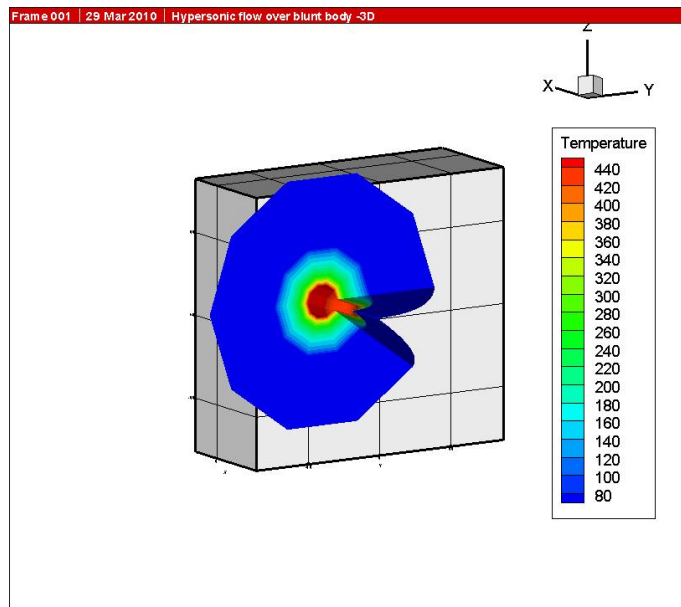


Figure 5.14: 3-D View of the Temperature Contours for Supersonic Flow Past an Ax-symmetric Blunt Body; $M = 5.85$, $\alpha = 0^\circ$.

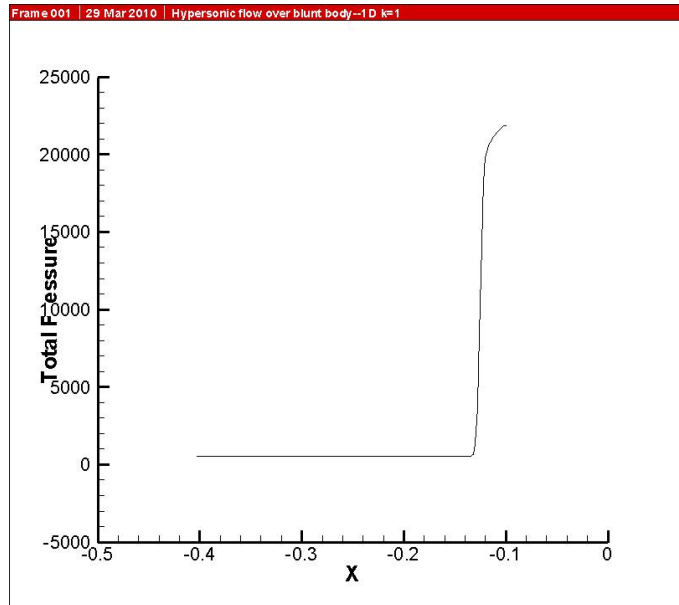


Figure 5.15: Total Pressure Profile along the Stagnation Line for Supersonic Flow Past an Axisymmetric Blunt Body; $M = 5.85$, $\alpha = 0^\circ$.

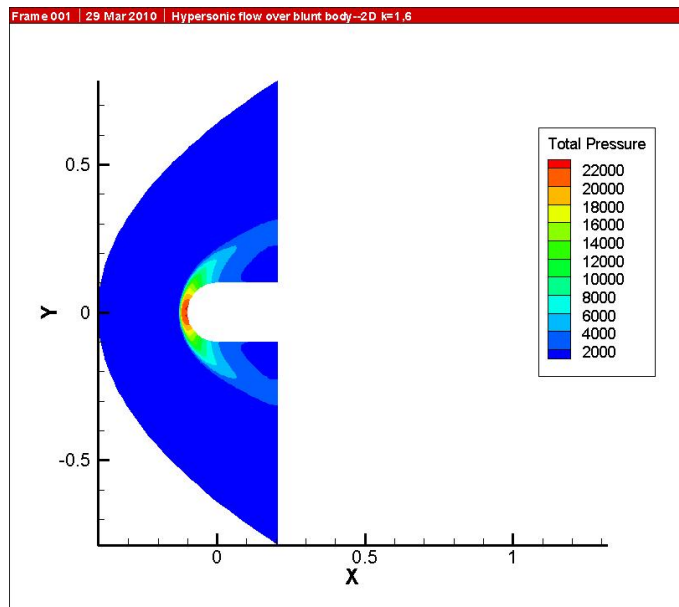


Figure 5.16: Total Pressure Contours in the $x - y$ Plane for Supersonic Flow Past an Axisymmetric Blunt Body; $M = 5.85$, $\alpha = 0^\circ$.

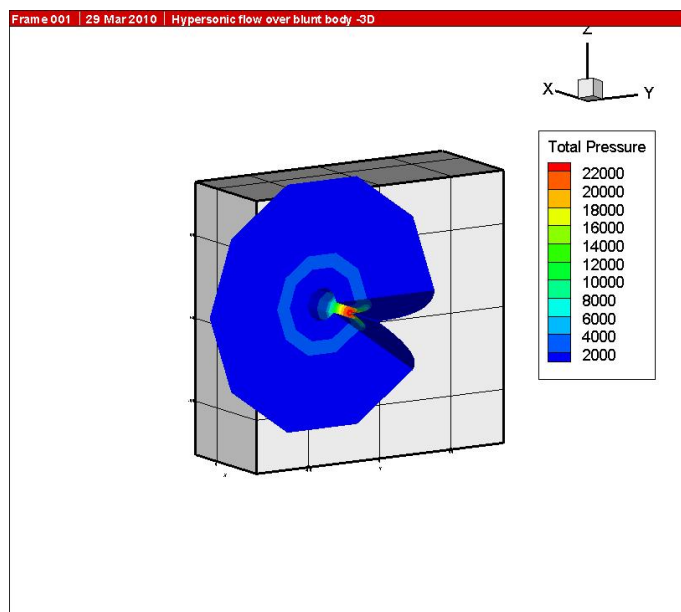


Figure 5.17: 3-D View of the Total Pressure Contours for Supersonic Flow Past an Axisymmetric Blunt Body; $M = 5.85$, $\alpha = 0^\circ$.

5.2.2 Flowfield Computations at $M = 5.85, \alpha = 3^\circ$

In this case, relatively coarse grid of $40 \times 51 \times 10$ mesh points was found to be sufficient for accurate results. Figure (5.18) shows the variation of density along the stagnation line. Figure (5.19) shows the density contours in the $x - y$ plane and Figure (5.20) shows a 3-D view of the density contours. Figure (5.21) shows the variation in the streamwise velocity along the stagnation line. Figure (5.22) shows the contours of the streamwise velocity in $x - y$ plane and figure (5.23) shows the 3-D view of the streamwise velocity. Figure (5.24) shows the variation in temperature along the stagnation line. Figure (5.25) shows the temperature contours in the $x - y$ plane and Figure (5.26) shows a 3-D view of the temperature contours. Figure (5.27) shows the variation in total pressure along the stagnation line. Figure (5.28) shows the total pressure contours in the $x - y$ plane and Figure (5.29) shows a 3-D view of the total pressure contours. The magnitudes of the different flow variables at the stagnation point are as expected from analytical normal shock theory.

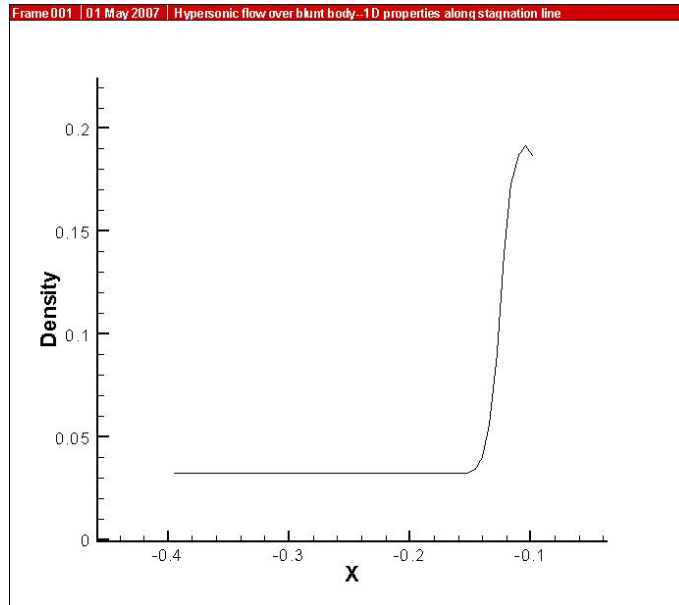


Figure 5.18: Density Profile along the Stagnation Line for Supersonic Flow Past an Axisymmetric Blunt Body; $M = 5.85$, $\alpha = 3^\circ$.

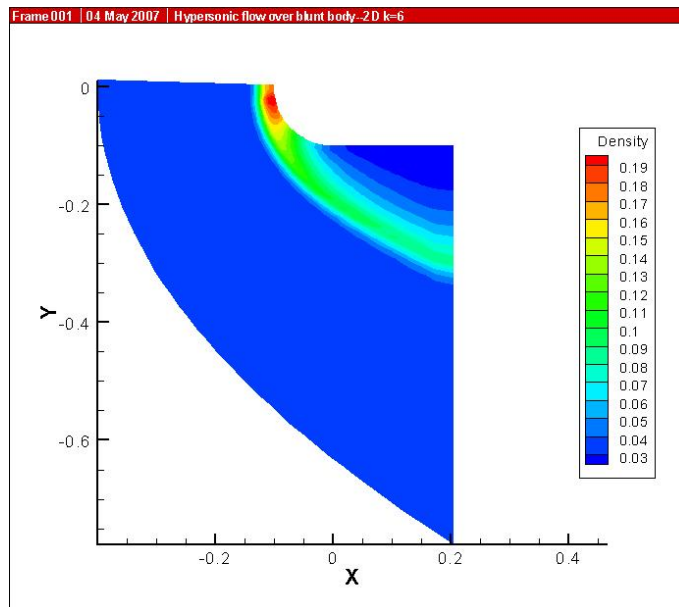


Figure 5.19: Density Contours in the $x - y$ Plane for Supersonic Flow Past an Axisymmetric Blunt Body; $M = 5.85$, $\alpha = 3^\circ$.

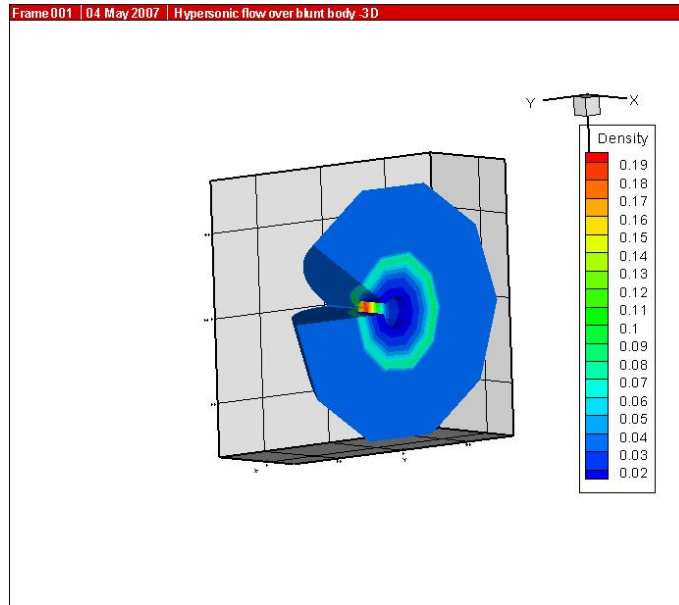


Figure 5.20: 3-D View of the Density Contours for Supersonic Flow Past an Axisymmetric Blunt Body; $M = 5.85$, $\alpha = 3^\circ$.

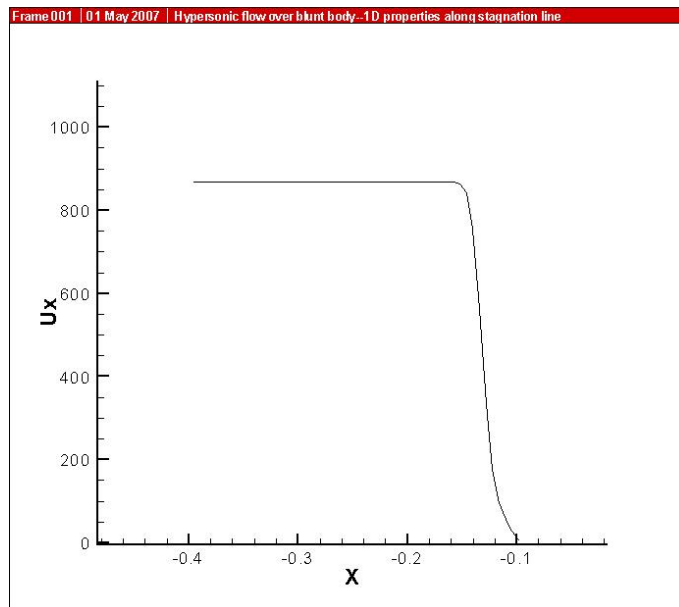


Figure 5.21: Streamwise Velocity Profile along the Stagnation Line for Supersonic Flow Past an Axisymmetric Blunt Body; $M = 5.85$, $\alpha = 3^\circ$.

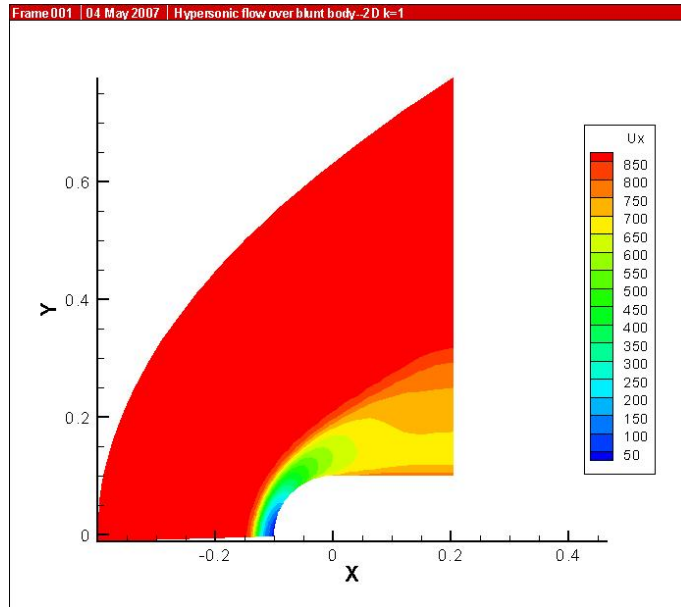


Figure 5.22: Velocity Contours in the $x - y$ Plane for Supersonic Flow Past an Axisymmetric Blunt Body; $M = 5.85$, $\alpha = 3^\circ$.

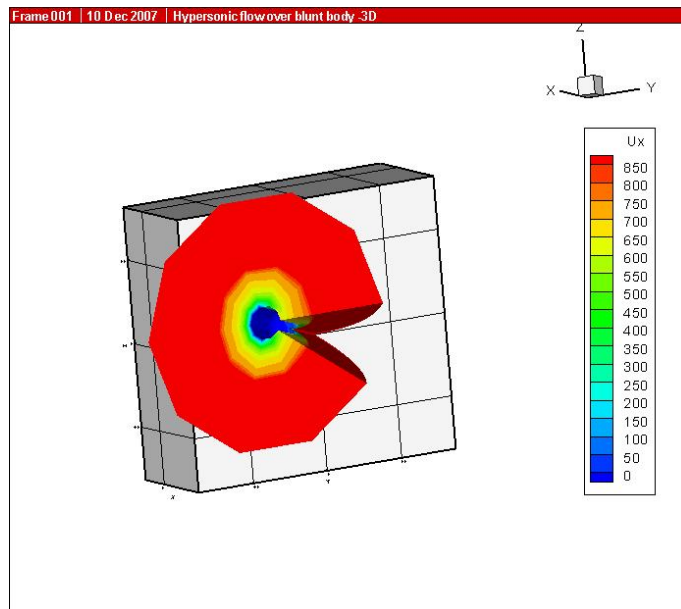


Figure 5.23: 3-D View of the Velocity Contours for Supersonic Flow Past an Axisymmetric Blunt Body; $M = 5.85$, $\alpha = 3^\circ$.

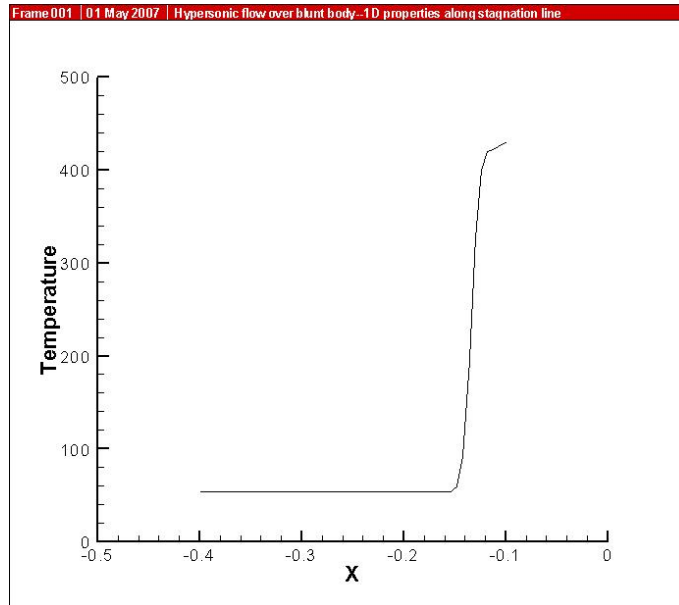


Figure 5.24: Temperature Profile along the Stagnation Line for Supersonic Flow Past an Axisymmetric Blunt Body; $M = 5.85$, $\alpha = 3^\circ$.

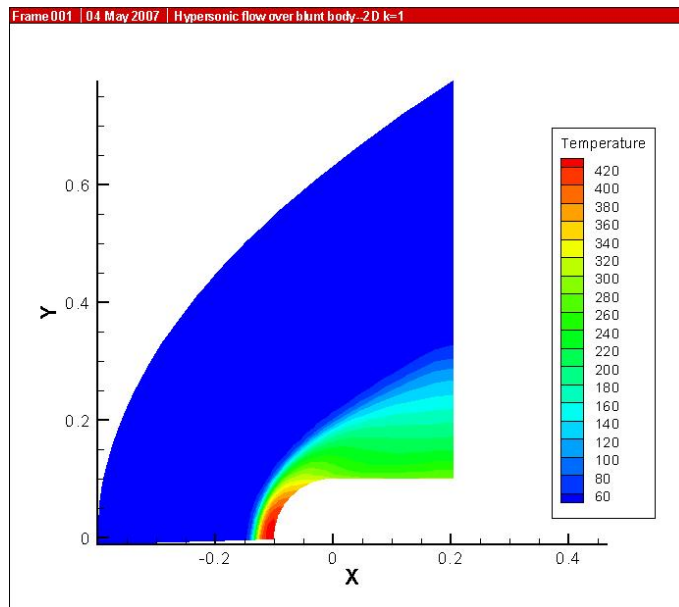


Figure 5.25: Temperature Contours in the $x - y$ Plane for Supersonic Flow Past an Axisymmetric Blunt Body; $M = 5.85$, $\alpha = 3^\circ$.

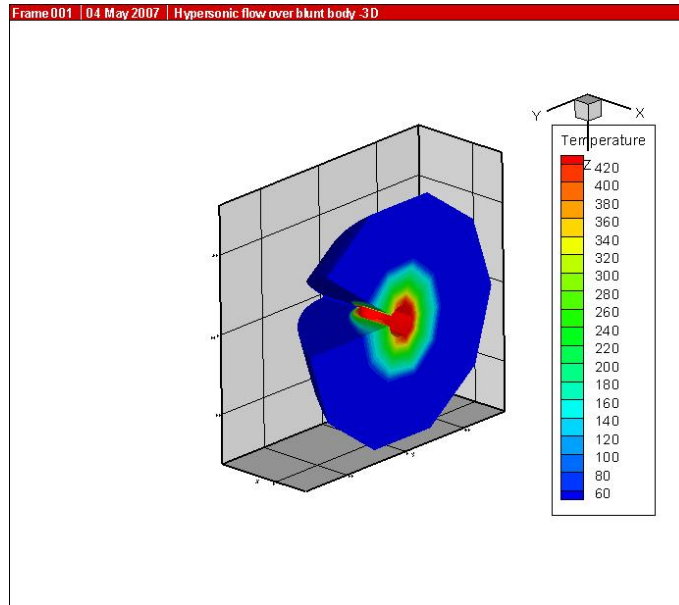


Figure 5.26: 3-D View of the Temperature Contours for Supersonic Flow Past an Axisymmetric Blunt Body; $M = 5.85$, $\alpha = 3^\circ$.

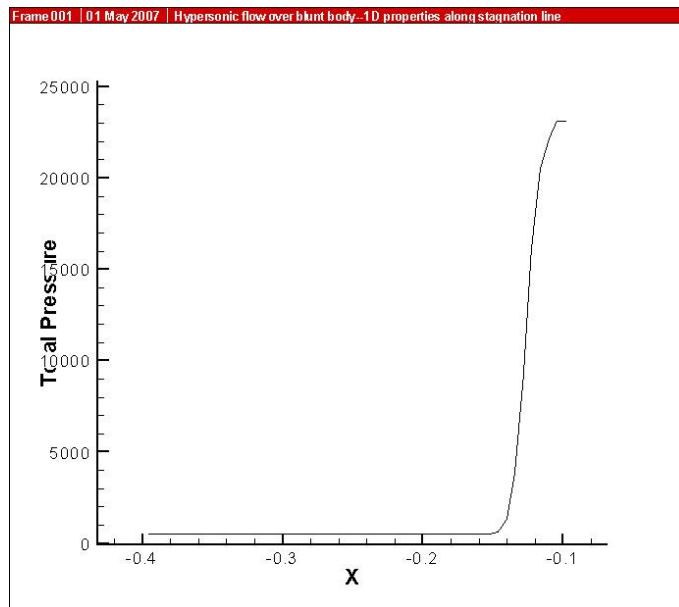


Figure 5.27: Total Pressure Profile along the Stagnation Line for Supersonic Flow Past an Axisymmetric Blunt Body; $M = 5.85$, $\alpha = 3^\circ$.

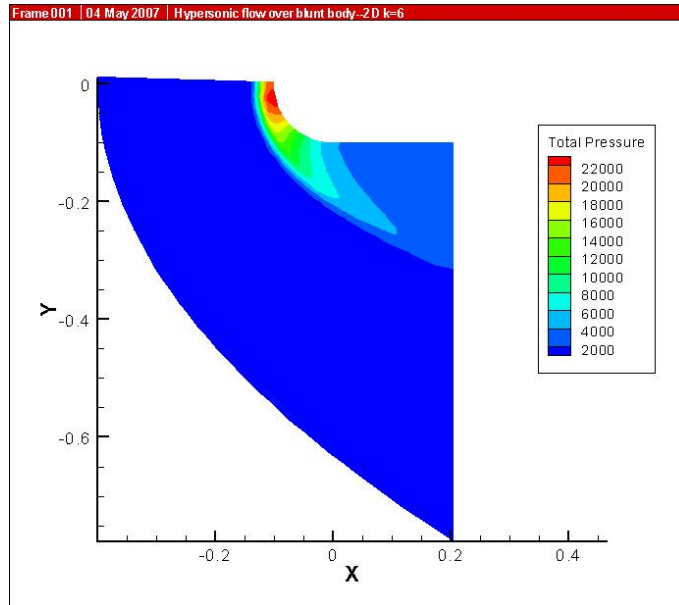


Figure 5.28: Total Pressure Contours in the $x - y$ Plane for Supersonic Flow Past an Axisymmetric Blunt Body; $M = 5.85$, $\alpha = 3^\circ$.

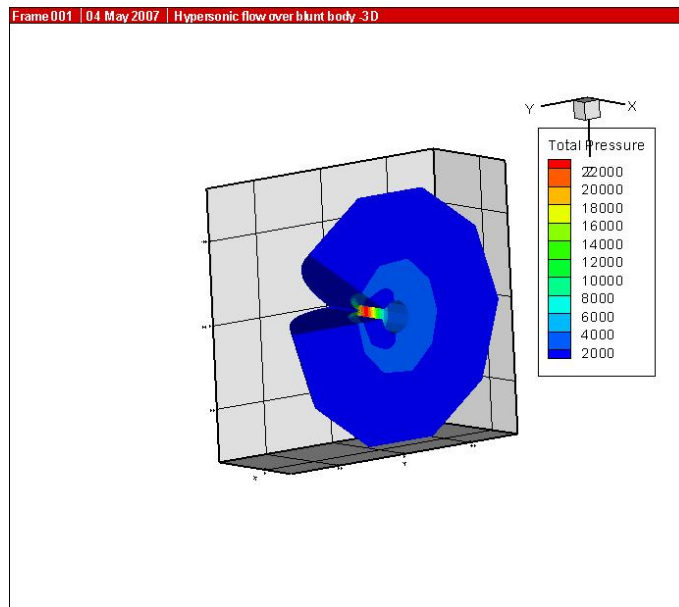


Figure 5.29: 3-D View of the Total Pressure Contours for Supersonic Flow Past an Axisymmetric Blunt Body; $M = 5.85$, $\alpha = 3^\circ$.

5.2.3 Flowfield Computations at $M = 5.85, \alpha = 6^\circ$

In this case, a finer grid of $117 \times 51 \times 10$ mesh points was used to maintain accuracy. Figure (5.30) shows the variation of density along the stagnation line. Figure (5.31) shows the density contours in the $x - y$ plane and Figure (5.32) shows a 3-D view of the density contours. Figure (5.33) shows the variation in the streamwise velocity along the stagnation line. Figure (5.34) shows the contours of the streamwise velocity in $x - y$ plane and figure (5.35) shows the 3-D view of the streamwise velocity. Figure (5.36) shows the variation in temperature along the stagnation line. Figure (5.37) shows the temperature contours in the $x - y$ plane and Figure (5.38) shows a 3-D view of the temperature contours. Figure (5.39) shows the variation in total pressure along the stagnation line. Figure (5.40) shows the total pressure contours in the $x - y$ plane and Figure (5.41) shows a 3-D view of the total pressure contours. The magnitudes of the different flow variables at the stagnation point are as expected from analytical normal shock theory.

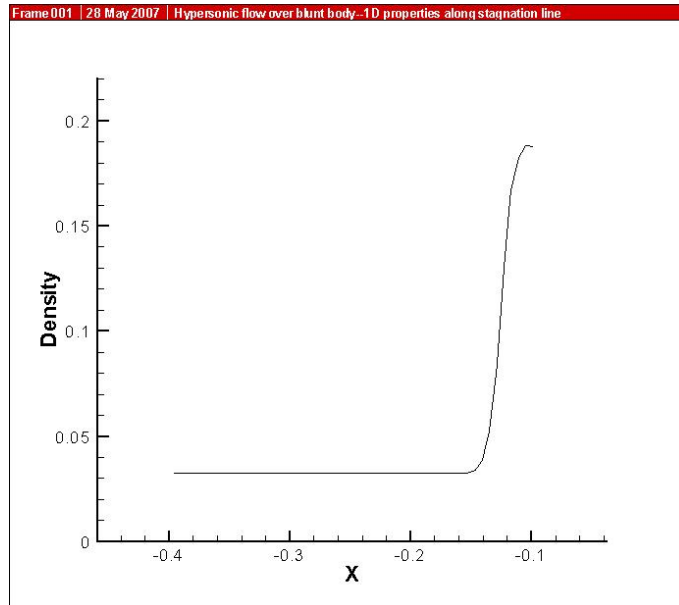


Figure 5.30: Density Profile along the Stagnation Line for Supersonic Flow Past an Axisymmetric Blunt Body; $M = 5.85$, $\alpha = 6^\circ$.

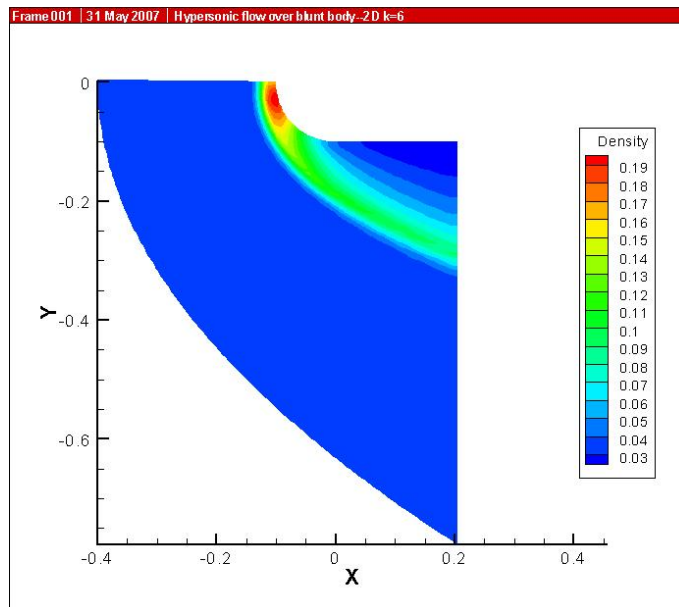


Figure 5.31: Density Contours in the $x - y$ Plane for Supersonic Flow Past an Axisymmetric Blunt Body; $M = 5.85$, $\alpha = 6^\circ$.

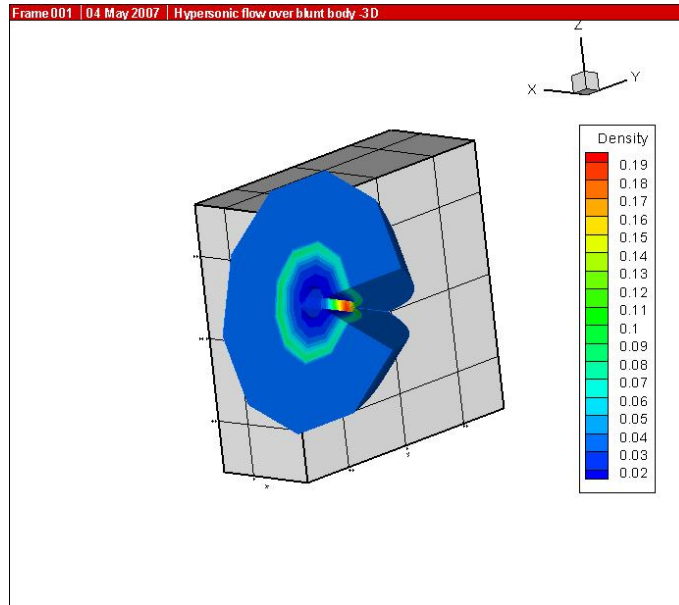


Figure 5.32: 3-D View of the Density Contours for Supersonic Flow Past an Axisymmetric Blunt Body; $M = 5.85$, $\alpha = 6^\circ$.

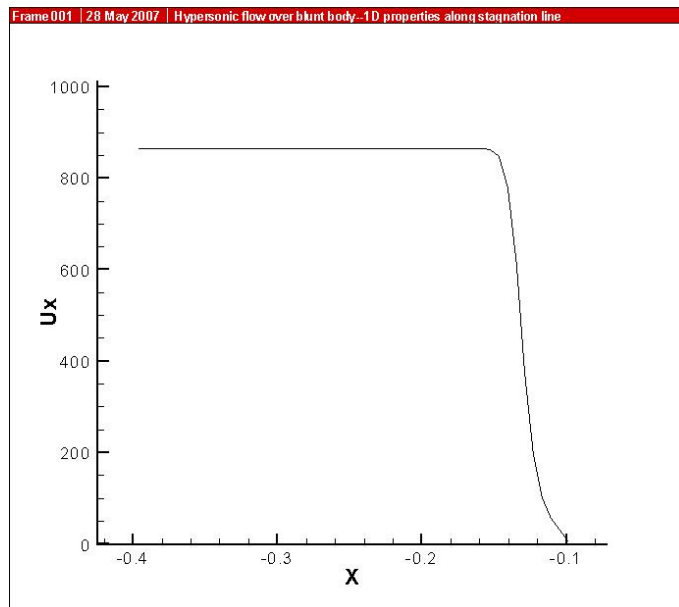


Figure 5.33: Streamwise Velocity Profile along the Stagnation Line for Supersonic Flow Past an Axisymmetric Blunt Body; $M = 5.85$, $\alpha = 6^\circ$.

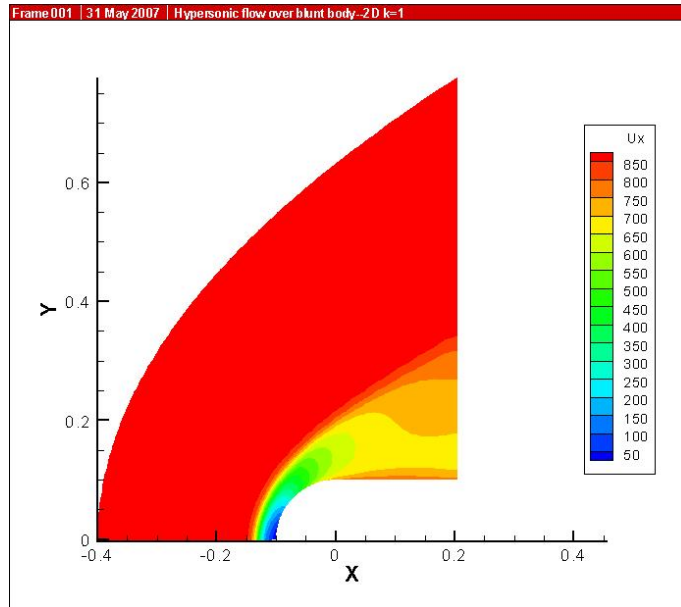


Figure 5.34: Velocity Contours in the $x - y$ Plane for Supersonic Flow Past an Axisymmetric Blunt Body; $M = 5.85$, $\alpha = 6^\circ$.

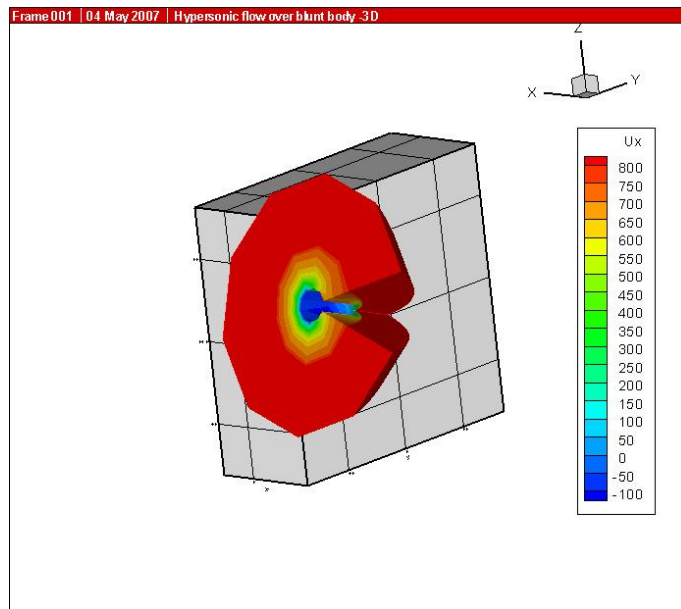


Figure 5.35: 3-D View of the Velocity Contours for Supersonic Flow Past an Axisymmetric Blunt Body; $M = 5.85$, $\alpha = 6^\circ$.

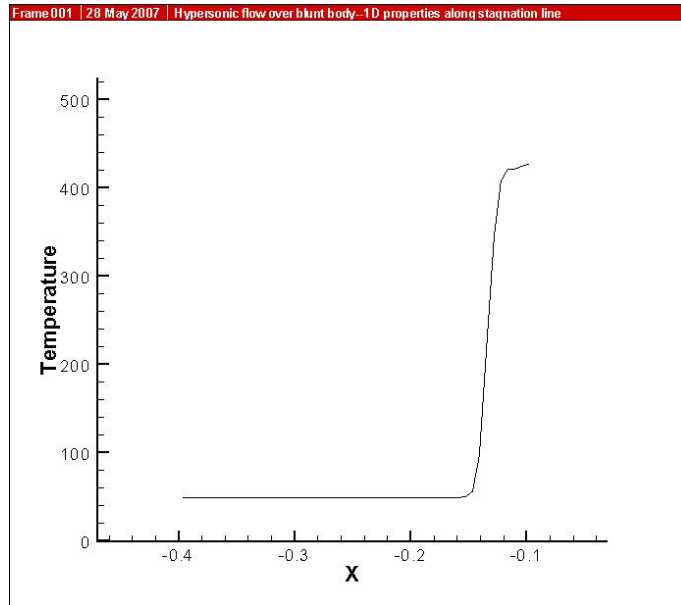


Figure 5.36: Temperature Profile along the Stagnation Line for Supersonic Flow Past an Axisymmetric Blunt Body; $M = 5.85$, $\alpha = 6^\circ$.

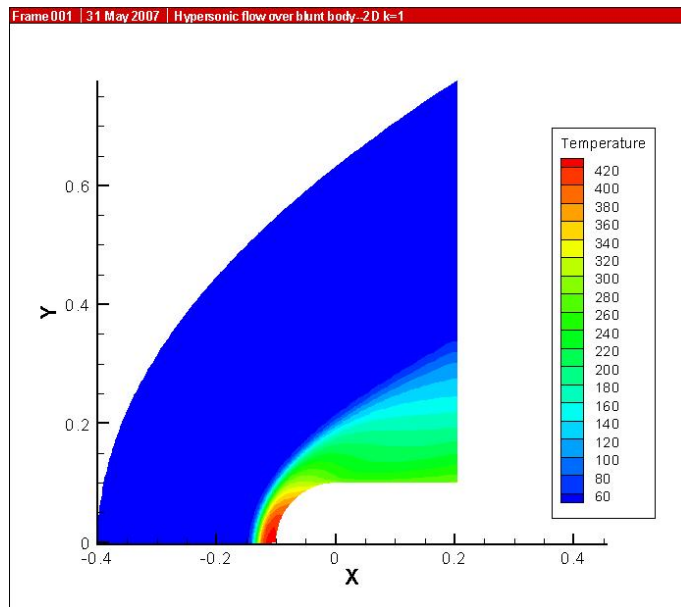


Figure 5.37: Temperature Contours in the $x - y$ Plane for Supersonic Flow Past an Axisymmetric Blunt Body; $M = 5.85$, $\alpha = 6^\circ$.

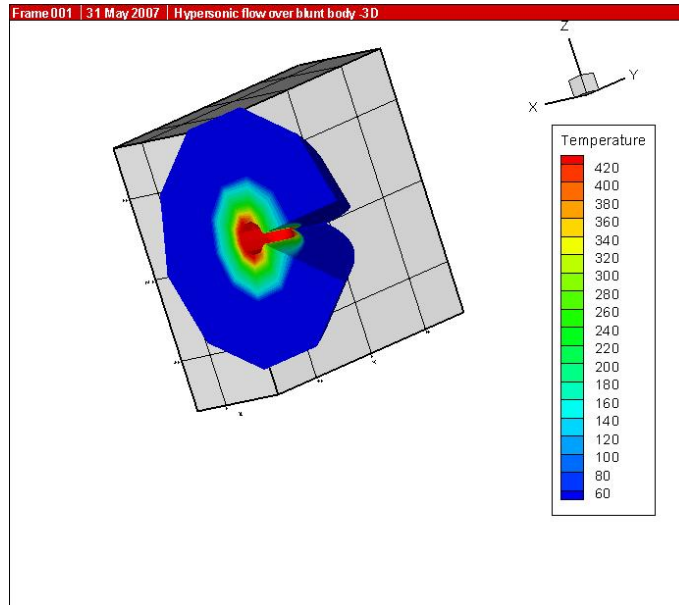


Figure 5.38: 3-D View of the Temperature Contours for Supersonic Flow Past an Axisymmetric Blunt Body; $M = 5.85$, $\alpha = 6^\circ$.

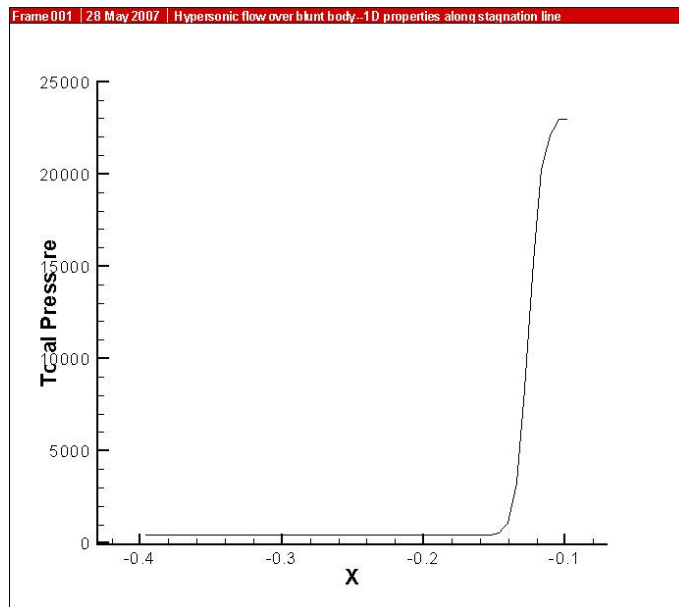


Figure 5.39: Total Pressure Profile along the Stagnation Line for Supersonic Flow Past an Axisymmetric Blunt Body; $M = 5.85$, $\alpha = 6^\circ$.

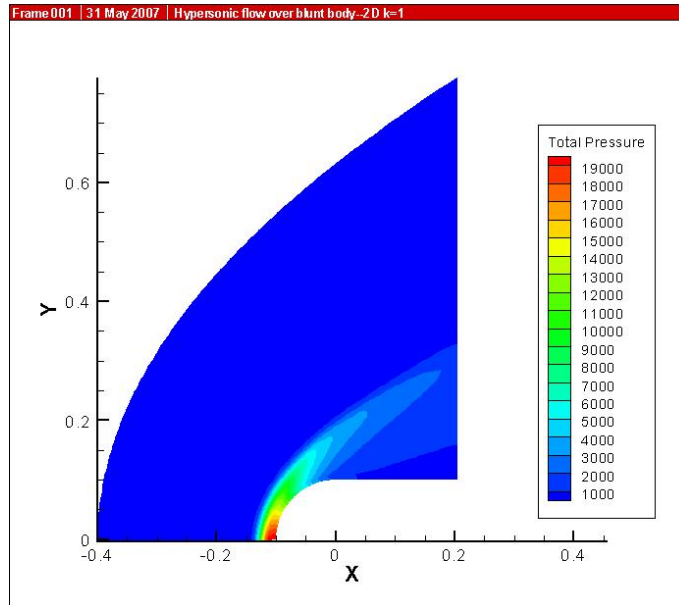


Figure 5.40: Total Pressure Contours in the $x - y$ Plane for Supersonic Flow Past an Axisymmetric Blunt Body; $M = 5.85, \alpha = 6^\circ$.

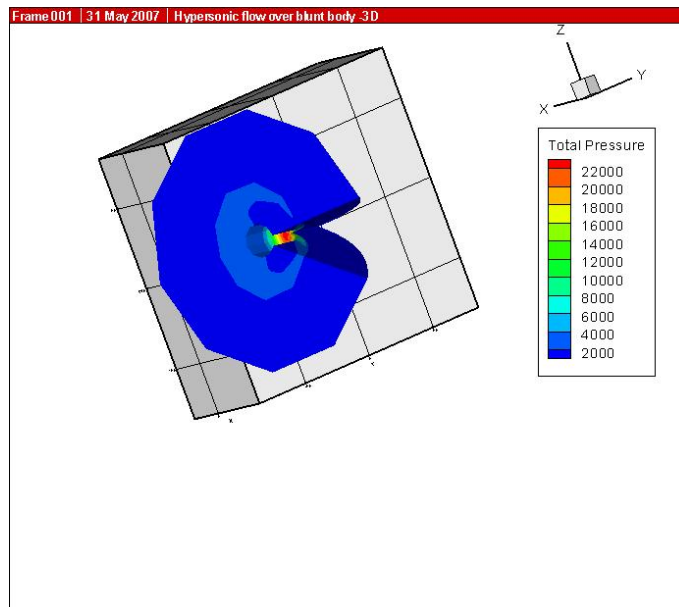


Figure 5.41: 3-D View of the Total Pressure Contours for Supersonic Flow Past an Axisymmetric Blunt Body; $M = 5.85, \alpha = 6^\circ$.

5.2.4 Flowfield Computations at $M = 5.85, \alpha = 10^\circ$

In this case, a finer grid of $117 \times 51 \times 10$ mesh points was used to maintain accuracy. Figure (5.42) shows the variation of density along the stagnation line. Figure (5.43) shows the density contours in the $x - y$ plane and Figure (5.44) shows a 3-D view of the density contours. Figure (5.45) shows the variation in the streamwise velocity along the stagnation line. Figure (5.46) shows the contours of the streamwise velocity in $x - y$ plane and figure (5.47) shows the 3-D view of the streamwise velocity. Figure (5.48) shows the variation in temperature along the stagnation line. Figure (5.49) shows the temperature contours in the $x - y$ plane and Figure (5.50) shows a 3-D view of the temperature contours. Figure (5.51) shows the variation in total pressure along the stagnation line. Figure (5.52) shows the total pressure contours in the $x - y$ plane and Figure (5.53) shows a 3-D view of the total pressure contours. The magnitudes of the different flow variables at the stagnation point are as expected from analytical normal shock theory.

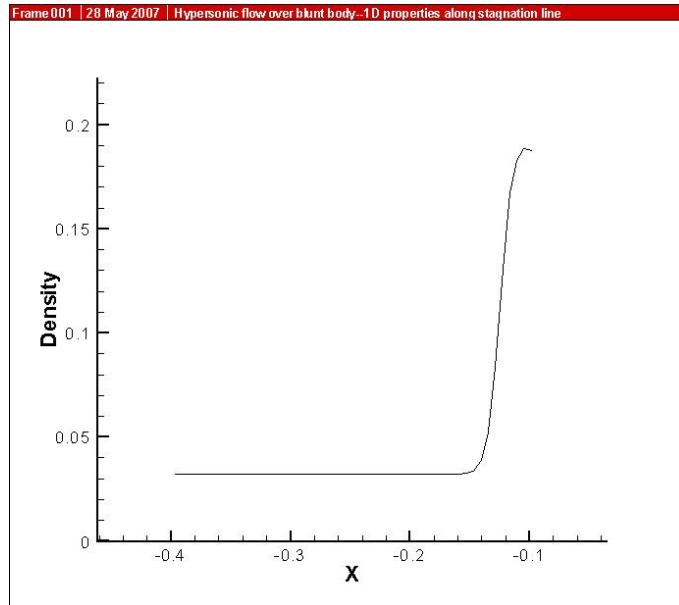


Figure 5.42: Density Profile along the Stagnation Line for Supersonic Flow Past an Axisymmetric Blunt Body; $M = 5.85$, $\alpha = 10^\circ$.

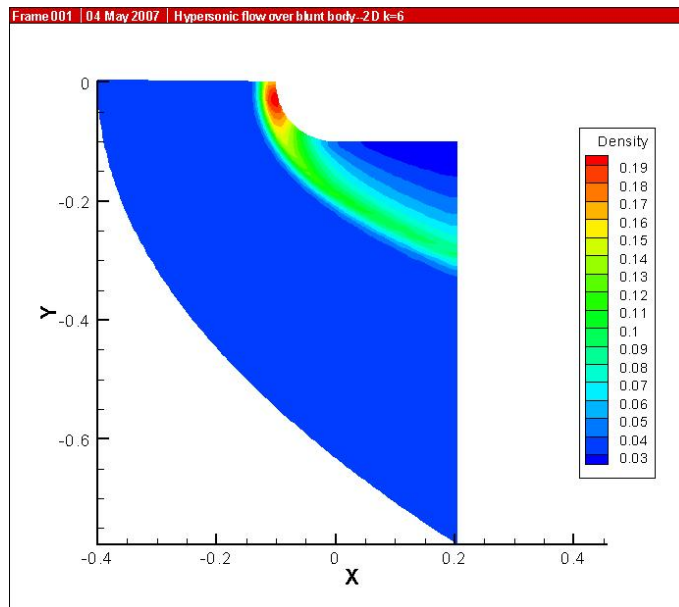


Figure 5.43: Density Contours in the $x - y$ Plane for Supersonic Flow Past an Axisymmetric Blunt Body; $M = 5.85$, $\alpha = 10^\circ$.

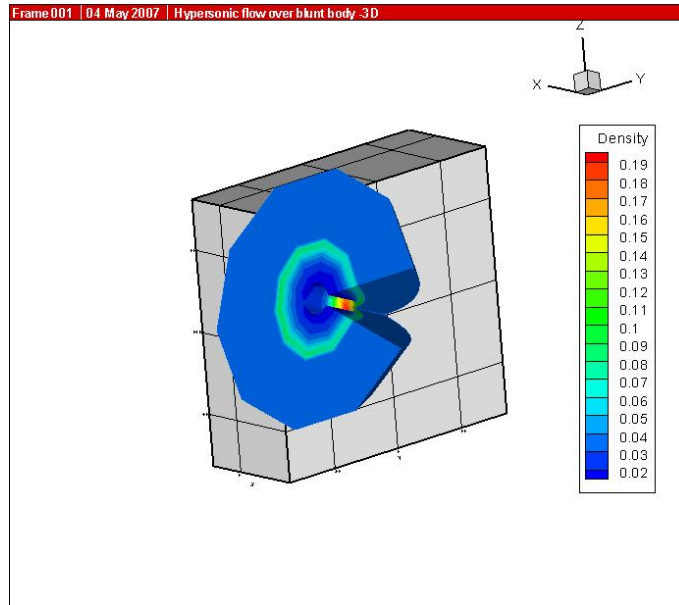


Figure 5.44: 3-D View of the Density Contours for Supersonic Flow Past an Axisymmetric Blunt Body; $M = 5.85$, $\alpha = 10^\circ$.

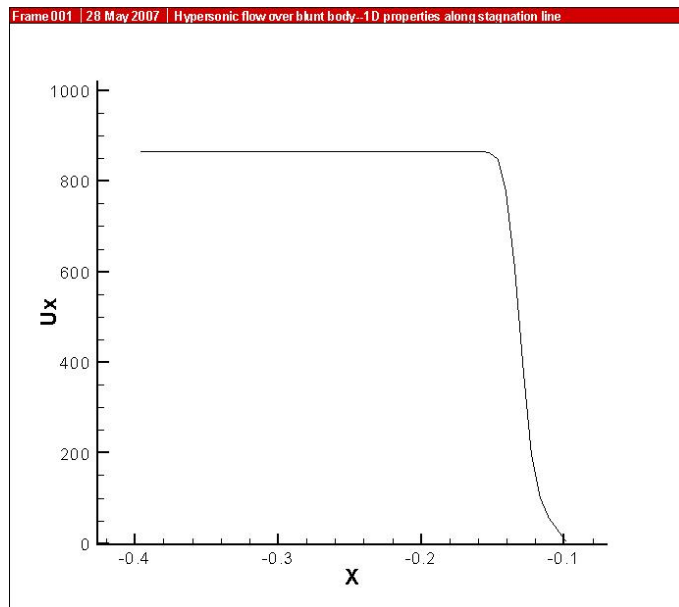


Figure 5.45: Streamwise Velocity Profile along the Stagnation Line for Supersonic Flow Past an Axisymmetric Blunt Body; $M = 5.85$, $\alpha = 10^\circ$.

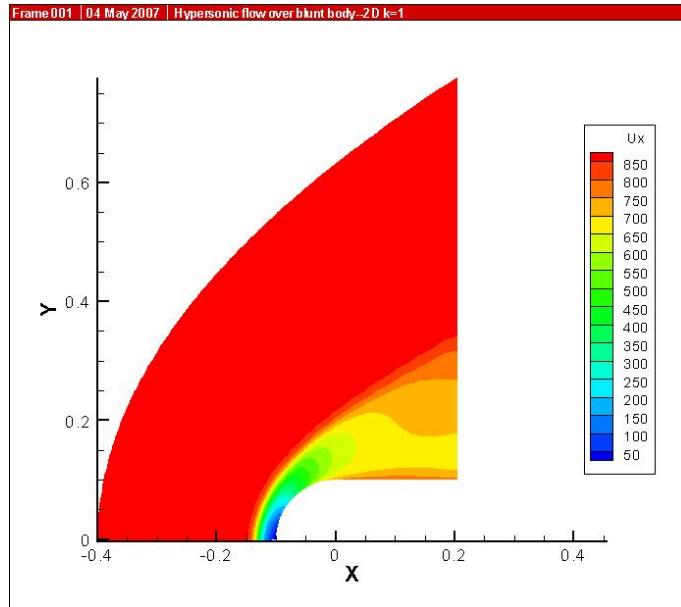


Figure 5.46: Velocity Contours in the $x - y$ Plane for Supersonic Flow Past an Axisymmetric Blunt Body; $M = 5.85$, $\alpha = 10^\circ$.

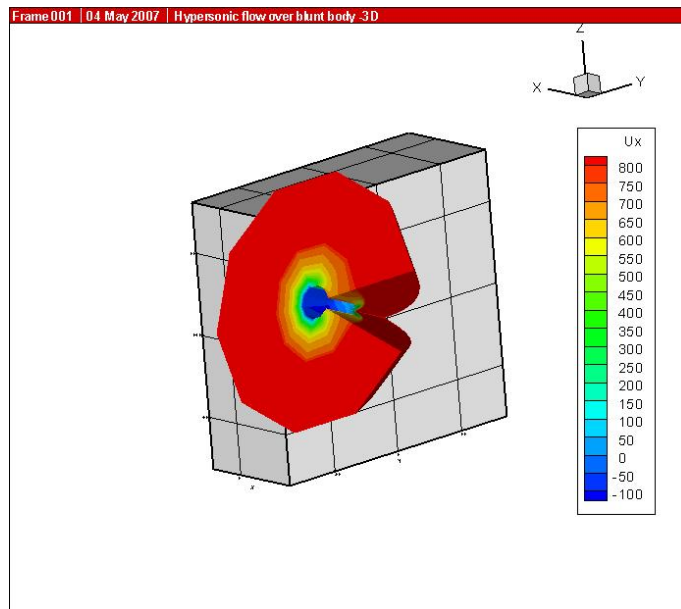


Figure 5.47: 3-D View of the Velocity Contours for Supersonic Flow Past an Axisymmetric Blunt Body; $M = 5.85$, $\alpha = 10^\circ$.

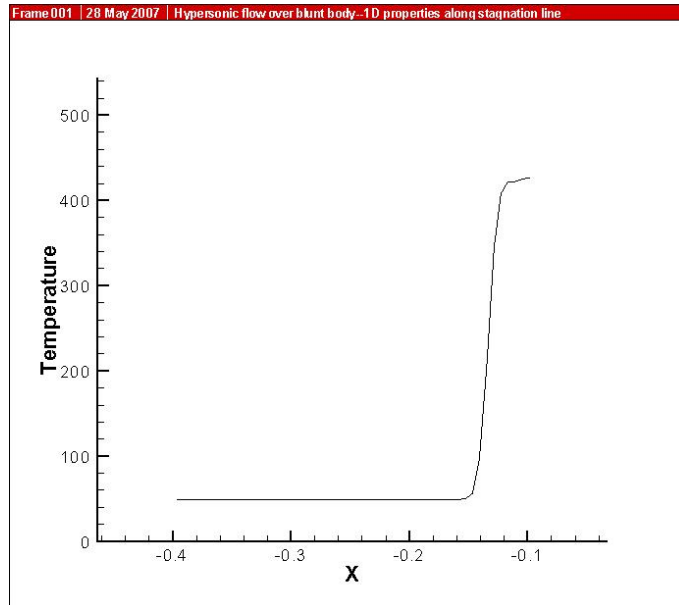


Figure 5.48: Temperature Profile along the Stagnation Line for Supersonic Flow Past an Axisymmetric Blunt Body; $M = 5.85$, $\alpha = 10^\circ$.

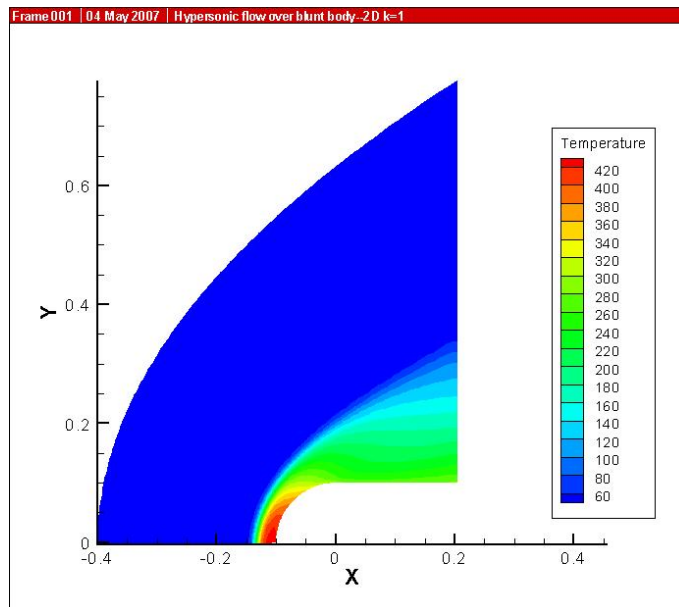


Figure 5.49: Temperature Contours in the $x - y$ Plane for Supersonic Flow Past an Axisymmetric Blunt Body; $M = 5.85$, $\alpha = 10^\circ$.

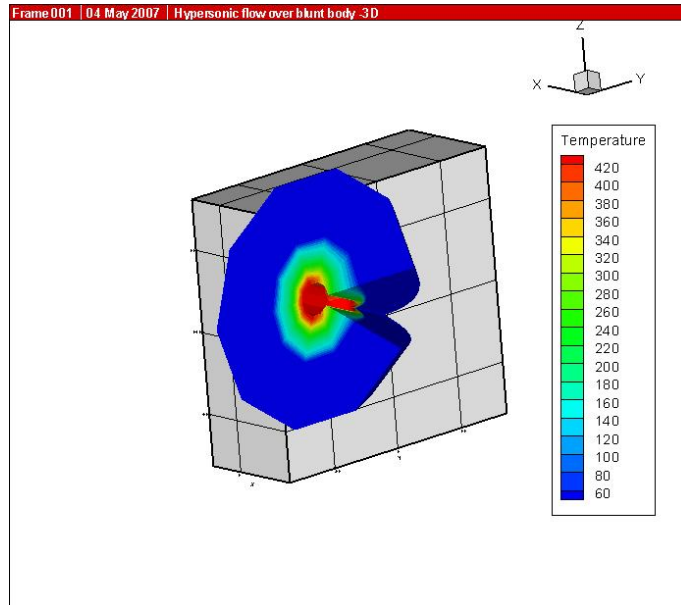


Figure 5.50: 3-D View of the Temperature Contours for Supersonic Flow Past an Axisymmetric Blunt Body; $M = 5.85$, $\alpha = 10^\circ$.

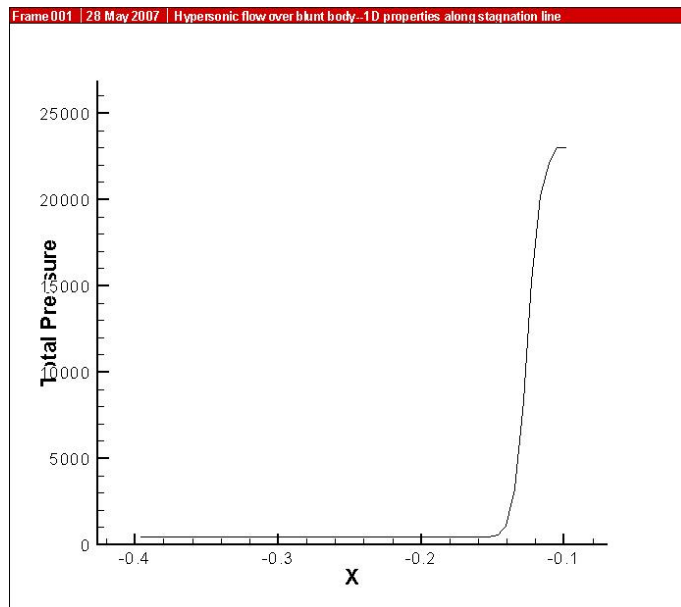


Figure 5.51: Total Pressure Profile along the Stagnation Line for Supersonic Flow Past an Axisymmetric Blunt Body; $M = 5.85$, $\alpha = 10^\circ$.

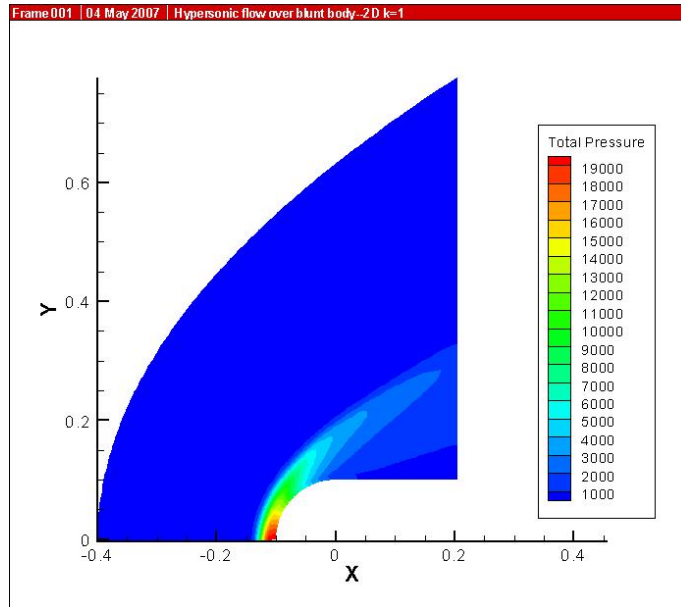


Figure 5.52: Total Pressure Contours in the $x - y$ Plane for Supersonic Flow Past an Axisymmetric Blunt Body; $M = 5.85, \alpha = 10^\circ$.

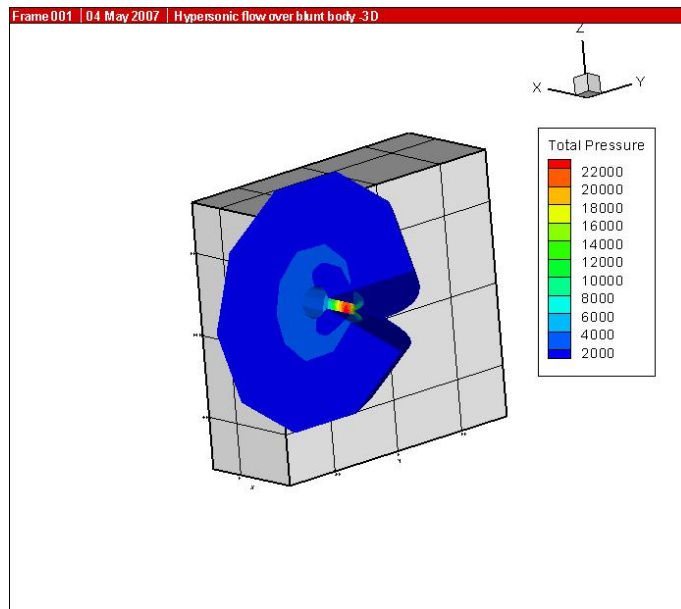


Figure 5.53: 3-D View of the Total Pressure Contours for Supersonic Flow Past an Axisymmetric Blunt Body; $M = 5.85, \alpha = 10^\circ$.

5.2.5 Flowfield Computations at $M = 5.85, \alpha = 15^\circ$

In this case, a finer grid of $117 \times 51 \times 10$ mesh points was used to maintain accuracy. Figure (5.54) shows the variation of density along the stagnation line. Figure (5.55) shows the density contours in the $x - y$ plane and Figure (5.56) shows a 3-D view of the density contours. Figure (5.57) shows the variation in the streamwise velocity along the stagnation line. Figure (5.58) shows the contours of the streamwise velocity in $x - y$ plane and figure (5.59) shows the 3-D view of the streamwise velocity. Figure (5.60) shows the variation in temperature along the stagnation line. Figure (5.61) shows the temperature contours in the $x - y$ plane and Figure (5.62) shows a 3-D view of the temperature contours. Figure (5.63) shows the variation in total pressure along the stagnation line. Figure (5.64) shows the total pressure contours in the $x - y$ plane and Figure (5.65) shows a 3-D view of the total pressure contours. The magnitudes of the different flow variables at the stagnation point are as expected from analytical normal shock theory.

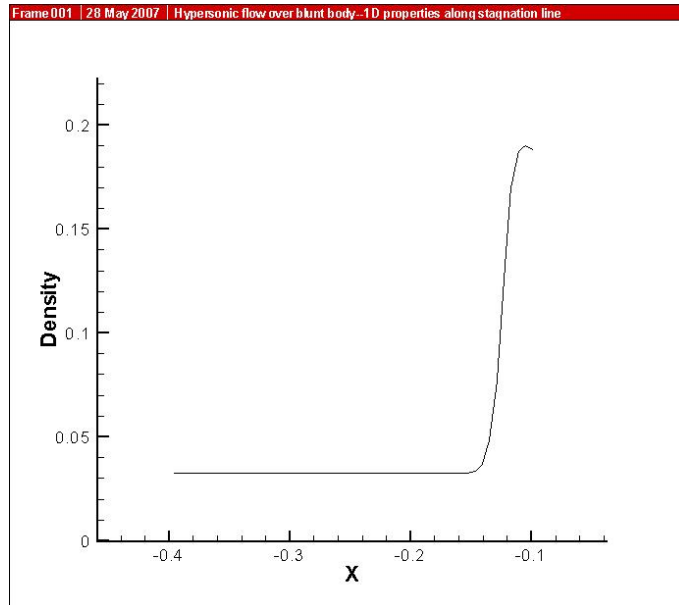


Figure 5.54: Density Profile along the Stagnation Line for Supersonic Flow Past an Axisymmetric Blunt Body; $M = 5.85$, $\alpha = 15^\circ$.

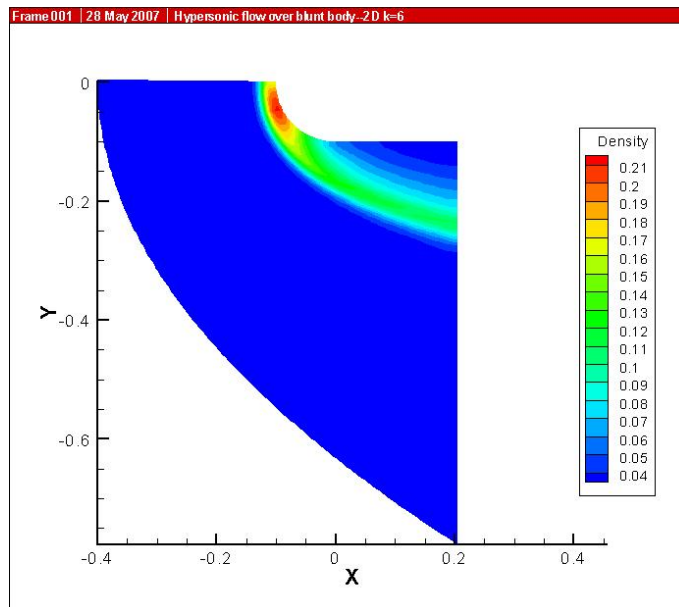


Figure 5.55: Density Contours in the $x - y$ Plane for Supersonic Flow Past an Axisymmetric Blunt Body; $M = 5.85$, $\alpha = 15^\circ$.

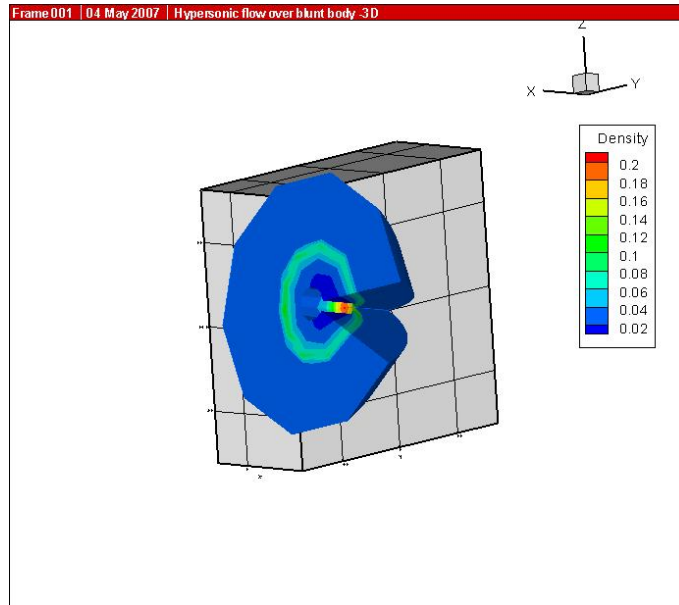


Figure 5.56: 3-D View of the Density Contours for Supersonic Flow Past an Axisymmetric Blunt Body; $M = 5.85$, $\alpha = 15^\circ$.

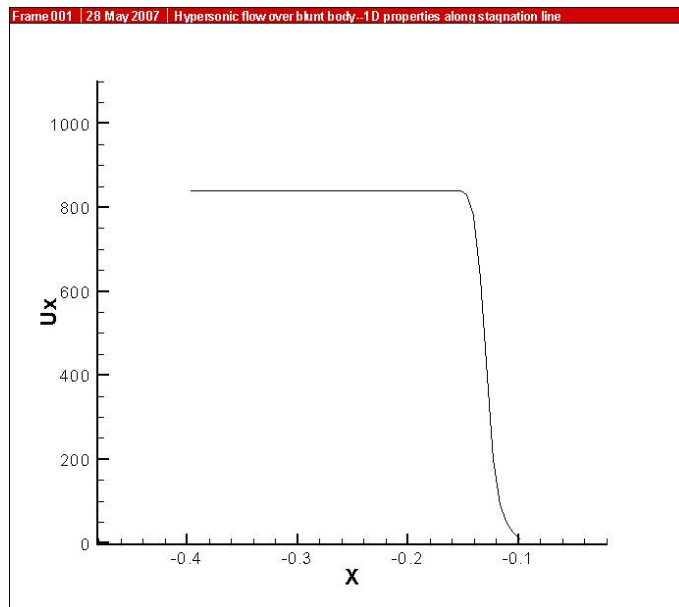


Figure 5.57: Streamwise Velocity Profile along the Stagnation Line for Supersonic Flow Past an Axisymmetric Blunt Body; $M = 5.85$, $\alpha = 15^\circ$.

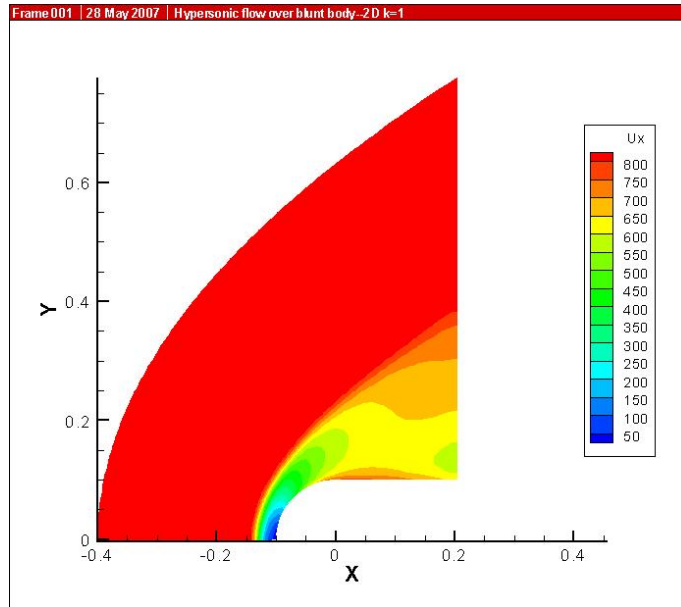


Figure 5.58: Velocity Contours in the $x - y$ Plane for Supersonic Flow Past an Axisymmetric Blunt Body; $M = 5.85$, $\alpha = 15^\circ$.

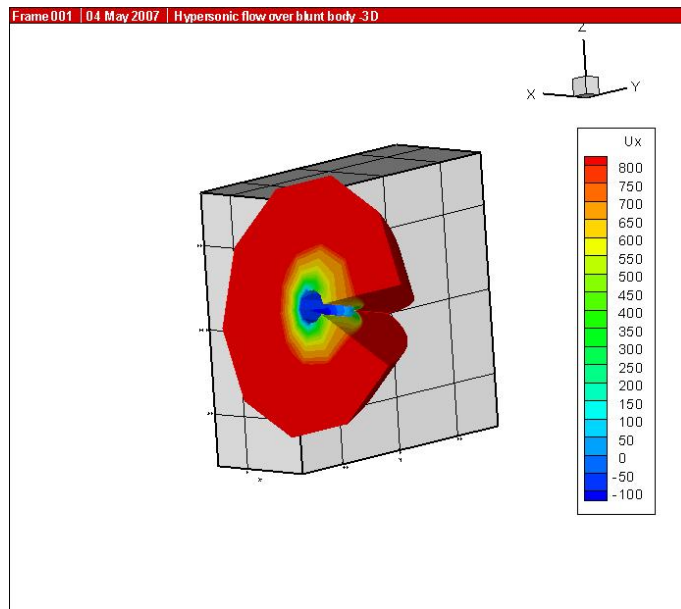


Figure 5.59: 3-D View of the Velocity Contours for Supersonic Flow Past an Axisymmetric Blunt Body; $M = 5.85$, $\alpha = 15^\circ$.

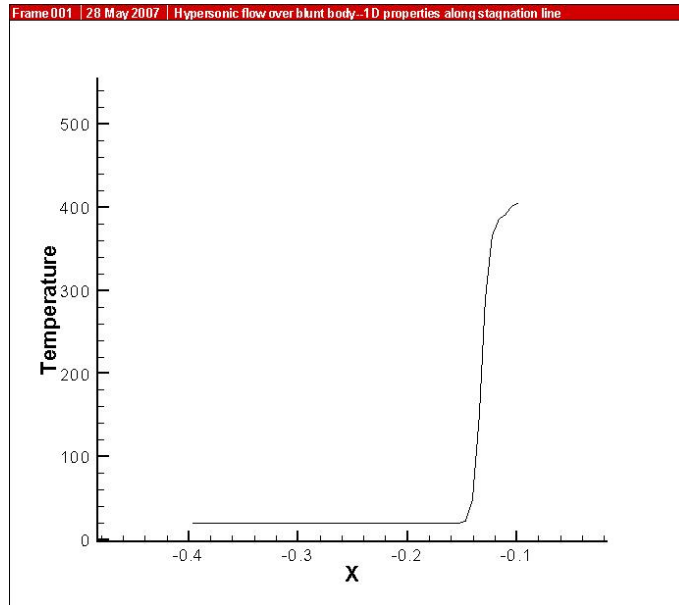


Figure 5.60: Temperature Profile along the Stagnation Line for Supersonic Flow Past an Axisymmetric Blunt Body; $M = 5.85$, $\alpha = 15^\circ$.

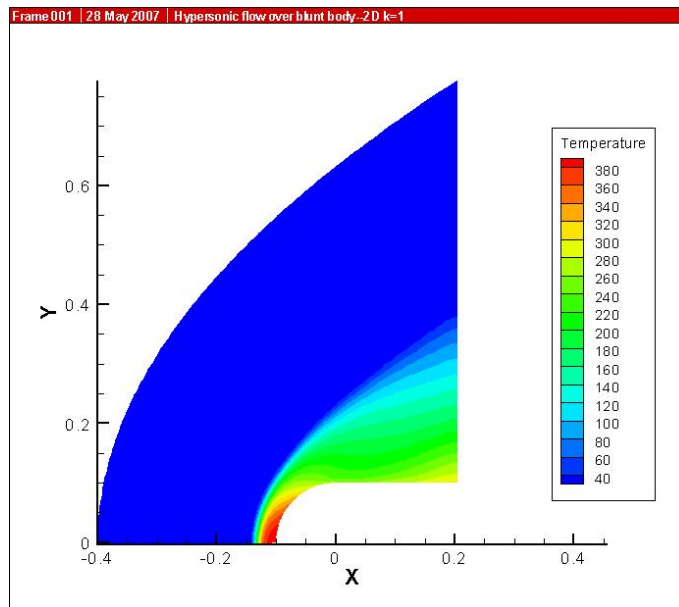


Figure 5.61: Temperature Contours in the $x - y$ Plane for Supersonic Flow Past an Axisymmetric Blunt Body; $M = 5.85$, $\alpha = 15^\circ$.

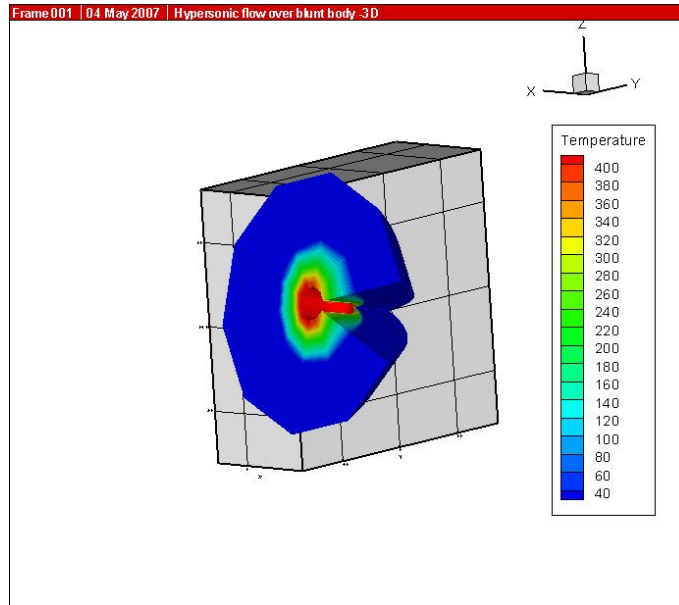


Figure 5.62: 3-D View of the Temperature Contours for Supersonic Flow Past an Axisymmetric Blunt Body; $M = 5.85$, $\alpha = 15^\circ$.

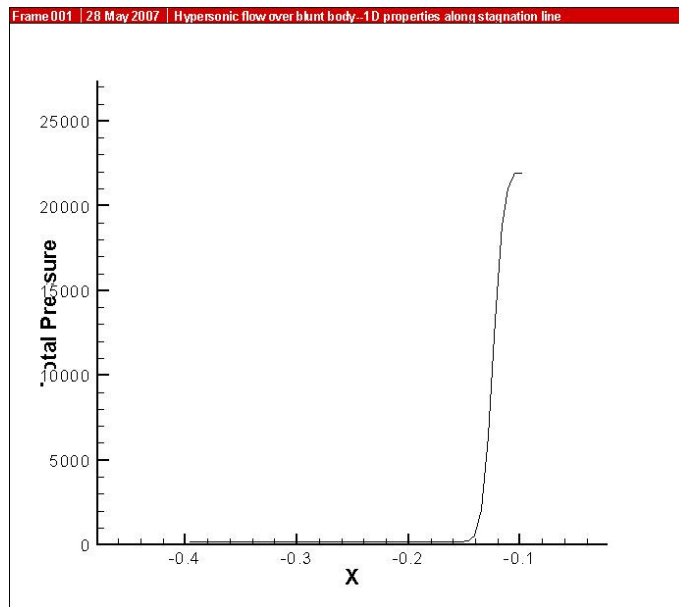


Figure 5.63: Total Pressure Profile along the Stagnation Line for Supersonic Flow Past an Axisymmetric Blunt Body; $M = 5.85$, $\alpha = 15^\circ$.

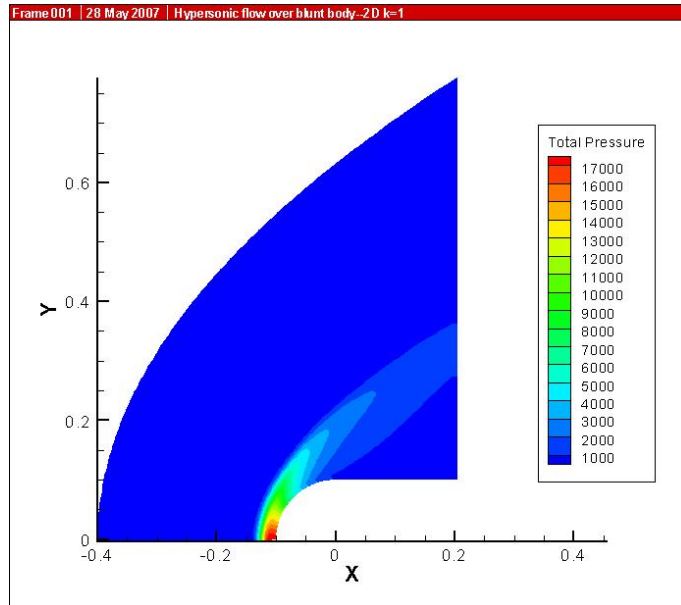


Figure 5.64: Total Pressure Contours in the $x - y$ Plane for Supersonic Flow Past an Axisymmetric Blunt Body; $M = 5.85$, $\alpha = 15^\circ$.

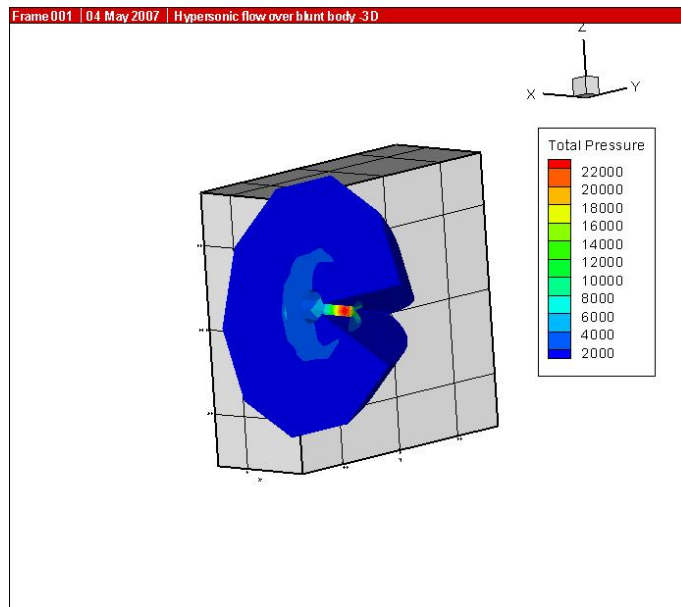


Figure 5.65: 3-D View of the Total Pressure Contours for Supersonic Flow Past an Axisymmetric Blunt Body; $M = 5.85$, $\alpha = 15^\circ$.

Chapter 6

Computation of Inviscid Supersonic MHD Flow Past an Axisymmetric Blunt Body Using the 3-D Ideal MHD solver

In this chapter, computations are performed for supersonic flow past an axisymmetric blunt body in the presence of a magnetic field using the explicit KWPS Ideal MHD flow solver.

6.1 MHD Flowfield Computations at $M = 5.85$, $\alpha = 0^\circ$,

$$B_x = B_y = 0, B_z = 0.04 \text{ T}$$

In this case, the grid of $40 \times 51 \times 10$ mesh points was employed to compute the results. Figure (6.1) shows the variation of density along the stagnation line. Figure (6.2) shows the variation in the streamwise velocity along the stagnation line. Figure (6.3) shows the variation in temperature along the stagnation line. Figure (6.4) shows the variation in thermal pressure along the stagnation line. Figure (6.5) shows the density contours in the $x - y$ plane. Figure (6.6) shows the contours of the streamwise velocity in $x - y$ plane. Figure (6.7) shows the dynamic pressure contours in the $x - y$ plane. These calculations are compared with the Euler calculations in the absence of magnetic field. As shown in section (6.3), the application of the magnetic field decreases the strength of the shock significantly. This effect can be utilized in reducing the shock-wave drag of space vehicles.

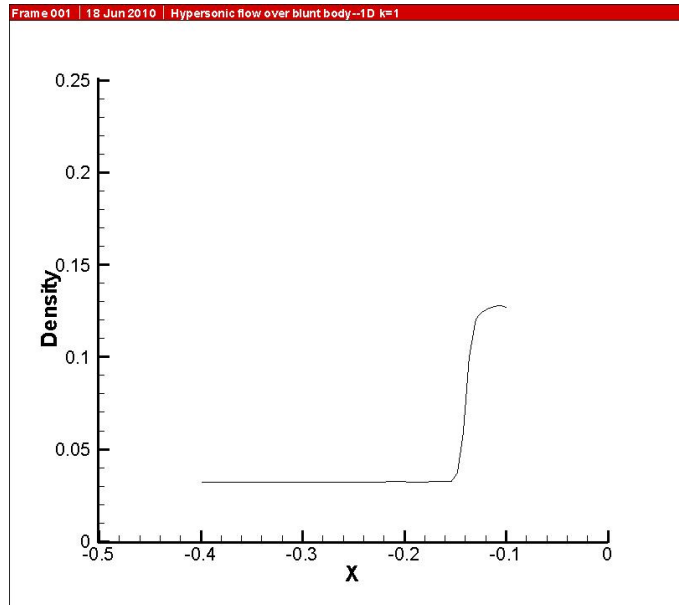


Figure 6.1: Density Profile along the Stagnation Line for Supersonic Flow Past an Axisymmetric Blunt Body; $M = 5.85$, $\alpha = 0^\circ$, $B_x = B_y = 0$, $B_z = 0.04 T$

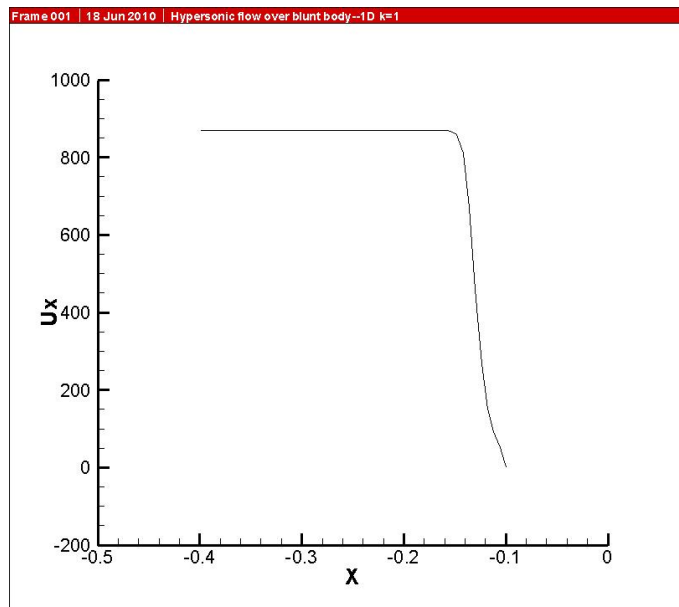


Figure 6.2: Streamwise Velocity Profile along the Stagnation Line for Supersonic Flow Past an Axisymmetric Blunt Body; $M = 5.85$, $\alpha = 0^\circ$, $B_x = B_y = 0$, $B_z = 0.04 T$

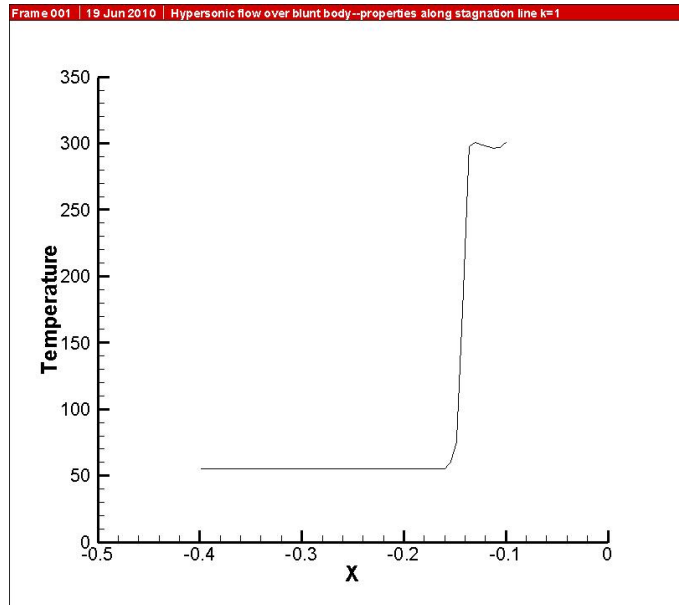


Figure 6.3: Temperature Profile along the Stagnation Line for Supersonic Flow Past an Axisymmetric Blunt Body; $M = 5.85$, $\alpha = 0^\circ$, $B_x = B_y = 0$, $B_z = 0.04 T$

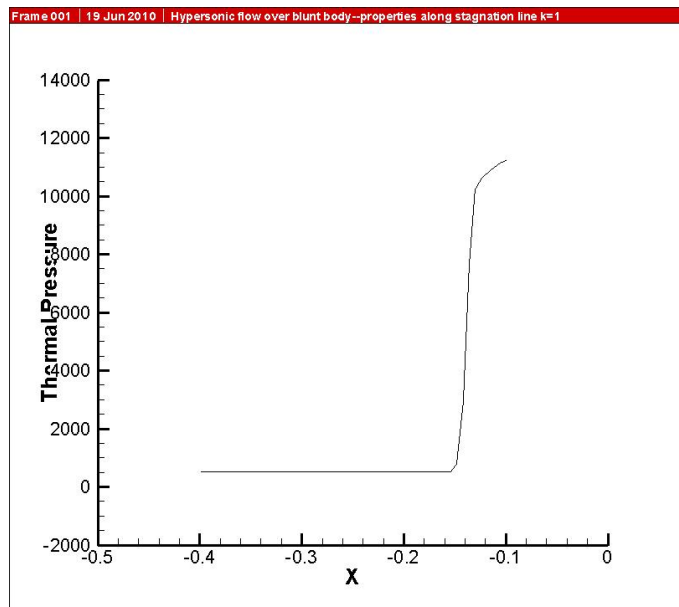


Figure 6.4: Thermal Pressure Profile along the Stagnation Line for Supersonic Flow Past an Axisymmetric Blunt Body; $M = 5.85$, $\alpha = 0^\circ$, $B_x = B_y = 0$, $B_z = 0.04 T$

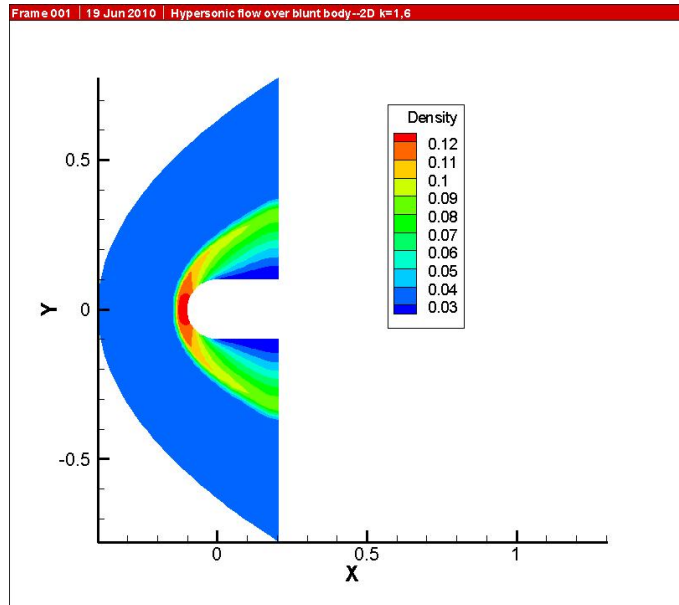


Figure 6.5: Density Contours in the $x-y$ Plane for Supersonic Flow Past an Axisymmetric Blunt Body; $M = 5.85$, $\alpha = 0^\circ$, $B_x = B_y = 0$, $B_z = 0.04$ T

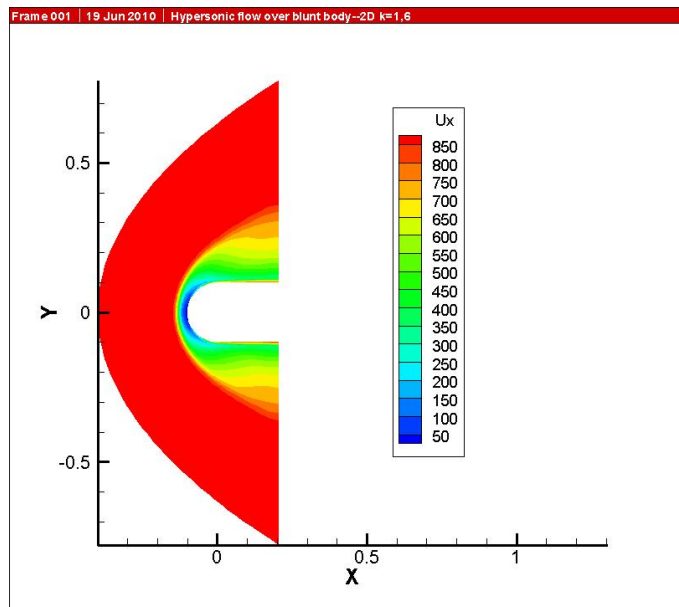


Figure 6.6: Velocity Contours in the $x-y$ Plane for Supersonic Flow Past an Axisymmetric Blunt Body; $M = 5.85$, $\alpha = 0^\circ$, $B_x = B_y = 0$, $B_z = 0.04$ T

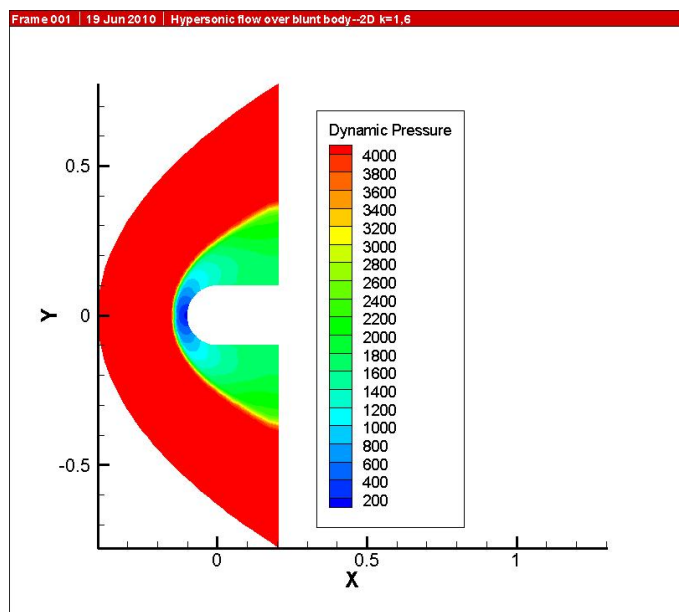


Figure 6.7: Dynamic Pressure Contours in the $x - y$ Plane for Supersonic Flow Past an Axisymmetric Blunt Body; $M = 5.85$, $\alpha = 0^\circ$, $B_x = B_y = 0$, $B_z = 0.04 T$

6.2 MHD Flowfield Computations at $M = 5.85$, $\alpha = 0^\circ$,

$$B_x = B_y = 0, B_z = 0.06 \text{ T}$$

In this case, the strength of the magnetic field is increased to $B_z = 0.06 \text{ T}$ to see its effect. Again, the grid of $40 \times 51 \times 10$ mesh points was employed to compute the results. Figure (6.8) shows the variation of density along the stagnation line. Figure (6.9) shows the variation in the streamwise velocity along the stagnation line. Figure (6.10) shows the variation in temperature along the stagnation line. Figure (6.11) shows the variation in thermal pressure along the stagnation line. Figure (6.12) shows the density contours in the $x - y$ plane. Figure (6.13) shows the contours of the streamwise velocity in $x - y$ plane. Figure (6.14) shows the dynamic pressure contours in the $x - y$ plane. These figures show that the increase in the intensity of the magnetic field further weakens the strength of the bow shock, thereby resulting in a greater reduction in shock wave drag. In section (6.3), the results of flow field calculations with and without magnetic field are compared.

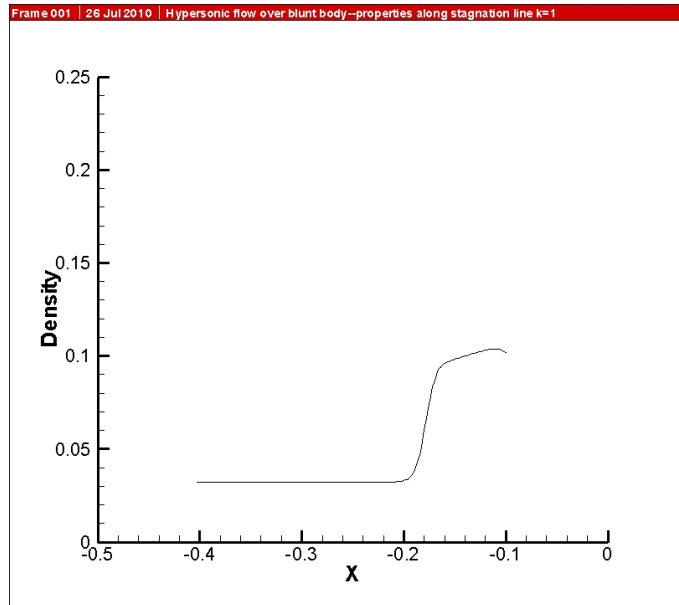


Figure 6.8: Density Profile along the Stagnation Line for Supersonic Flow Past an Axisymmetric Blunt Body; $M = 5.85$, $\alpha = 0^\circ$, $B_x = B_y = 0$, $B_z = 0.06$ T

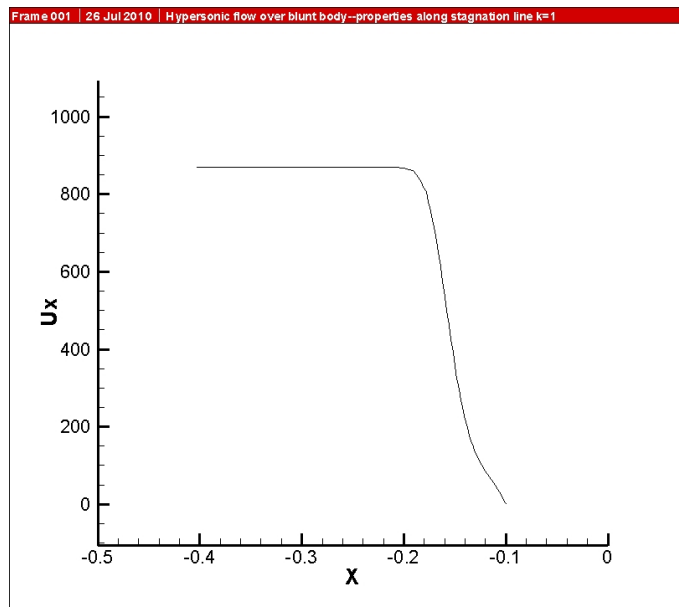


Figure 6.9: Streamwise Velocity Profile along the Stagnation Line for Supersonic Flow Past an Axisymmetric Blunt Body; $M = 5.85$, $\alpha = 0^\circ$, $B_x = B_y = 0$, $B_z = 0.06$ T

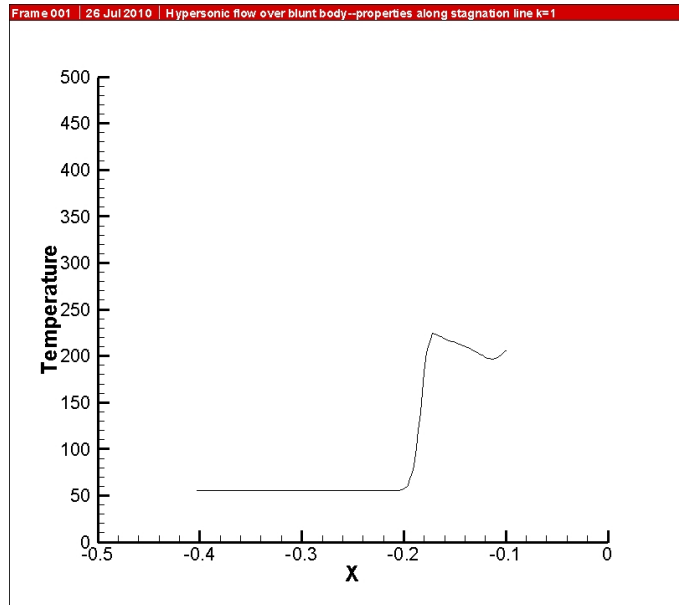


Figure 6.10: Temperature Profile along the Stagnation Line for Supersonic Flow Past an Axisymmetric Blunt Body; $M = 5.85$, $\alpha = 0^\circ$, $B_x = B_y = 0$, $B_z = 0.06 T$

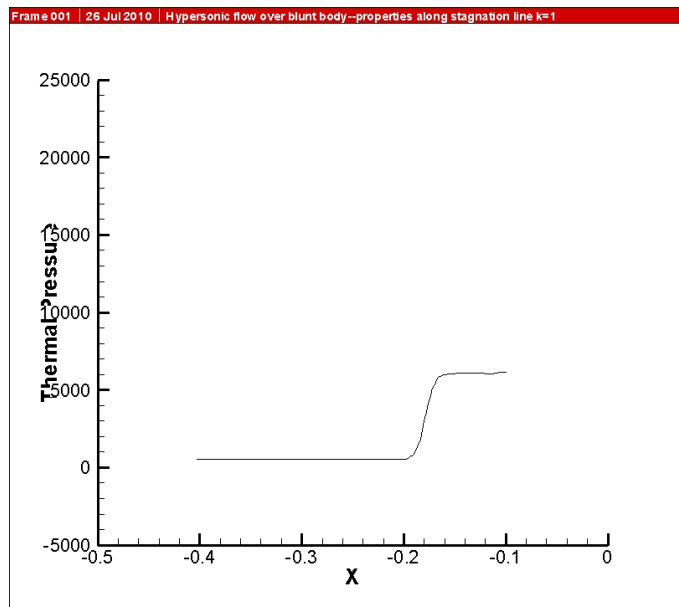


Figure 6.11: Thermal Pressure Profile along the Stagnation Line for Supersonic Flow Past an Axisymmetric Blunt Body; $M = 5.85$, $\alpha = 0^\circ$, $B_x = B_y = 0$, $B_z = 0.06 T$

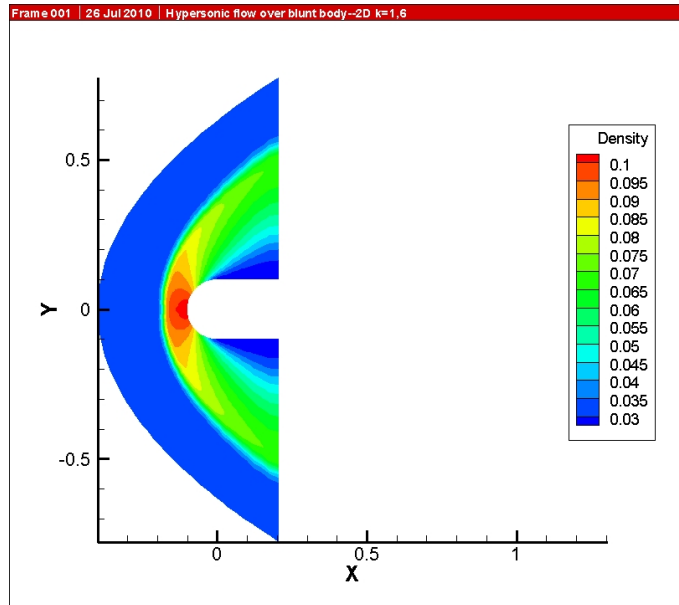


Figure 6.12: Density Contours in the $x - y$ Plane for Supersonic Flow Past an Axisymmetric Blunt Body; $M = 5.85$, $\alpha = 0^\circ$, $B_x = B_y = 0$, $B_z = 0.06$ T

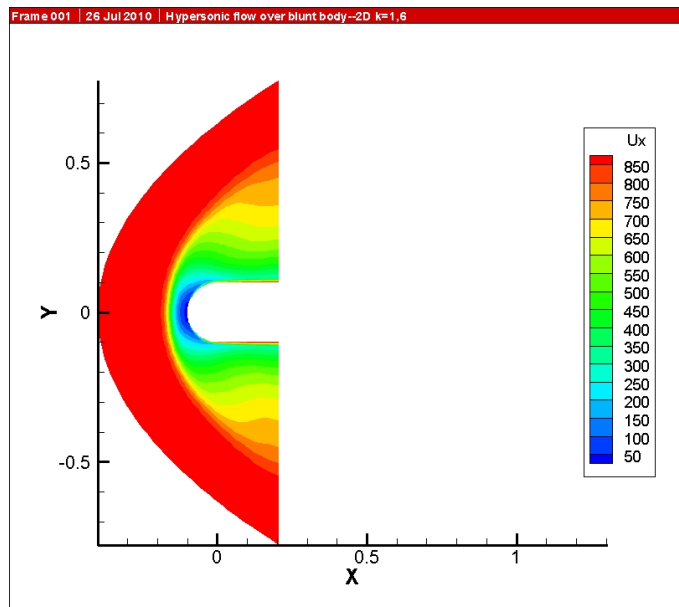


Figure 6.13: Velocity Contours in the $x - y$ Plane for Supersonic Flow Past an Axisymmetric Blunt Body; $M = 5.85$, $\alpha = 0^\circ$, $B_x = B_y = 0$, $B_z = 0.06$ T

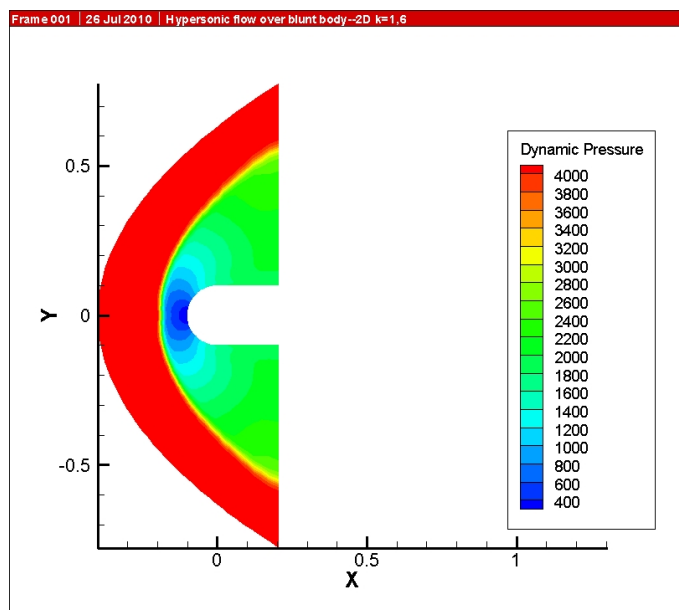


Figure 6.14: Dynamic Pressure Contours in the $x - y$ Plane for Supersonic Flow Past an Axisymmetric Blunt Body; $M = 5.85$, $\alpha = 0^\circ$, $B_x = B_y = 0$, $B_z = 0.06$ T

6.3 Comparison of Euler and MHD Flowfield

**Computations at $M = 5.85$, $\alpha = 0^\circ$, $B_x = B_y = 0$,
 $B_z = 0.04$ T **and** 0.06 T**

In this section, the comparison of flow fields with and without the magnetic field is presented. Figures (6.15) - (6.19) respectively show the variation of density, streamwise velocity, thermal pressure, static temperature and total pressure along the stagnation line. There are two physical effects that can be clearly observed: (1) The magnetic field decreases the strength of the bow shock and (2) the magnetic field pushes the shock further away from the body. Furthermore, for higher values of the magnetic field, these two effects become more pronounced. Thus, the magnetic field can be utilized in reducing the wave drag of aerospace vehicles at high speed.

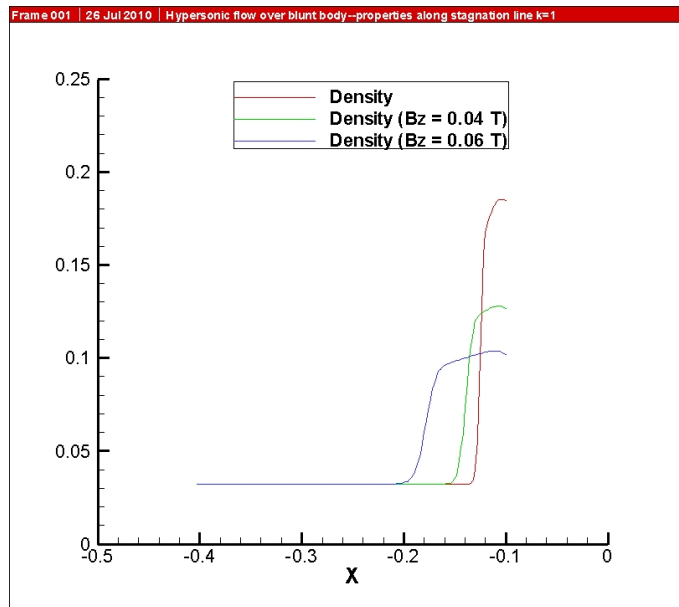


Figure 6.15: Comparison of Density Profiles along the Stagnation Line for Euler and MHD Supersonic Flow Past an Axisymmetric Blunt Body; $M = 5.85$, $\alpha = 0^\circ$, $B_x = B_y = 0$, $B_z = 0.04$ T and $B_z = 0.06$ T

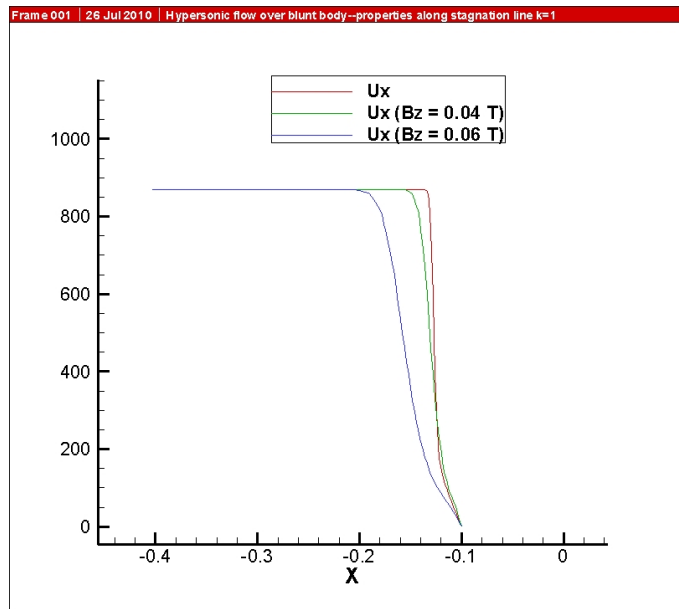


Figure 6.16: Comparison of Velocity Profiles along the Stagnation Line for Euler and MHD Supersonic Flow Past an Axisymmetric Blunt Body; $M = 5.85$, $\alpha = 0^\circ$, $B_x = B_y = 0$, $B_z = 0.04$ T and $B_z = 0.06$ T

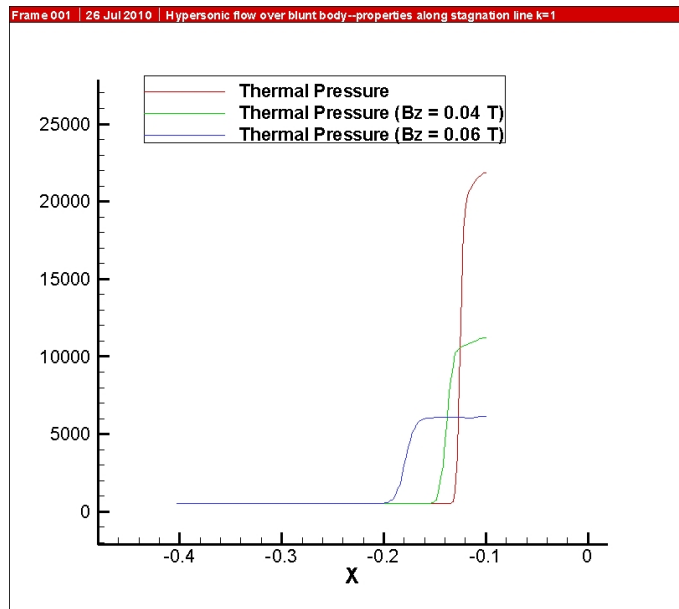


Figure 6.17: Comparison of Thermal Pressure Profiles along the Stagnation Line for Euler and MHD Supersonic Flow Past an Axisymmetric Blunt Body; $M = 5.85$, $\alpha = 0^\circ$, $B_x = B_y = 0$, $B_z = 0.04$ T and $B_z = 0.06$ T

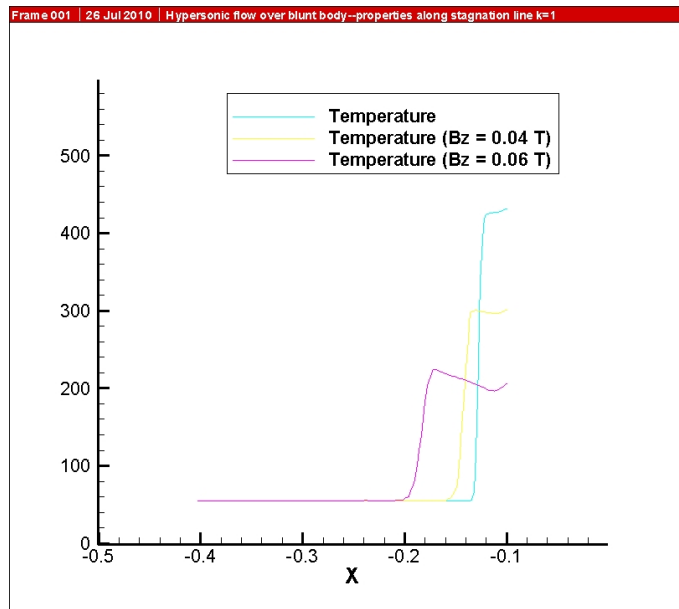


Figure 6.18: Comparison of Temperature Profiles along the Stagnation Line for Euler and MHD Supersonic Flow Past an Axisymmetric Blunt Body; $M = 5.85$, $\alpha = 0^\circ$, $B_x = B_y = 0$, $B_z = 0.04$ T and $B_z = 0.06$ T

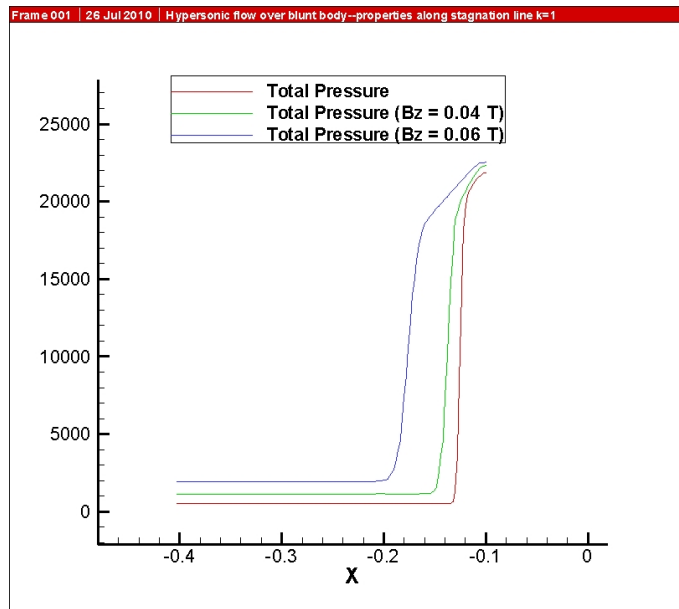


Figure 6.19: Comparison of Total Pressure Profiles along the Stagnation Line for Euler and MHD Supersonic Flow Past an Axisymmetric Blunt Body; $M = 5.85$, $\alpha = 0^\circ$, $B_x = B_y = 0$, $B_z = 0.04$ T and $B_z = 0.06$ T

Chapter 7

Summary

A class of explicit and implicit kinetic schemes, known as Kinetic Flux-Vector Split(KFVS) and Kinetic Wave-Particle Split (KWPS), have been developed for the numerical solution of Euler and ideal magnetohydrodynamics equation in 3-D orthogonal curvilinear coordinate systems. A 3-D computational code has been written using the explicit KWPS scheme to solve the 3-D Euler and ideal MHD equations. Other kinetic schemes can be easily included in the code with minor modifications. The code has been validated by computing 1-D and 2-D flows for which the computations of other investigators are available. The 3-D code has been applied to compute the Euler and MHD supersonic flow past an axisymmetric blunt body at an angle of attack. The computed Euler flowfields show the location of the shock upstream of the body in agreement with the prediction of the normal shock theory along the stagnation streamline.

The 3D codes based on explicit KWPS scheme for both the Euler and MHD equations have been successfully tested for the supersonic flow past an axisymmetric blunt body.

The code performed successfully in the 3-D generalized coordinate system. The kinetic schemes are found to be very robust and efficient.

The code can be used for studying the flowfields in a wide range of aerospace applications.

References

- [1] R.K. Agarwal and K.E. Acheson. A Kinetic Theory Based Wave/Particle Flux Splitting Scheme for the Euler Equations. *AIAA 95-2178*, 1995.
- [2] R.K. Agarwal and D.W. Halt. A Modified CUSP Scheme for Wave/Particle Split Form for Unstructured Grid Euler Flows. *Frontiers of Computational Fluid Dynamics*, I:155–168, 1994. John Wiley, NY.
- [3] R.K. Agarwal and H.S.R. Reksoprodjo. Implicit Kinetic Schemes for the Euler and Ideal MHD Equations. *Proc. of the 2nd Intl. Conf. on Comp. Fluid Dynamics 2 (ICCFD2)*, July 2002. Sydney, Australia, Springer-Verlag, Berlin.
- [4] J.D. Anderson. *Modern Compressible Flow with Historical Perspective*. McGraw-Hill, St. Louis, MO, 2nd edition, 1990.
- [5] R. Balakrishnan. *Entropy Consistent Formulation and Numerical Simulation of the BGK-Burnett Equations for Hypersonic Flows in the Continuum-Transition Regime*. PhD thesis, Wichita State University, 1999.
- [6] M.S. Brassiere and G. Gallice. A Roe Scheme for the Bi-Temperature Model of Magnetohydrodynamics. *Proc. of 16th Intl. Conf. on Num. Meth. in Fluid Dynamics*, pages 260–265, 1998. Arcachon, France, Springer-Verlag, Berlin.
- [7] M. Brio and C.C. Wu. An Upwind Differencing Schemes for the Equations of Ideal Magnetohydrodynamics. *J. Comp. Physics*, 75:400–422, 1988.
- [8] J.-P. Croisille, R. Khanfir, and G. Chanteur. Numerical Simulation of the MHD Equations by a Kinetic-type Method. *J. Sci. Comput.*, 10:481–492, 1995.
- [9] S.M. Deshpande. On the Maxwellian Distribution, Symmetric Form, and Entropy Conservation for the Euler Equations. *NASA TP 2583*, 1986.

- [10] S.M. Deshpande. Kinetic Flux-Splitting Schemes. *CFD Review*, pages 161–181, 1995.
- [11] S.M. Deshpande, P.S. Kulkarni, and A.K. Ghosh. New Developments in Kinetic Schemes. *Computers Math. Applic.*, 35(1/2):75–93, 1998.
- [12] W.M. Eppard and B. Grossman. An Upwind, Kinetic Flux-Vector Splitting Method for Flows in Chemical and Thermal Non-Equilibrium. *AIAA 93-0894*, 1993.
- [13] J.L. Estivalezes and P. Villedieu. A New Second Order Positivity Preserving Kinetic Schemes for the Compressible Euler Equations. *Proc. of the 15th Int. Conf. on Num. Meth. in Fluid Dynamics*, pages 96–100, 1996. Springer-Verlag, Berlin.
- [14] J.L. Estivalezes and P. Villedieu. High-Order Positivity-Preserving Kinetic Schemes for the Compressible Euler Equations. *SIAM J. Numer. Anal.*, 33(5):2050–2067, 1996.
- [15] K.A. Hoffman and S.T. Chiang. *Computational Fluid Dynamics for Engineers–Vol. I & II*. Engineering Education System, Wichita, KS, 2nd edition, 1993.
- [16] J.D. Huba and J.G. Lyon. A New 3D MHD Algorithm: The Distribution Function Method. *J. Plasma Physics*, 61:391–405, 1998.
- [17] H.W. Liepmann and Roshko A. *Elements of Gasdynamics*. Dover Publications, Mineola, NY, 2001.
- [18] M.-S. Liou and C.J. Steffen. A New Flux Splitting Scheme. *NASA TM-104404*, 1991.
- [19] R.W. MacCormack. An Upwind Conservation Form Method for the Ideal Magnetohydrodynamics Equations. *AIAA 99-3609*, 1999.

- [20] R.W. MacCormack. A Conservation Form Method for Magneto-Fluid Dynamics. *AIAA 2001-0195*, 2001.
- [21] J.C. Mandal and S.M. Deshpande. Kinetic Flux Vector Splitting for Euler Equations. *Computers and Fluids*, 23(2):447–478, 1994.
- [22] K.G. Powell. An Approximate Riemann Solver for Magnetohydrodynamics. *ICASE Report 94-24*, 1994.
- [23] K.H. Prendergast and K. Xu. Numerical Hydrodynamics from Gas-Kinetic Theory. *J. Comp. Physics*, 109:53–66, 1993.
- [24] W.H. Press, S.A. Teukolsky, W.T. Vetterling, and B.P. Flannery. *Numerical Recipes in FORTRAN*. Cambridge University Press, New York, NY, 2nd edition, 1992.
- [25] D.I. Pullin. Direct Simulation Methods for Compressible Inviscid Ideal-Gas Flow. *J. Comp. Physics*, 34:231–244, 1980.
- [26] K.S. Ravichandran. Higher Order KFVS Algorithms Using Compact Upwind Difference Operators. *J. Comp. Physics*, 130:161–173, 1997.
- [27] H.S.R. Reksoprodjo. Development of a Higher-order Accurate Kinetic Wave/Particle Flux-Splitting Algorithms for the Euler Equations. Master’s thesis, Wichita State University, 1999.
- [28] H.S.R. Reksoprodjo and R.K. Agarwal. A Higher-Order Kinetic Wave/Particle Flux-Splitting Algorithm for the Euler Equations. *AIAA 99-0920*, 1999.
- [29] H.S.R. Reksoprodjo and R.K. Agarwal. A Kinetic Scheme for Numerical Solution of Ideal Magnetohydrodynamics Equations with A Bi-Temperature Model. *AIAA 2000-0448*, 2000.

- [30] P.L. Roe. Approximate Riemann Solvers, Parameter Vectors and Difference Schemes. *J. Comp. Physics*, 43:357–372, 1981.
- [31] G.A. Sod. A Survey of Several Finite Difference Methods for Systems of Nonlinear Hyperbolic Conservation Laws. *J. Comp. Physics*, 27:1–31, 1978.
- [32] J.L. Steger and R.F. Warming. Flux Vector Splitting of the Inviscid Gas Dynamics Equations with Applications to Finite Difference Methods. *J. Comp. Physics*, 40:263–293, 1981.
- [33] H.-Z. Tang and K. Xu. A High-order Gas-kinetic Method for Multidimensional Ideal Magnetohydrodynamics. *J. Comp. Physics*, 165(1):69–88, 2000.
- [34] J.C. Tannehill, D.A. Anderson, and R.H. Pletcher. *Computational Fluid Mechanics and Heat Transfer*. Taylor and Francis, Washington, DC, 2nd edition, 1997.
- [35] B. van Leer. On the relation between the upwind-differencing schemes of Godunov, Engquist-Osher, and Roe. *ICASE Report 81-11*, 1981.
- [36] K. Xu. Gas-kinetic Theory Based Flux Splitting Method for Ideal Magnetohydrodynamics. *ICASE Report 98-53*, 1998.
- [37] K. Xu, L. Martinelli, and A. Jameson. Gas-Kinetic Finite Volume Methods, Flux-Vector Splitting, and Artificial Diffusion. *J. Comp. Physics*, 120:48–65, 1995.
- [38] K. Xu and K.H. Prendergast. Numerical Navier-Stokes Solutions from Gas-Kinetic Theory. *J. Comp. Physics*, 114:9–17, 1994.

APPENDICES

Appendix A

Derivation of the 1-D Kinetic Schemes for the Euler Equations

In Chapter 2 and Chapter 3, a mathematical connection between the Boltzmann equation and the Euler equations was presented. In the following sections, the methodology described as the “moment method strategy” is employed to derive the 1-D kinetic schemes, namely the explicit Kinetic Flux-Vector Split (KFVS) and the Kinetic Wave/Particle Split (KWPS) schemes. Note that the term “1-D” in the context of Boltzmann equation simply means that the other two velocity components of the fluid vanish ($u_2 = u_3 = 0$).

A.1 The Maxwellian Gas

The Maxwellian probability density distribution function describes the gas in a state of collisional equilibrium. It can be expressed as follows:

$$f^{(0)} = \frac{1}{\epsilon_o} \exp\left(-\frac{\epsilon}{\epsilon_o}\right) \left(\frac{\beta}{\pi}\right)^{3/2} \exp(-\beta(\vec{v} - \vec{u}) \cdot (\vec{v} - \vec{u})) \quad (\text{A.1})$$

where $\beta = \frac{\rho}{2p}$ is the equivalent temperature, $\rho = mn$ is the fluid density, and p is the fluid pressure. The internal energy term associated with the non-translational degrees of freedom is expressed in terms of the ideal gas constant R and temperature T as $\epsilon_o = \left(\frac{1}{\gamma-1} - \frac{3}{2}\right) RT$. Additionally, the molecular velocity \vec{v} can also be written as the sum of the fluid velocity \vec{u} and the thermal velocity \vec{c} .

The equilibrium Boltzmann equation can be written as:

$$\frac{\partial(nf)}{\partial t} + v_i \frac{\partial(nf)}{\partial x_i} = 0 \quad , \quad i = 1, 2, 3 \quad (\text{A.2})$$

where t is the time, n is the particle number density, f is the probability density distribution function, v_i are the components of the molecular velocity vector, and x_i are the components of the position vector.

The collisional invariant vector Ψ is the vector of quantities that are conserved during collisional processes, namely the mass, momentum, and the total energy of the individual gas particles:

$$\Psi = \left[m \quad m\vec{v} \quad m\epsilon + \frac{1}{2}m\vec{v} \cdot \vec{v} \right]^T \quad (\text{A.3})$$

In the following sections, the kinetic schemes for the 1-D Euler equations, namely the KFVS and the KWPS schemes, are derived. It has been noted that certain integrals are repeatedly used in the derivation of the schemes, therefore they are presented below.

Internal energy The integrals used are of the form $\int \exp(-\epsilon) d\epsilon$.

$$\begin{aligned}\int \exp(-\epsilon) d\epsilon &= -\exp(-\epsilon) + \mathcal{C} \\ \int \epsilon \exp(-\epsilon) d\epsilon &= -\epsilon \exp(-\epsilon) + \int \exp(-\epsilon) d\epsilon \\ \int \epsilon^2 \exp(-\epsilon) d\epsilon &= -\epsilon^2 \exp(-\epsilon) + 2 \int \epsilon \exp(-\epsilon) d\epsilon\end{aligned}$$

Molecular velocity First, note that the definition of the error function is

$$\operatorname{erf}(\phi) = \frac{1}{\sqrt{\pi}} \int_{-\phi}^{\phi} \exp(-\varphi^2) d\varphi = \frac{2}{\sqrt{\pi}} \int_0^{\phi} \exp(-\varphi^2) d\varphi$$

since $\exp(-\varphi^2)$ is an even function. In particular, $\operatorname{erf}(\infty) = 1$. In the following sections, the integrals involving the molecular velocity are of the form $\int \exp(-c^2) dc$.

$$\begin{aligned}\int \exp(-c^2) dc &\quad \textit{see definition of the error function} \\ \int c \exp(-c^2) dc &= -\frac{1}{2} \exp(-c^2) + \mathcal{C} \\ \int c^2 \exp(-c^2) dc &= -\frac{1}{2} c \exp(-c^2) + \frac{1}{2} \int \exp(-c^2) dc \\ \int c^3 \exp(-c^2) dc &= -\frac{1}{2} c^2 \exp(-c^2) + \int c \exp(-c^2) dc \\ \int c^4 \exp(-c^2) dc &= -\frac{1}{2} c^3 \exp(-c^2) + \frac{3}{2} \int c^2 \exp(-c^2) dc\end{aligned}$$

A.2 Conserved Variables (Field) Vector

The field variable vector \mathbf{Q} is obtained by taking the moments of (nf) with respect to the collision invariant vector. The detailed derivations are given as follows. Note that 1-D flow is assumed, that is $u_2 = u_3 = 0$. Taking $\Psi = m$:

$$\langle mnf \rangle = \rho \int_0^{\infty} \frac{1}{\epsilon_o} \exp\left(-\frac{\epsilon}{\epsilon_o}\right) d\epsilon \int_{-\infty}^{\infty} \sqrt{\frac{\beta}{\pi}} \exp(-\beta(v_1 - u_1)^2) dv_1$$

$$\times \int_{-\infty}^{\infty} \sqrt{\frac{\beta}{\pi}} \exp(-\beta v_2^2) dv_2 \int_{-\infty}^{\infty} \sqrt{\frac{\beta}{\pi}} \exp(-\beta v_3^2) dv_3$$

By substituting $\hat{\epsilon} = \frac{\epsilon}{\epsilon_0}$ and $\hat{c}_i = \sqrt{\beta}(v_i - u_i)$, simpler expressions are obtained:

$$\begin{aligned} \langle mnf \rangle &= \rho \int_0^{\infty} \exp(-\hat{\epsilon}) d\hat{\epsilon} \int_{-\infty}^{\infty} \frac{1}{\sqrt{\pi}} \exp(-\hat{c}_1^2) d\hat{c}_1 \\ &\quad \times \int_{-\infty}^{\infty} \frac{1}{\sqrt{\pi}} \exp(-\hat{c}_2^2) d\hat{c}_2 \int_{-\infty}^{\infty} \frac{1}{\sqrt{\pi}} \exp(-\hat{c}_3^2) d\hat{c}_3 \\ &= \rho \end{aligned} \tag{A.4}$$

Substituting $\Psi = mv_1$ gives:

$$\begin{aligned} \langle mnv_1f \rangle &= \rho \int_0^{\infty} \exp(-\hat{\epsilon}) d\hat{\epsilon} \int_{-\infty}^{\infty} \left(u_1 + \frac{1}{\sqrt{\beta}} \hat{c}_1 \right) \frac{1}{\sqrt{\pi}} \exp(-\hat{c}_1^2) d\hat{c}_1 \\ &\quad \times \int_{-\infty}^{\infty} \frac{1}{\sqrt{\pi}} \exp(-\hat{c}_2^2) d\hat{c}_2 \int_{-\infty}^{\infty} \frac{1}{\sqrt{\pi}} \exp(-\hat{c}_3^2) d\hat{c}_3 \\ &= \rho u_1 \end{aligned}$$

Yet, when $\Psi = mv_2$ and $\Psi = mv_3$ are used, the following expressions are obtained:

$$\begin{aligned} \langle mnv_2f \rangle &= \rho \int_0^{\infty} \exp(-\hat{\epsilon}) d\hat{\epsilon} \int_{-\infty}^{\infty} \frac{1}{\sqrt{\pi}} \exp(-\hat{c}_1^2) d\hat{c}_1 \\ &\quad \times \int_{-\infty}^{\infty} \frac{1}{\sqrt{\beta}} \hat{c}_2 \frac{1}{\sqrt{\pi}} \exp(-\hat{c}_2^2) d\hat{c}_2 \int_{-\infty}^{\infty} \frac{1}{\sqrt{\pi}} \exp(-\hat{c}_3^2) d\hat{c}_3 \\ &= 0 \end{aligned}$$

and

$$\begin{aligned} \langle mnv_3f \rangle &= \rho \int_0^{\infty} \exp(-\hat{\epsilon}) d\hat{\epsilon} \int_{-\infty}^{\infty} \frac{1}{\sqrt{\pi}} \exp(-\hat{c}_1^2) d\hat{c}_1 \\ &\quad \times \int_{-\infty}^{\infty} \frac{1}{\sqrt{\pi}} \exp(-\hat{c}_2^2) d\hat{c}_2 \int_{-\infty}^{\infty} \frac{1}{\sqrt{\beta}} \hat{c}_3 \frac{1}{\sqrt{\pi}} \exp(-\hat{c}_3^2) d\hat{c}_3 \\ &= 0 \end{aligned}$$

Finally, by using $\Psi = m\epsilon + \frac{1}{2}m(v_1^2 + v_2^2 + v_3^2)$, the following expression is obtained:

$$\begin{aligned}
\langle mn\epsilon f \rangle &= \rho \int_0^\infty \hat{\epsilon} \epsilon_o \exp(-\hat{\epsilon}) d\hat{\epsilon} \int_{-\infty}^\infty \frac{1}{\sqrt{\pi}} \exp(-\hat{c}_1^2) d\hat{c}_1 \\
&\quad \times \int_{-\infty}^\infty \frac{1}{\sqrt{\pi}} \exp(-\hat{c}_2^2) d\hat{c}_2 \int_{-\infty}^\infty \frac{1}{\sqrt{\pi}} \exp(-\hat{c}_3^2) d\hat{c}_3 \\
&= \rho \epsilon_o \\
\langle mn\frac{1}{2}v_1^2 f \rangle &= \rho \int_0^\infty \exp(-\hat{\epsilon}) d\hat{\epsilon} \int_{-\infty}^\infty \left(\frac{1}{2}u_1^2 + \frac{1}{\sqrt{\beta}}u_1\hat{c}_1 + \frac{1}{2\beta}\hat{c}_1^2 \right) \frac{1}{\sqrt{\pi}} \exp(-\hat{c}_1^2) d\hat{c}_1 \\
&\quad \times \int_{-\infty}^\infty \frac{1}{\sqrt{\pi}} \exp(-\hat{c}_2^2) d\hat{c}_2 \int_{-\infty}^\infty \frac{1}{\sqrt{\pi}} \exp(-\hat{c}_3^2) d\hat{c}_3 \\
&= \frac{1}{2}\rho u_1^2 + \rho \frac{1}{4\beta} \\
\langle mn\frac{1}{2}v_2^2 f \rangle &= \rho \int_0^\infty \exp(-\hat{\epsilon}) d\hat{\epsilon} \int_{-\infty}^\infty \frac{1}{\sqrt{\pi}} \exp(-\hat{c}_1^2) d\hat{c}_1 \\
&\quad \times \int_{-\infty}^\infty \frac{1}{2\beta}\hat{c}_2^2 \frac{1}{\sqrt{\pi}} \exp(-\hat{c}_2^2) d\hat{c}_2 \int_{-\infty}^\infty \frac{1}{\sqrt{\pi}} \exp(-\hat{c}_3^2) d\hat{c}_3 \\
&= \rho \frac{1}{4\beta} \\
\langle mn\frac{1}{2}v_3^2 f \rangle &= \rho \int_0^\infty \exp(-\hat{\epsilon}) d\hat{\epsilon} \int_{-\infty}^\infty \frac{1}{\sqrt{\pi}} \exp(-\hat{c}_1^2) d\hat{c}_1 \\
&\quad \times \int_{-\infty}^\infty \frac{1}{\sqrt{\pi}} \exp(-\hat{c}_2^2) d\hat{c}_2 \int_{-\infty}^\infty \frac{1}{2\beta}\hat{c}_3^2 \frac{1}{\sqrt{\pi}} \exp(-\hat{c}_3^2) d\hat{c}_3 \\
&= \rho \frac{1}{4\beta}
\end{aligned}$$

By using the definition for the average internal energy ($\epsilon_o = \left(\frac{1}{\gamma-1} - \frac{3}{2}\right) \frac{1}{2\beta}$) and the equation of state for ideal gas ($p = \rho \frac{1}{2\beta}$), the previous expressions can be combined and written as:

$$\langle mn \left(\epsilon + \frac{1}{2}v_k^2 \right) f \rangle = \rho e_t \quad (\text{A.5})$$

Thus, for the one-dimensional Euler equations, where $u_2 = u_3 = 0$, the vector \mathbf{Q} can be expressed as:

$$\mathbf{Q} = \left[\rho \quad \rho u_1 \quad \rho e_t \right]^T \quad (\text{A.6})$$

where $e_t = \frac{1}{2}u_k^2 + \frac{\gamma}{\gamma-1}\frac{1}{2\beta}$ is the specific total energy. Note that the equations for the transverse velocity components (u_2, u_3) have been dropped.

A.3 Kinetic-Flux-Vector-Splitting (KFVS) Scheme

Flux-Vector

The KFVS split-flux-vector along the direction x_1 can be obtained by splitting ($v_1 n f$) based on its sign and then taking the moments with respect to the collision invariant vector. For the mass conservation equation, $\Psi = m$, therefore:

$$\begin{aligned} \langle m n v_1^+ f \rangle &= \rho \int_0^\infty \frac{1}{\epsilon_o} \exp\left(-\frac{\epsilon}{\epsilon_o}\right) d\epsilon \int_{-\infty}^\infty \frac{v_1 + |v_1|}{2} \sqrt{\frac{\beta}{\pi}} \exp\left(-\beta(v_1 - u_1)^2\right) dv_1 \\ &\quad \times \int_{-\infty}^\infty \sqrt{\frac{\beta}{\pi}} \exp\left(-\beta v_2^2\right) dv_2 \int_{-\infty}^\infty \sqrt{\frac{\beta}{\pi}} \exp\left(-\beta v_3^2\right) dv_3 \end{aligned}$$

Substituting $\hat{\epsilon} = \frac{\epsilon}{\epsilon_o}$ and $\hat{c}_i = \sqrt{\beta}(v_i - u_i)$,

$$\begin{aligned} \langle m n v_1^+ f \rangle &= \rho \int_0^\infty \exp(-\hat{\epsilon}) d\hat{\epsilon} \int_{-u_1\sqrt{\beta}}^\infty \left(u_1 + \frac{1}{\sqrt{\beta}}\hat{c}_1\right) \frac{1}{\sqrt{\pi}} \exp\left(-\hat{c}_1^2\right) d\hat{c}_1 \\ &\quad \times \int_{-\infty}^\infty \frac{1}{\sqrt{\pi}} \exp\left(-\hat{c}_2^2\right) d\hat{c}_2 \int_{-\infty}^\infty \frac{1}{\sqrt{\pi}} \exp\left(-\hat{c}_3^2\right) d\hat{c}_3 \\ &= \frac{1 + \operatorname{erf}\left(u_1\sqrt{\beta}\right)}{2} (\rho u_1) + \frac{\exp\left(-u_1^2\beta\right)}{2\sqrt{\pi\beta}} (\rho) \end{aligned} \tag{A.7}$$

where $\operatorname{erf}(\phi) = \frac{2}{\sqrt{\pi}} \int_0^\phi \exp(-\varphi^2) d\varphi$ is the error function.

By substituting $\Psi = m v_1$ the following expression is obtained:

$$\langle m n v_1^+ v_1 f \rangle = \rho \int_0^\infty \exp(-\hat{\epsilon}) d\hat{\epsilon} \int_{-u_1\sqrt{\beta}}^\infty \left(u_1 + \frac{1}{\sqrt{\beta}}\hat{c}_1\right)^2 \frac{1}{\sqrt{\pi}} \exp\left(-\hat{c}_1^2\right) d\hat{c}_1$$

$$\begin{aligned}
& \times \int_{-\infty}^{\infty} \frac{1}{\sqrt{\pi}} \exp(-\hat{c}_2^2) d\hat{c}_2 \int_{-\infty}^{\infty} \frac{1}{\sqrt{\pi}} \exp(-\hat{c}_3^2) d\hat{c}_3 \\
& = \frac{1+\operatorname{erf}\left(\frac{u_1\sqrt{\beta}}{2}\right)}{2} \left(\rho u_1^2 + \rho \frac{1}{2\beta}\right) + \frac{\exp(-\frac{u_1^2\beta}{2})}{2\sqrt{\pi\beta}} (\rho u_1)
\end{aligned}$$

Applying the equation of state of an ideal gas

$$p = \rho RT = \frac{\rho}{2\beta}$$

results in:

$$\langle mnv_1^+ v_1 f \rangle = \frac{1+\operatorname{erf}\left(\frac{u_1\sqrt{\beta}}{2}\right)}{2} (\rho u_1^2 + p) + \frac{\exp(-\frac{u_1^2\beta}{2})}{2\sqrt{\pi\beta}} (\rho u_1) \quad (\text{A.8})$$

When $\Psi = mv_2$ and $\Psi = mv_3$ are used, the following expressions are obtained:

$$\begin{aligned}
\langle mnv_1^+ v_2 f \rangle & = \rho \int_0^{\infty} \exp(-\hat{\epsilon}) d\hat{\epsilon} \int_{-u_1\sqrt{\beta}}^{\infty} \left(u_1 + \frac{1}{\sqrt{\beta}}\hat{c}_1\right) \frac{1}{\sqrt{\pi}} \exp(-\hat{c}_1^2) d\hat{c}_1 \\
& \times \int_{-\infty}^{\infty} \frac{1}{\sqrt{\beta}} \hat{c}_2 \frac{1}{\sqrt{\pi}} \exp(-\hat{c}_2^2) d\hat{c}_2 \int_{-\infty}^{\infty} \frac{1}{\sqrt{\pi}} \exp(-\hat{c}_3^2) d\hat{c}_3 \\
& = 0
\end{aligned} \quad (\text{A.9})$$

and

$$\begin{aligned}
\langle mnv_1^+ v_3 f \rangle & = \rho \int_0^{\infty} \exp(-\hat{\epsilon}) d\hat{\epsilon} \int_{-u_1\sqrt{\beta}}^{\infty} \left(u_1 + \frac{1}{\sqrt{\beta}}\hat{c}_1\right) \frac{1}{\sqrt{\pi}} \exp(-\hat{c}_1^2) d\hat{c}_1 \\
& \times \int_{-\infty}^{\infty} \frac{1}{\sqrt{\pi}} \exp(-\hat{c}_2^2) d\hat{c}_2 \int_{-\infty}^{\infty} \frac{1}{\sqrt{\beta}} \hat{c}_3 \frac{1}{\sqrt{\pi}} \exp(-\hat{c}_3^2) d\hat{c}_3 \\
& = 0
\end{aligned} \quad (\text{A.10})$$

And finally by employing $\Psi = m\epsilon + \frac{1}{2}m(v_1^2 + v_2^2 + v_3^2)$, the split-fluxes for the energy equation are obtained:

$$\langle mnv_1^+ \epsilon f \rangle = \rho \int_0^{\infty} \hat{\epsilon} \epsilon_o \exp(-\hat{\epsilon}) d\hat{\epsilon} \int_{-u_1\sqrt{\beta}}^{\infty} \left(u_1 + \frac{1}{\sqrt{\beta}}\hat{c}_1\right) \frac{1}{\sqrt{\pi}} \exp(-\hat{c}_1^2) d\hat{c}_1$$

$$\begin{aligned}
& \times \int_{-\infty}^{\infty} \frac{1}{\sqrt{\pi}} \exp(-\hat{c}_2^2) d\hat{c}_2 \int_{-\infty}^{\infty} \frac{1}{\sqrt{\pi}} \exp(-\hat{c}_3^2) d\hat{c}_3 \\
& = \frac{1+\operatorname{erf}(u_1\sqrt{\beta})}{2} (\rho u_1 \epsilon_o) + \frac{\exp(-u_1^2\beta)}{2\sqrt{\pi\beta}} (\rho \epsilon_o) \\
\langle mnv_1^+ \frac{1}{2} v_1^2 f \rangle & = \rho \int_0^{\infty} \exp(-\hat{\epsilon}) d\hat{\epsilon} \int_{-u_1\sqrt{\beta}}^{\infty} \frac{1}{2} \left(u_1 + \frac{1}{\sqrt{\beta}} \hat{c}_1 \right)^3 \frac{1}{\sqrt{\pi}} \exp(-\hat{c}_1^2) d\hat{c}_1 \\
& \times \int_{-\infty}^{\infty} \frac{1}{\sqrt{\pi}} \exp(-\hat{c}_2^2) d\hat{c}_2 \int_{-\infty}^{\infty} \frac{1}{\sqrt{\pi}} \exp(-\hat{c}_3^2) d\hat{c}_3 \\
& = \frac{1+\operatorname{erf}(u_1\sqrt{\beta})}{2} \left(\frac{1}{2} \rho u_1^3 + \frac{3}{2} p u_1 \right) + \frac{\exp(-u_1^2\beta)}{2\sqrt{\pi\beta}} \left(\frac{1}{2} \rho u_1^2 + p \right) \\
\langle mnv_1^+ \frac{1}{2} v_2^2 f \rangle & = \rho \int_0^{\infty} \exp(-\hat{\epsilon}) d\hat{\epsilon} \int_{-u_1\sqrt{\beta}}^{\infty} \left(u_1 + \frac{1}{\sqrt{\beta}} \hat{c}_1 \right) \frac{1}{\sqrt{\pi}} \exp(-\hat{c}_1^2) d\hat{c}_1 \\
& \times \int_{-\infty}^{\infty} \frac{1}{2\beta} \hat{c}_2^2 \frac{1}{\sqrt{\pi}} \exp(-\hat{c}_2^2) d\hat{c}_2 \int_{-\infty}^{\infty} \frac{1}{\sqrt{\pi}} \exp(-\hat{c}_3^2) d\hat{c}_3 \\
& = \frac{1+\operatorname{erf}(u_1\sqrt{\beta})}{2} \left(\frac{1}{2} p u_1 \right) + \frac{\exp(-u_1^2\beta)}{2\sqrt{\pi\beta}} \left(\frac{1}{2} p \right) \\
\langle mnv_1^+ \frac{1}{2} v_3^2 f \rangle & = \rho \int_0^{\infty} \exp(-\hat{\epsilon}) d\hat{\epsilon} \int_{-u_1\sqrt{\beta}}^{\infty} \left(u_1 + \frac{1}{\sqrt{\beta}} \hat{c}_1 \right) \frac{1}{\sqrt{\pi}} \exp(-\hat{c}_1^2) d\hat{c}_1 \\
& \times \int_{-\infty}^{\infty} \frac{1}{\sqrt{\pi}} \exp(-\hat{c}_2^2) d\hat{c}_2 \int_{-\infty}^{\infty} \frac{1}{2\beta} \hat{c}_3^2 \frac{1}{\sqrt{\pi}} \exp(-\hat{c}_3^2) d\hat{c}_3 \\
& = \frac{1+\operatorname{erf}(u_1\sqrt{\beta})}{2} \left(\frac{1}{2} p u_1 \right) + \frac{\exp(-u_1^2\beta)}{2\sqrt{\pi\beta}} \left(\frac{1}{2} p \right)
\end{aligned}$$

By using the definition for the average internal energy $(\epsilon_o = (\frac{1}{\gamma-1} - \frac{3}{2}) \frac{1}{2\beta})$, the KFVS split-flux for the energy equation is expressed as:

$$\langle mnv_1^+ \left(\epsilon + \frac{1}{2} v_k^2 \right) f \rangle = \frac{1+\operatorname{erf}(u_1\sqrt{\beta})}{2} (\rho u_1 e_t + p u_1) + \frac{\exp(-u_1^2\beta)}{2\sqrt{\pi\beta}} (\rho e_t + \frac{1}{2} p) \quad (\text{A.11})$$

Thus, the KFVS split-flux-vector for the Euler equations can be written as:

$$\mathbf{F}^{\pm} = \frac{1 \pm \operatorname{erf}(u_1 \sqrt{\beta})}{2} \begin{bmatrix} \rho u_1 \\ \rho u_1^2 + p \\ \rho u_1 e_t + p u_1 \end{bmatrix} \pm \frac{\exp(-u_1^2 \beta)}{2\sqrt{\pi\beta}} \begin{bmatrix} \rho \\ \rho u_1 \\ \rho e_t + \frac{1}{2}p \end{bmatrix} \quad (\text{A.12})$$

A.4 Kinetic-Wave-Particle-Splitting (KWPS) Scheme

Flux-Vector

In the derivation of the KWPS split-flux-vectors, it is recognized that the molecular velocity \vec{v} can be expressed as the sum of the fluid velocity \vec{u} and the thermal velocity \vec{c} . Upwinding can then be applied to each of the velocities \vec{u} and \vec{c} separately. This results in much simpler expressions compared to the KFVS formulation.

By using the fluid velocity \vec{u} as the basis for the upwinding, the following expression is obtained when moments are taken with respect to the collision invariant vector:

$$\langle u_1^+ n f \Psi \rangle = \frac{u_1 + |u_1|}{2} \langle n f \Psi \rangle \quad (\text{A.13})$$

In equation A.13 the fluid velocity can be taken outside the integrations. However, this is equivalent to:

$$\langle u_1^+ n f \Psi \rangle = \frac{u_1 + |u_1|}{2} \mathbf{Q} \quad (\text{A.14})$$

This implies that the information contained in the conserved variable vector is convected at exactly the fluid velocity, hence the name “particle” flux.

The “wave” flux is obtained by splitting the thermal velocity \vec{c} . The derivation of the split-flux terms for the “wave” flux is given below.

Letting $\Psi = m$, the following expression is obtained:

$$\begin{aligned}
\langle mnc_1^+ f \rangle &= \rho \int_0^\infty \exp(-\hat{\epsilon}) d\hat{\epsilon} \int_0^\infty \frac{1}{\sqrt{\beta}} \hat{c}_1 \frac{1}{\sqrt{\pi}} \exp(-\hat{c}_1^2) d\hat{c}_1 \\
&\quad \times \int_{-\infty}^\infty \frac{1}{\sqrt{\pi}} \exp(-\hat{c}_2^2) d\hat{c}_2 \int_{-\infty}^\infty \frac{1}{\sqrt{\pi}} \exp(-\hat{c}_3^2) d\hat{c}_3 \\
&= \frac{1}{2\sqrt{\pi\beta}} (\rho)
\end{aligned} \tag{A.15}$$

By substituting $\Psi = mv_1$, the following expression is obtained:

$$\begin{aligned}
\langle mnc_1^+ v_1 f \rangle &= \rho \int_0^\infty \exp(-\hat{\epsilon}) d\hat{\epsilon} \int_0^\infty \frac{1}{\sqrt{\beta}} \hat{c}_1 \left(u_1 + \frac{1}{\sqrt{\beta}} \hat{c}_1 \right) \frac{1}{\sqrt{\pi}} \exp(-\hat{c}_1^2) d\hat{c}_1 \\
&\quad \times \int_{-\infty}^\infty \frac{1}{\sqrt{\pi}} \exp(-\hat{c}_2^2) d\hat{c}_2 \int_{-\infty}^\infty \frac{1}{\sqrt{\pi}} \exp(-\hat{c}_3^2) d\hat{c}_3 \\
&= \frac{1}{2\sqrt{\pi\beta}} (\rho u_1) + \frac{1}{2} (p)
\end{aligned} \tag{A.16}$$

When $\Psi = mv_2$ and $\Psi = mv_3$ are used, the following expressions are obtained:

$$\begin{aligned}
\langle mnc_1^+ v_2 f \rangle &= \rho \int_0^\infty \exp(-\hat{\epsilon}) d\hat{\epsilon} \int_0^\infty \frac{1}{\sqrt{\beta}} \hat{c}_1 \frac{1}{\sqrt{\pi}} \exp(-\hat{c}_1^2) d\hat{c}_1 \\
&\quad \times \int_{-\infty}^\infty \frac{1}{\sqrt{\beta}} \hat{c}_2 \frac{1}{\sqrt{\pi}} \exp(-\hat{c}_2^2) d\hat{c}_2 \int_{-\infty}^\infty \frac{1}{\sqrt{\pi}} \exp(-\hat{c}_3^2) d\hat{c}_3 \\
&= 0
\end{aligned} \tag{A.17}$$

and

$$\begin{aligned}
\langle mnc_1^+ v_3 f \rangle &= \rho \int_0^\infty \exp(-\hat{\epsilon}) d\hat{\epsilon} \int_0^\infty \frac{1}{\sqrt{\beta}} \hat{c}_1 \frac{1}{\sqrt{\pi}} \exp(-\hat{c}_1^2) d\hat{c}_1 \\
&\quad \times \int_{-\infty}^\infty \frac{1}{\sqrt{\pi}} \exp(-\hat{c}_2^2) d\hat{c}_2 \int_{-\infty}^\infty \frac{1}{\sqrt{\beta}} \hat{c}_3 \frac{1}{\sqrt{\pi}} \exp(-\hat{c}_3^2) d\hat{c}_3 \\
&= 0
\end{aligned} \tag{A.18}$$

And finally by employing $\Psi = m\epsilon + \frac{1}{2}m(v_1^2 + v_2^2 + v_3^2)$, the split-fluxes for the energy

equation are obtained:

$$\begin{aligned}
\langle mnc_1^+ \epsilon f \rangle &= \rho \int_0^\infty \hat{\epsilon} \epsilon_o \exp(-\hat{\epsilon}) d\hat{\epsilon} \int_0^\infty \frac{1}{\sqrt{\beta}} \hat{c}_1 \frac{1}{\sqrt{\pi}} \exp(-\hat{c}_1^2) d\hat{c}_1 \\
&\quad \times \int_{-\infty}^\infty \frac{1}{\sqrt{\pi}} \exp(-\hat{c}_2^2) d\hat{c}_2 \int_{-\infty}^\infty \frac{1}{\sqrt{\pi}} \exp(-\hat{c}_3^2) d\hat{c}_3 \\
&= \frac{1}{2\sqrt{\pi\beta}} (\rho \epsilon_o) \\
\langle mnc_1^+ \frac{1}{2} v_1^2 f \rangle &= \rho \int_0^\infty \exp(-\hat{\epsilon}) d\hat{\epsilon} \int_0^\infty \frac{1}{\sqrt{\beta}} \hat{c}_1 \frac{1}{2} \left(u_1 + \frac{1}{\sqrt{\beta}} \hat{c}_1 \right)^2 \frac{1}{\sqrt{\pi}} \exp(-\hat{c}_1^2) d\hat{c}_1 \\
&\quad \times \int_{-\infty}^\infty \frac{1}{\sqrt{\pi}} \exp(-\hat{c}_2^2) d\hat{c}_2 \int_{-\infty}^\infty \frac{1}{\sqrt{\pi}} \exp(-\hat{c}_3^2) d\hat{c}_3 \\
&= \frac{1}{2\sqrt{\pi\beta}} \left(\frac{1}{2} \rho u_1^2 + p \right) + \frac{1}{2} (p u_1) \\
\langle mnc_1^+ \frac{1}{2} v_2^2 f \rangle &= \rho \int_0^\infty \exp(-\hat{\epsilon}) d\hat{\epsilon} \int_0^\infty \frac{1}{\sqrt{\beta}} \hat{c}_1 \frac{1}{\sqrt{\pi}} \exp(-\hat{c}_1^2) d\hat{c}_1 \\
&\quad \times \int_{-\infty}^\infty \frac{1}{2\beta} \hat{c}_2^2 \frac{1}{\sqrt{\pi}} \exp(-\hat{c}_2^2) d\hat{c}_2 \int_{-\infty}^\infty \frac{1}{\sqrt{\pi}} \exp(-\hat{c}_3^2) d\hat{c}_3 \\
&= \frac{1}{2\sqrt{\pi\beta}} \left(\frac{1}{2} p \right) \\
\langle mnc_1^+ \frac{1}{2} v_3^2 f \rangle &= \rho \int_0^\infty \exp(-\hat{\epsilon}) d\hat{\epsilon} \int_0^\infty \frac{1}{\sqrt{\beta}} \hat{c}_1 \frac{1}{\sqrt{\pi}} \exp(-\hat{c}_1^2) d\hat{c}_1 \\
&\quad \times \int_{-\infty}^\infty \frac{1}{\sqrt{\pi}} \exp(-\hat{c}_2^2) d\hat{c}_2 \int_{-\infty}^\infty \frac{1}{2\beta} \hat{c}_3^2 \frac{1}{\sqrt{\pi}} \exp(-\hat{c}_3^2) d\hat{c}_3 \\
&= \frac{1}{2\sqrt{\pi\beta}} \left(\frac{1}{2} p \right)
\end{aligned}$$

Simplifying:

$$\langle mnc_1^+ \left(\epsilon + \frac{1}{2} v_k^2 \right) f \rangle = \frac{1}{2} (p u_1) + \frac{1}{2\sqrt{\pi\beta}} \left(\rho e_t + \frac{1}{2} p \right) \quad (\text{A.19})$$

Thus, the KWPS split-flux-vector for the one-dimensional Euler equations is obtained as:

$$\mathbf{F}^\pm = \frac{u_1 \pm |u_1|}{2} \begin{bmatrix} \rho \\ \rho u_1 \\ \rho e_t \end{bmatrix} + \frac{1}{2} \begin{bmatrix} 0 \\ p \\ p u_1 \end{bmatrix} \pm \frac{1}{2\sqrt{\pi\beta}} \begin{bmatrix} \rho \\ \rho u_1 \\ \rho e_t + \frac{1}{2} p \end{bmatrix} \quad (\text{A.20})$$

Appendix B

Metrics of Transformation for the Generalized Curvilinear Coordinate System

B.1 Computation of the Metrics of Transformation

The solution of the Euler equations about an arbitrary geometry can be facilitated by employing a body conforming grid system. The numerical computation, however, is far more convenient to be conducted over a simple Cartesian grid. To connect both the physical (consisting of orthogonal curvilinear grid lines) and computational (consisting of Cartesian grid lines) spaces, a method of coordinate transformation is applied.

Define the following one-to-one relationships connecting the computational coordinates

(ξ, η, ζ) as functions of the physical space coordinates (x, y, z) :

$$\xi = \xi(x, y, z)$$

$$\eta = \eta(x, y, z)$$

$$\zeta = \zeta(x, y, z)$$

A differential form of the above expressions can be written as:

$$\begin{bmatrix} d\xi \\ d\eta \\ d\zeta \end{bmatrix} = \begin{bmatrix} \xi_x & \xi_y & \xi_z \\ \eta_x & \eta_y & \eta_z \\ \zeta_x & \zeta_y & \zeta_z \end{bmatrix} \begin{bmatrix} dx \\ dy \\ dz \end{bmatrix} \quad (\text{B.1})$$

where the subscripts denote partial differentiations.

In general, it is much easier to define the physical space coordinates as functions of the computational space coordinates. This can be achieved by reversing the role of dependent and independent variables in equation (B.1) as follows:

$$\begin{bmatrix} dx \\ dy \\ dz \end{bmatrix} = \begin{bmatrix} x_\xi & x_\eta & x_\zeta \\ y_\xi & y_\eta & y_\zeta \\ z_\xi & z_\eta & z_\zeta \end{bmatrix} \begin{bmatrix} d\xi \\ d\eta \\ d\zeta \end{bmatrix} \quad (\text{B.2})$$

from which the metrics of coordinate transformation can be obtained as:

$$\begin{aligned} \begin{bmatrix} \xi_x & \xi_y & \xi_z \\ \eta_x & \eta_y & \eta_z \\ \zeta_x & \zeta_y & \zeta_z \end{bmatrix} &= \begin{bmatrix} x_\xi & x_\eta & x_\zeta \\ y_\xi & y_\eta & y_\zeta \\ z_\xi & z_\eta & z_\zeta \end{bmatrix}^{-1} \\ &= \mathcal{J} \begin{bmatrix} y_\eta z_\zeta - y_\zeta z_\eta & z_\eta x_\zeta - z_\zeta x_\eta & x_\eta y_\zeta - x_\zeta y_\eta \\ y_\zeta z_\xi - y_\xi z_\zeta & z_\zeta x_\xi - z_\xi x_\zeta & x_\zeta y_\xi - x_\xi y_\zeta \\ y_\xi z_\eta - y_\eta z_\xi & z_\xi x_\eta - z_\eta x_\xi & x_\xi y_\eta - x_\eta y_\xi \end{bmatrix} \end{aligned} \quad (\text{B.3})$$

where \mathcal{J} is the Jacobian of coordinate transformation defined as:

$$\mathcal{J} = \begin{vmatrix} x_\xi & x_\eta & x_\zeta \\ y_\xi & y_\eta & y_\zeta \\ z_\xi & z_\eta & z_\zeta \end{vmatrix}^{-1} = \frac{1}{(x_\xi y_\eta z_\zeta + x_\eta y_\zeta z_\xi + x_\zeta y_\xi z_\eta) - (z_\xi y_\eta x_\zeta + z_\eta y_\zeta x_\xi + z_\zeta y_\xi x_\eta)}$$

B.2 Differentiation of the Metrics of Transformation

In the derivation of the Poisson solver, the need to evaluate the spatial derivatives of the metrics of transformation arises. The Laplacian of an arbitrary function ϕ in the Cartesian coordinates is defined as:

$$\nabla^2 \phi = \phi_{xx} + \phi_{yy} + \phi_{zz} \quad (\text{B.4})$$

In a generalized curvilinear coordinate system, the equation (B.4) becomes more involved. The following illustrates the additional terms that need to be added:

$$\begin{aligned} \nabla^2 \phi &= \left(\xi_x \frac{\partial}{\partial \xi} + \eta_x \frac{\partial}{\partial \eta} + \zeta_x \frac{\partial}{\partial \zeta} \right) (\xi_x \phi_\xi + \eta_x \phi_\eta + \zeta_x \phi_\zeta) \\ &\quad + \left(\xi_y \frac{\partial}{\partial \xi} + \eta_y \frac{\partial}{\partial \eta} + \zeta_y \frac{\partial}{\partial \zeta} \right) (\xi_y \phi_\xi + \eta_y \phi_\eta + \zeta_y \phi_\zeta) \\ &\quad + \left(\xi_z \frac{\partial}{\partial \xi} + \eta_z \frac{\partial}{\partial \eta} + \zeta_z \frac{\partial}{\partial \zeta} \right) (\xi_z \phi_\xi + \eta_z \phi_\eta + \zeta_z \phi_\zeta) \\ &= (\xi, \xi) \phi_{\xi\xi} + (\eta, \eta) \phi_{\eta\eta} + (\zeta, \zeta) \phi_{\zeta\zeta} \\ &\quad + 2(\xi, \eta) \phi_{\xi\eta} + 2(\eta, \zeta) \phi_{\eta\zeta} + 2(\zeta, \xi) \phi_{\zeta\xi} \\ &\quad + \nabla^2 \xi \phi_\xi + \nabla^2 \eta \phi_\eta + \nabla^2 \zeta \phi_\zeta \end{aligned}$$

where the terms such as $(\xi, \xi) = \xi_x^2 + \xi_y^2 + \xi_z^2$ indicate the inner products. The Laplacian of the coordinate ξ is defined as follows:

$$\nabla^2 \xi = \xi_x \frac{\partial}{\partial \xi} (\xi_x) + \eta_x \frac{\partial}{\partial \eta} (\xi_x) + \zeta_x \frac{\partial}{\partial \zeta} (\xi_x)$$

$$\begin{aligned}
& + \xi_y \frac{\partial}{\partial \xi} (\xi_y) + \eta_y \frac{\partial}{\partial \eta} (\xi_y) + \zeta_y \frac{\partial}{\partial \zeta} (\xi_y) \\
& + \xi_z \frac{\partial}{\partial \xi} (\xi_z) + \eta_z \frac{\partial}{\partial \eta} (\xi_z) + \zeta_z \frac{\partial}{\partial \zeta} (\xi_z)
\end{aligned}$$

The Laplacians of the other coordinates η and ζ are obtained by using appropriate substitutions. Finally, the derivatives of the metrics of coordinate transformation, e.g. $\frac{\partial}{\partial \xi} (\xi_x)$, can be obtained using the definition of the Jacobian of transformation \mathcal{J} as follows:

$$\begin{aligned}
\frac{\partial}{\partial \xi} (\xi_x) &= \frac{\partial}{\partial \xi} [\mathcal{J} (y_\eta z_\zeta - y_\zeta z_\eta)] \\
&= \mathcal{J} (y_{\xi\eta} z_\zeta - y_{\zeta\xi} z_\eta + z_{\zeta\xi} y_\eta - z_{\xi\eta} y_\zeta) + \mathcal{J}_\xi (y_\eta z_\zeta - y_\zeta z_\eta)
\end{aligned}$$

Expanding \mathcal{J}_ξ

$$\begin{aligned}
\mathcal{J}_\xi &= -\mathcal{J}^2 [(x_{\xi\xi} y_\eta z_\zeta + x_\eta y_\zeta z_{\xi\xi} + x_\zeta y_{\xi\xi} z_\eta) - (z_{\xi\xi} y_\eta x_\zeta + z_\eta y_\zeta x_{\xi\xi} + z_\zeta y_{\xi\xi} x_\eta)] \\
&\quad -\mathcal{J}^2 [(x_\xi y_{\xi\eta} z_\zeta + x_{\xi\eta} y_\zeta z_\xi + x_\zeta y_\xi z_{\xi\eta}) - (z_\xi y_{\xi\eta} x_\zeta + z_{\xi\eta} y_\zeta x_\xi + z_\zeta y_\xi x_{\xi\eta})] \\
&\quad -\mathcal{J}^2 [(x_\xi y_\eta z_{\zeta\xi} + x_\eta y_{\zeta\xi} z_\xi + x_{\zeta\xi} y_\xi z_\eta) - (z_\xi y_\eta x_{\zeta\xi} + z_\eta y_{\zeta\xi} x_\xi + z_{\zeta\xi} y_\xi x_\eta)] \\
&= -\mathcal{J}^2 (y_\eta z_\zeta - y_\zeta z_\eta) x_{\xi\xi} - \mathcal{J}^2 (z_\eta x_\zeta - z_\zeta x_\eta) y_{\xi\xi} - \mathcal{J}^2 (x_\eta y_\zeta - x_\zeta y_\eta) z_{\xi\xi} \\
&\quad -\mathcal{J}^2 (y_\zeta z_\xi - y_\xi z_\zeta) x_{\xi\eta} - \mathcal{J}^2 (z_\zeta x_\xi - z_\xi x_\zeta) y_{\xi\eta} - \mathcal{J}^2 (x_\zeta y_\xi - x_\xi y_\zeta) z_{\xi\eta} \\
&\quad -\mathcal{J}^2 (y_\xi z_\eta - y_\eta z_\xi) x_{\zeta\xi} - \mathcal{J}^2 (z_\xi x_\eta - z_\eta x_\xi) y_{\zeta\xi} - \mathcal{J}^2 (x_\xi y_\eta - x_\eta y_\xi) z_{\zeta\xi} \\
&= -\mathcal{J} (\xi_x x_{\xi\xi} + \xi_y y_{\xi\xi} + \xi_z z_{\xi\xi} + \eta_x x_{\xi\eta} + \eta_y y_{\xi\eta} + \eta_z z_{\xi\eta} + \zeta_x x_{\zeta\xi} + \zeta_y y_{\zeta\xi} + \zeta_z z_{\zeta\xi})
\end{aligned}$$

The substitution for \mathcal{J}_ξ gives

$$\begin{aligned}
\frac{\partial}{\partial \xi} (\xi_x) &= \frac{\partial}{\partial \xi} [\mathcal{J} (y_\eta z_\zeta - y_\zeta z_\eta)] \\
&= \mathcal{J} (y_{\xi\eta} z_\zeta - y_{\zeta\xi} z_\eta + z_{\zeta\xi} y_\eta - z_{\xi\eta} y_\zeta) + \mathcal{J}_\xi (y_\eta z_\zeta - y_\zeta z_\eta) \\
&= -\xi_x (\xi_x x_{\xi\xi} + \xi_y y_{\xi\xi} + \xi_z z_{\xi\xi}) \\
&\quad -\eta_x (\xi_x x_{\xi\eta} + \xi_y y_{\xi\eta} + \xi_z z_{\xi\eta}) \\
&\quad -\zeta_x (\xi_x x_{\zeta\xi} + \xi_y y_{\zeta\xi} + \xi_z z_{\zeta\xi})
\end{aligned}$$

Likewise, other derivatives can be obtained. After substitution, the Laplacian $\nabla^2\xi$ becomes

$$\begin{aligned}\nabla^2\xi = & -(\xi, \xi)(\xi_x x_{\xi\xi} + \xi_y y_{\xi\xi} + \xi_z z_{\xi\xi}) - 2(\xi, \eta)(\xi_x x_{\xi\eta} + \xi_y y_{\xi\eta} + \xi_z z_{\xi\eta}) \\ & -(\eta, \eta)(\xi_x x_{\eta\eta} + \xi_y y_{\eta\eta} + \xi_z z_{\eta\eta}) - 2(\eta, \zeta)(\xi_x x_{\eta\zeta} + \xi_y y_{\eta\zeta} + \xi_z z_{\eta\zeta}) \\ & -(\zeta, \zeta)(\xi_x x_{\zeta\zeta} + \xi_y y_{\zeta\zeta} + \xi_z z_{\zeta\zeta}) - 2(\zeta, \xi)(\xi_x x_{\zeta\xi} + \xi_y y_{\zeta\xi} + \xi_z z_{\zeta\xi})\end{aligned}$$

Appendix C

Implementation of Boundary Conditions

Numerical simulations of the Euler equations require a procedure for implementing the boundary conditions in a manner consistent with the physics of the flow. Incorrect application of the boundary conditions can lead to wrong solutions, or may result in instability in the computations. This appendix explains the implementation of the boundary conditions employed in this dissertation.

C.1 Supersonic Inflow

This boundary condition, applied at supersonic inflows, simply imposes prescribed or free-stream values on the inflow boundary grid points. This procedure is applied at the inflow boundary for computation of supersonic flow past a blunt body.

C.2 Supersonic Outflow

At supersonic outflows, flow variables can be simply extrapolated from the interior points onto the boundary grid points. This type of boundary condition is implemented on the supersonic outflow boundaries for supersonic flow past a blunt body.

C.3 Subsonic Outflow

For subsonic outflow boundary, flow variables can be simply extrapolated from the neighboring interior points onto the boundary grid points. This type of boundary condition is implemented on the subsonic outflow boundaries for supersonic flow past a blunt body.

C.4 Solid Wall Boundary Condition

A more general approach in devising a procedure to enforce a solid wall boundary condition involves the following idea. First, it is assumed that at the wall the normal gradient of the pressure is equal to zero, therefore its value at the wall can simply be extrapolated from the interior. Being solid, there is no mass flow across the wall, which is expressed as $\vec{u} \cdot \hat{n} = 0$, where \hat{n} is the unit vector normal to the wall. However, the magnitude of the momentum vector $\vec{M} = \rho\vec{u}$ can be assumed to be the same, only its direction needs to be set tangential to the wall (velocity slip condition). In other words, upon encountering the solid wall the momentum vector is rotated to point tangentially along the wall. The density at the wall can then be obtained using the fact that for steady

state flow of inviscid, non-heat conducting gas, the total enthalpy h_t is constant throughout the flowfield. Mathematically, it can be expressed as:

$$h_t = \frac{1}{2\rho^2} \vec{M} \cdot \vec{M} + \frac{\gamma}{\gamma - 1} \frac{p}{\rho} = \text{constant} \quad (\text{C.1})$$

from which density at the wall can then be obtained as a solution of a quadratic equation:

$$\rho = \frac{\gamma p + \sqrt{\gamma^2 p^2 + 2h_t (\gamma - 1)^2 \vec{M} \cdot \vec{M}}}{2h_t (\gamma - 1)} \quad (\text{C.2})$$

where the positive sign has been chosen to prevent negative values for the density.

Appendix D

Computational Code (Separate Document)

VITA

Wei Dong

Year of Birth: 1972

Place of Birth: Handan, Hebei Province, P. R. China

Degree: B.E., Engineering Mechanics, July 1995
Tsinghua University; Beijing, P. R. China